High Strain Rate Properties of Soft Polymeric and Biological Materials



Aaron Graham
Wadham College
University of Oxford

A thesis submitted for the degree of
Doctor of Philosophy
Michaelmas 2023

This thesis is dedicated to
Library Genesis and Sci-Hub
for democratising access to publicly funded knowledge

Acknowledgements

First and foremost, I would like to thank my supervisor, Clive Siviour. This research project would not have been possible without your support, guidance, and patience. I could not have asked for a better supervisor, and am incredibly glad to have had you as a supervisor.

Without the generous financial support of the Rhodes Trust, this research project would not have been possible; I am grateful for their support.

To my Oxford friends, for their endless support and kindness. You made Oxford fun, and brightened the otherwise stygian darkness of the English winters. Andy and Neil, for your technical support, willingness to manufacture things sometimes at the last minute, and general good vibes. Richard, for teaching me that quality machining takes time.

To my office and lab-mates, for the jokes, support and banter. In particular to Thom and Isabella, without whom this thesis would have been less enjoyable but finished sooner.To MatchID, the superior DIC software. It is only after hitting the wall a few times (using DaVis) that one truly appreciates a door (MatchID).

To Kate, my girlfriend. My time at Oxford has been greatly improved by your presence. Thank you.

And last but not least, Lilith. You were born after this project started, and died before it ended, but helped so much along the journey. Of all the animal friends I've had, you were the favourite. You didn't have long on this earth, but did so much with the time you had.

Abstract

Accurate characterisation of the response of low modulus materials to applied deformation at high frequencies, or strain rates, is of significance in many industrial or scientific settings, in particular when considering personal protective equipment. However, because of the low speed of sound in these materials, producing accurate measurements of material constitutive properties, and separating these from specimen structural response, can be challenging.

This report presents research on the development and use of a novel methodology for the mechanical characterisation of ultra-soft biological tissues and polymers at high frequencies. The core development is a novel apparatus for high rate characterisation of soft materials under shear loading. This apparatus and methodology has been successfully used to characterise silicone based elastomers, agarose gel and brain tissue at frequencies of over 1 kHz. Firstly, the apparatus was designed, modelled and implemented, with extensive validation data obtained from a commercial silicone elastomer. The apparatus was then used in conjunction with traditional rheometry to characterise a PolyDiMethylSiloxane (PDMS) polymer, and to show that the mechanical properties can be tuned over a wide range of both stiffnesses and frequencies, by varying the ratio of crosslinker when curing the PDMS, from hundreds of Pa up to several MPa.

Further experiments were then performed on an agarose gel and brain tissue. Again, it was shown that the properties of the agarose could be modified by changing the composition. Further, the ability of the measurement system to examine spatially varying properties was confirmed. This is relevant to biological tissues, and also allows for more efficient data gathering, as multiple material types can be characterised in a single experiment. Both PDMS and agarose hydrogels are commonly used as simulants for biological tissues, however there is a paucity of data in the literature about the high frequency behaviour of these materials. This gap in the literature is being closed by this research.

The ultimate aim of this research was to characterise brain tissue. Porcine brain tissue obtained from a local butcher has been characterised over a wide range of frequencies at two temperatures.

A key enabling technology for the experiments was the Virtual Fields Method (VFM), which is used as a means to extract quantitative information about stresses inside a specimen from full-field acceleration data. A side project was performed to develop a method of characterising the large strain behaviour of a material over a

wide range of stress states and strain rates using a single test. This is achieved via the use of the VFM, applied to a T shaped specimen designed to develop heterogeneous stress states during the test. This method has been validated over a range of strain rates and temperatures on two materials, 1000 series Aluminium and Polycarbonate with PDMS crosslinker. The Aluminium material was selected as it exhibits almost perfect elasto-plastic behaviour, with a large strain to failure. In contrast, the polymeric material demonstrates complex post-yield behaviour. Here, the VFM was shown to be a superior analysis method, even when conducted on data obtained from traditional uniaxial tensile tests. Unlike traditional analysis methods, the VFM was capable of measuring local material behaviour, and separating geometric effects and material behaviour on the global behaviour of the sample. This allowed for more accurate characterisation of the material, using fewer tests. This advantage was further increased when using the T specimens.

Key contributions of this thesis are therefore the development of two novel test methodologies with wide applicability to measure the mechanical response of low and high modulus materials. The high rate shear testing apparatus and methodology characterises the full-field mechanical properties of soft materials over a wide range of frequencies, while the T test methodology is capable of characterising stiff engineering polymers and metals accurately and repeatably using far fewer tests than would be required under traditional engineering test methodologies. These provide data that would not be possible to obtain using traditional engineering test methodologys. A second contribution is the generation of novel high rate data on low modulus polymers and brain tissue. In preparation for future projects on this topic, a second high strain rate characterisation methodology, for volumetric (compressive) testing was developed in Finite Element code. It is shown that this is, in principle, a viable method for soft material characterisation; however, it could not be implemented in this thesis as it requires high speed imaging that is just out of reach of current technologies.

Contents

List of Figures viii

List of Tables xi

1 Introduction 1
- 1.1 Context . . . 1
- 1.2 Motivation and Objectives . . . 2
- 1.3 Report overview . . . 2

2 Literature review 4
- 2.1 Mech properties and models of ultra-soft materials . . . 4
  - 2.1.1 Deviatoric response . . . 5
  - 2.1.2 Dilatational response . . . 13
  - 2.1.3 Electromechanical coupling . . . 15
  - 2.1.4 Post-mortem brain properties . . . 16
- 2.2 Phantom materials and ultra-soft Gels . . . 16
  - 2.2.1 Phantom materials . . . 16
  - 2.2.2 PDMS . . . 17
- 2.3 Test methodology . . . 19
  - 2.3.1 *In vivo* mechanical testing . . . 19
  - 2.3.2 *Ex vivo* testing . . . 20
  - 2.3.3 Indentation testing of brain tissue . . . 21
- 2.4 DIC and the VFM . . . 23
  - 2.4.1 DIC . . . 23
  - 2.4.2 The VFM . . . 26
- 2.5 Summary and motivation . . . 31

3 Methodologies 32
- 3.1 Metrology and Loading . . . 32
  - 3.1.1 Measurement and analysis . . . 32
  - 3.1.2 Loading . . . 33
- 3.2 Phantom selection and characterisation . . . 34
  - 3.2.1 Selection of Phantom material . . . 34
  - 3.2.2 Mechanical characterisation of selected phantom . . . 35

4 Validation of apparatus and methodology 41

5 Mechanical Properties of Sylgard184 over a wide range of frequencies, temperatures, and crosslinker ratios 66

6 Tests on Brain tissue and Agarose 84

7 T test 100

8 Conclusions 131
8.1 Summaries . . . 131
8.1.1 Development of apparatus and methodology . . . 131
8.1.2 Sylgard . . . 132
8.1.3 Bio-materials . . . 133
8.1.4 VFM on Engineering materials . . . 133
8.2 Future work . . . 134

References 136

Appendices

A Design and simulation of proposal for future test methodology 148
A.1 Design of apparatus . . . 148
A.1.1 Specimen containment . . . 149
A.1.2 Dilatational characterisation . . . 152
A.2 Simulation of experimental setup . . . 153
A.2.1 Effect of sleeve material on stress wave . . . 154
A.2.2 Effect of friction on stress wave . . . 155
A.2.3 Parameter extraction from simulated experiment . . . 156
A.2.4 Conclusion . . . 159

List of Figures

2.1 Mechanical properties of various human tissues - note the extremely low modulus of brain tissue. Image taken from Budday et al. (July 2019)[4] 5
2.2 Single Maxwell element 7
2.3 Generalised Maxwell-Weichart model 7
2.4 Fitting various hyper-elastic material models to experimental data on brain tissue. Note that the 1-term Ogden model out-performs the other hyper-elastic models significantly, in spite of only using 2 parameters. Note too that the 'compression' and 'tension' loading are unconfined, and as a result consists almost entirely of a deviatoric rather than a dilatational deformation. Figure adapted from Budday et al. (Jan. 2017) [14]. 10
2.5 Multiplicative decomposition model. Individual constitutive models are required for the elastic stress σ_e, the viscous stress σ_v, and the viscous stretch rate d_v. Note the similarity in structure to the SLS model shown in fig. 2.3. Image adapted from Rooij and Kuhl (Jan. 2016) [23] 11
2.6 Partially confined and unconfined testing of brain tissue. Note that while humidity is controlled in fig. 2.6b, de-watering is not prevented. Dewatering is only partially prevented in fig. 2.6a 14
2.7 Shear modulus vs. probe voltage via indentation, and burn marks left by high voltage probe [48] 15
2.8 Reported Young's Modulus vs crosslinking ratio for Sylgard 184, taken from Glover *et al.* Note that for an incompressible material, Young's modulus (reported here) will be approximately 3 times the shear modulus (reported in the rest of this paper) 18
2.9 Overview of MRI elastography method adapted from [43]. A: generating shear waves in the brain via external actuation. B: phase-contrast MRI of the resultant deformation field. C: Extracting the mechanical property distribution from the imaged wave field. 20
2.10 Unconfined *ex vivo* testing of brain tissue in shear by Rashid, Destrade, and Gilchrist (Dec. 2013) [57] 21
2.11 Grey scale profile of the reference image $f(\boldsymbol{X})$ and the deformed image $g(\boldsymbol{y}(\boldsymbol{X}))$. Image adapted from [100] 24

2.12 Local vs Global DIC deformation fields. Image taken from [100] . . 25

3.1 Shore hardness of various common polymers - note that Ecoflex 00-10 is at the bottom of the range of the scale, and Ecoflex GEL is softer than the measurement scale. Image taken from [119] 35

3.2 Example of a test where slipping occurred at high frequencies - note the sudden drop in storage modulus in particular. When testing at higher strain amplitudes, slipping occurred earlier as a result of increased forces. 37

3.3 Shear storage and loss moduli for Ecoflex GEL over a range of temperatures and frequencies 38

3.4 Shift factors vs temperature for Ecoflex GEL, taking 25° C to be reference temperature 39

A.1 Quarter cross-section view of proposed loading setup. Loading is applied to the brain sample via the input bar. The brain sample is immersed in cerebrospinal fluid (CSF) simulant, better emulating *in vivo* drainage and loading conditions. The sleeve is transparent, allowing one to image the brain sample directly and make use of DIC for full-field displacement measurements. The free surface guarantees a stress-free boundary, allowing for easy calculation of stresses via integration of the acceleration field. 149

A.2 Axial stress distribution along the surface of the sample at 5μs. Loading is a step load of 1 MPa pressure. Three containment material types are modelled: perfectly rigid (blue), quartz (red), and PMMA (brown). 155

A.3 Distribution of S22 at 5μs for various containers, using a clean loading pulse of 1 MPa. Figure a models only a brain specimen and a water specimen, whilst figures b and c show brain, water, and the sleeve material. Note that the magnitudes of the stress waves are not of great importance, but rather the distribution within the brain tissue. A nominally perfect rigid sleeve results in a perfectly 1d stress profile, a quartz sleeve is worse, but most of the inhomogeneity in the stress wave occurs in the water portion, rather than the sample. For a PMMA sleeve, even the sample portion undergoes messy loading . . 156

A.4 Stress at the surface of the specimen compared to stress calculated by integrating the acceleration field and stress taking friction effects into account. Note that the shear stresses due to Newtonian viscosity in the fluid medium are negligible - lines 2 and 3 overlap almost exactly. Loading is 1 MPa applied through a PMMA input bar - the impedance mismatch at the PMMA-sample interface causes ineffective force transmission, hence the particularly non-constant stress profile 157
A.5 Stress at the surface of the specimen according to FEA output, integrating the acceleration field of the DIC output, and multiplying the DIC strain field by the bulk modulus of the specimen. 158
A.6 Bulk modulus obtained by comparing the stress in fig. A.5 to the measured strain. Where the measured strain was less than 10% of the maximum strain, this region was ignored in order to avoid dividing by very small strain values. 158

List of Tables

2.1 Local vs Global DIC problem suitability 26
2.2 Definition of the 3 types of problem as defined by Pierron and Grédiac (2012) [109] 28

3.1 Test parameters for shear DMA on silicone gel 36

A.1 Approximate stiffness and refractive index of various transparent materials 151
A.2 Material parameters for simulating brain under compression 154

List of Symbols and Abbreviations

Symbol	Description	Unit
$\boldsymbol{X}$	Undeformed position (material/Lagrangian co-ordinate)	m
$\boldsymbol{x}$	Current position (spatial/Eulerian co-ordinate), and a function of $\boldsymbol{X}$ and t	m
$\boldsymbol{u}$	Displacement field ($\boldsymbol{x} - \boldsymbol{X}$)	m
$\boldsymbol{F}$	Deformation gradient, $\frac{\partial \boldsymbol{x}}{\partial \boldsymbol{X}}$	unitless
$\boldsymbol{l}$	Velocity gradient, $\dot{\boldsymbol{F}} \cdot \boldsymbol{F}^{-1}$	s^{-1}
$\boldsymbol{C}$	Right Cauchy-Green deformation tensor ($\boldsymbol{F^T} \cdot \boldsymbol{F}$)	unitless
$\boldsymbol{B}$	Left Cauchy-Green deformation tensor ($\boldsymbol{F} \cdot \boldsymbol{F^T}$)	unitless
$\boldsymbol{b}$	Body force tensor. Describes body forces (such as gravity) on an object	N/kg
W	Strain energy density function, describes the strain energy of the material in terms of the deformation gradient.	J
λ_i	i^{th} principal stretch (1+strain)	unitless
J	Volumetric strain ratio, det($\boldsymbol{F}$)	unitless
$\boldsymbol{\sigma}$	Cauchy stress. Stress in the spatial description, also known as "true stress".	Pa
$\boldsymbol{P}$	First Piola-Kirchhoff stress.	Pa
$\boldsymbol{S}$	Second Piola-Kirchhoff stress	Pa
$\boldsymbol{T}$	Surface traction	Pa
S_f	Loaded surface	m^2
$\boldsymbol{n}$	Outward facing unit normal	unitless
$\boldsymbol{u}^*$	Virtual displacement	m
$\boldsymbol{\epsilon}^*$	Virtual strain	unitless
V	Volume	m^3
$\dot{\phi}$	Rate of change of ϕ with time, $\frac{\partial \phi}{\partial t}$. ϕ being a generic quantity (mass, velocity, energy etc)	ϕ/s
$\ddot{\phi}$	Rate of change of $\dot{\phi}$ with time, $\frac{\partial^2 \phi}{\partial t^2}$	ϕ/s^2
E_Y	Young's modulus/Elastic modulus	Pa
μ	Shear modulus	Pa
ν	Poisson's ratio	unitless

Symbols that are in bold represent tensor quantities, and symbols that are not in bold represent scalar quantities.

1 Introduction

1.1 Context

The human brain is one of the least understood tissues in the human body. Comprising only 2% of bodyweight, the brain is responsible for approximately 20% of energy consumption [1]. Ensconced in the skull, surrounded by cerebrospinal fluid, and protected by the blood-brain barrier, the brain is well isolated from the external mechanical and chemical environment[2].It is the softest biological tissue by orders of magnitude [2–4], with a shear modulus of approximately 1 kPa. Unlike most other organs, the function of the brain appears to be almost entirely electro-chemical and not mechanical. As a consequence, initial research on brain tissue focussed primarily on electrical rather than mechanical properties [5]; however, recent studies have showed that the mechanical behaviour of the brain is closely linked to its cognitive functions[3]. The brain's mechanical response plays a prevalent role, across a wide range of timescales and magnitudes, in many pathological conditions and novel potential clinical treatments ranging from low rate behaviour observed in hydrocephaly [6] (abnormal accumulation of fluid and (quasi-static) pressure in the brain) or acidosis [7], up to the dynamic events observed in Traumatic Brain Injury (TBI) [8, 9] or ultrasound neuromodulation [10].

In spite of being well isolated from the external environment, the brain is linked

to major public health effects as a result of both injury[1] and disease. A recent (2016-2018) event affecting on US government personnel in Havana [13] showed just how poorly the brain is understood, and how important that understanding is.

1.2 Motivation and Objectives

In spite of the importance of accurately characterising brain tissue's mechanical response, test data in the literature have given a wide spread of sometimes contradictory results. Part of the reason for this is the use of standard engineering test methodologies on brain tissue, despite their unsuitability. Accurately characterising brain tissue is challenging as a result of its extreme softness, sensitivity to drainage conditions, natural biological variability, and complex post-mortem changes.

This dissertation builds towards improved measurements of the mechanical response of brain tissue through the development of novel test methodologies for low modulus polymers. In particular, the research presented focusses on the design and application of a novel apparatus for measuring the deviatoric (shear) modulus at high frequencies. The new system, which builds on recent developments in quantitative image analsysis, is described, and initially tested on silicone elastomers with different mechanical properties, before being applied to brain tissue. The thesis also describes a parallel project in which characterisation of 'engineering' polymers is performed using a similar methodology. Finally, a test method for dilatational (compression/tension) characterisation in *in vivo* drainage conditions is described and assessed through FE simulation.

1.3 Report overview

Chapter 2 reviews relevant literature, focusing on the mechanical properties of brain tissue and currently used test methodologies. The shortfalls of these test methodologies are discussed, and a significant gap in the literature described.

[1] TBI affects over 2 million people per year[11, 12]

Chapter 3 gives a brief overview of the silicone material chosen as an initial phantom material[2] for test development and validation, as well as some of the experimental methodologies used throughout this thesis.

The test methodology developed for measuring the shear properties of low modulus polymers at high frequencies is described in detail in Chapter 4, which consists of a paper *Characterising the frequency-response of ultra-soft polymers with Virtual Fields Method*, published in 2021 in Strain. Here the technique is applied to a commercial silicone elsastomer. In order to further assess the technique, and also provide useful data on silicones, which are often used as phantoms for biological tissue, further work on these materials is presented in Chapter 5, which is a paper intended for submission to Polymer or Polymer Testing. Chapter 6 then moves on to experiments on agarose gel and brain, with the intention of showing the capability of this method to measure properties of brain at both room temperature and 37 °C. It is intended to submit this paper to Journal of the Mechanical Behavior of Biomedical Materials.

Chapter 7 presents a somewhat different piece of research in which the analysis technique used in this thesis, the virtual fields method, is applied to a novel test geometry on engineering polymers. This paper will be submitted to International Journal of Mechanics and Physics of Solids. This research arose from a research collaboration with other members of the research team in Oxford. Finally, Conclusions and recommendations for further work are presented in Chapter 8, with Appendix A progressing the research on brain by proposing a novel test design for measuring the dilatational response under undrained conditions.

[2]A phantom material being a useful substitute for a biological tissue, with similar mechanical properties, for use when commissioning or validating equipment. In this case, a PDMS polymer with similar mechanical properties to brain tissue is a useful phantom, as it is has more consistent mechanical properties than brain tissue, and is easier to acquire, store, use, and dispose of

2
Literature review

This literature review primarily focuses on the mechanical properties of and test methods associated with brain tissue, with other materials such as tissue phantoms covered in less detail. This is followed by an over-view of Digital Image Correlation (DIC) and the Virtual Fields Method (VFM), the key techniques used to analyse experimental data in the remainder of this thesis.

2.1 Mechanical properties and models of brain tissue and ultra-soft gel materials

Brain tissue is a highly complex material: bi-phasic, non-linear, viscous, porous, saturated, and heterogeneous [4]. When loaded in shear, brain tissue is the softest human tissue (with a shear modulus on the order of 1 kPa [14]), but is almost incompressible, with a bulk modulus on the order of 2 GPa[1] [8].) This extreme softness makes accurate mechanical characterisation difficult: engineering material methodologies and equipment tend to be designed for stiffer materials. Additionally, the large mismatch in magnitude between the shear modulus ($\approx 10^3$ Pa) and the bulk modulus ($\approx 10^9$ Pa) makes brain tissue extremely sensitive to mechanical boundary conditions during testing.

[1] Note the similarity to water, which also has a bulk modulus of approximately 2 GPa

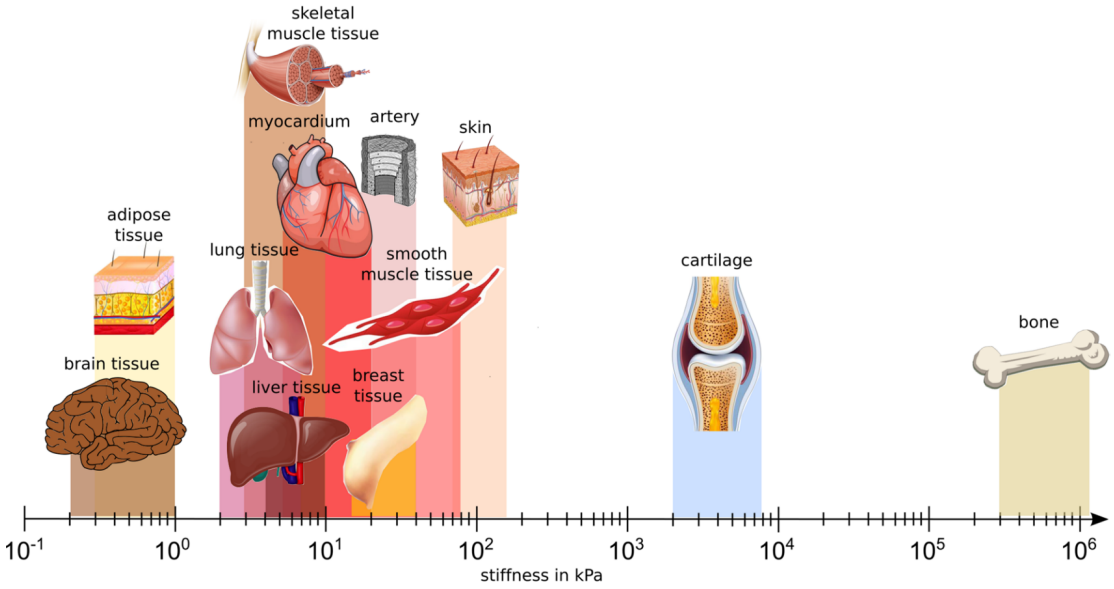


Figure 2.1: Mechanical properties of various human tissues - note the extremely low modulus of brain tissue. Image taken from Budday et al. (July 2019)[4]

2.1.1 Deviatoric response

The shear response of brain tissue is non-linear, and shows significant time-dependence. Most testing to date has focused on unconfined[2] testing of brain tissue in various ways, all of which *de facto* measure the dilatational response, given the effectively incompressible nature of the material. Mihai et al. (Sept. 2015) [15] summarised the unusual shear behaviour of brain tissue as:

1. the shear modulus increases sharply as compression in the direction orthogonal to the shear direction increases;

2. the shear modulus remains almost constant or may decrease as tension in the direction orthogonal to the shear direction increases;

3. the elastic modulus increases or remains almost constant when compression increases.

[2]tests where the sample is free to expand, as in the vast majority of mechanical test setups

Additionally, Li et al. (2018) [16] showed that brain tissue exhibits a compression-tension asymmetry under dilatational loading, with a lower effective tensile modulus (discussed further in section 2.1.2.3).

2.1.1.1 Linear time dependent behaviour

Whilst the brain has been characterised at the most general level as a poro-visco-hyperelastic material[4, 6, 15, 17–33], for small deformation (such as observed in vibrations), linear visco-elastic models have been used as a first approximation [13, 23, 34–52] Whilst brain tissue exhibits significant non-linearity[5, 20, 22, 30], linear-visco-elastic models are significantly simpler to describe, characterise, and implement. When only the low strain regime is to be modelled, linear visco-elastic models can be sufficient. A particular advantage of a linear visco-elastic model is that it allows for the use common engineering techniques such as Dynamic Mechanical Analysis (DMA)[3] as well as Magnetic Resonance Elastography (MRE), a non-invasive *in vivo* measurement of the brain's shear modulus - see section 2.3.1 for further details.

Complex modulus: In linear viscoelasticity, the complex modulus allows for the description of a material's viscoelasticity in terms of a storage and a loss modulus, where the storage modulus G' represents the elastic response[4], and the loss modulus G'' represents the viscous response[5]. The complex shear modulus is then given by:

$$G^* = G' + iG'' \tag{2.1}$$

The ratio between the storage and the loss modulus is equivalent to the tangent of the phase lag between the stress and the strain under oscillatory loading, and is effectively a measure of the damping ability of the material. In practice, the storage and loss moduli are often highly dependent on frequency; they are often described using convolution models such as the Prony series.

[3] a technique used for probing the frequency response of a material

[4] i.e. the portion of the response equivalent to that of a purely elastic sprint

[5] i.e. the portion of the response equivalent to that of a purely viscous damper, with all energy dissipated

Convolution models: One of the simplest viscoelastic models is a Maxwell element which consists of a spring-dashpot in series as shown in fig. 2.2, resulting in a stress-strain response governed by:

$$\frac{\dot{\sigma}}{G} + \frac{\sigma}{\eta} = \dot{\epsilon} \tag{2.2}$$



Figure 2.2: Single Maxwell element

If a sinusoidal deformation of frequency ω is applied and the relaxation time $\tau = \frac{\eta}{G}$ is defined, the complex modulus can be written as:

$$G^*(\omega) = \underbrace{G\frac{\tau^2\omega^2}{\tau^2\omega^2+1}}_{\text{Storage modulus}} + \underbrace{iG\frac{\tau\omega}{\tau^2\omega^2+1}}_{\text{Loss Modulus}} \tag{2.3}$$

In reality most materials have a spectrum of relaxation times, which can be modelled via the Generalised Maxwell-Weichart model, consisting of a series of Maxwell elements in parallel [53]. Figure 2.3 shows the generalised Maxwell-Weichart model, henceforth referred to as the GMW model.

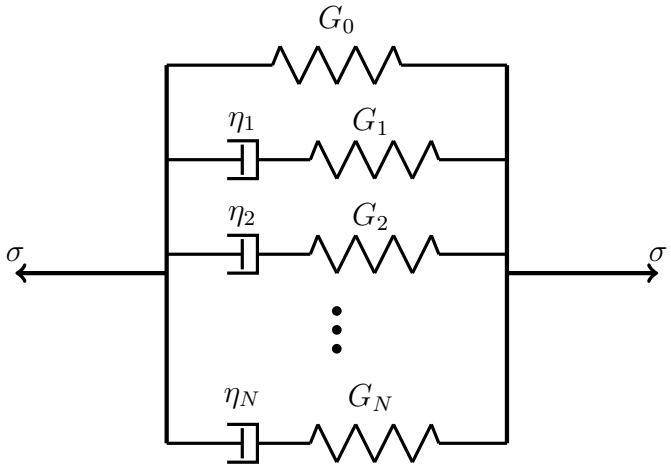


Figure 2.3: Generalised Maxwell-Weichart model

The storage and loss moduli for the GMW model are the sum of the storage and loss moduli for each branch, resulting in the following expression for the

complex modulus:

$$G^*(\omega) = \underbrace{G_0 + \sum_{n=1}^{N} G_n \frac{\tau_n^2\omega^2}{\tau_n^2\omega^2+1}}_{\text{Storage modulus}} + \underbrace{i\sum_{n=1}^{N} G_n \frac{\tau_n\omega}{\tau_n^2\omega^2+1}}_{\text{Loss Modulus}} \tag{2.4}$$

In the presence of multiple relaxation times, it is difficult to measure the response of each branch in isolation, and as a result it is generally more feasible to measure the frequency dependent complex modulus over a range of frequencies or relaxation times and then solve for the existence of each branch as an inverse problem [3, 4, 35, 54]. Data obtained during shear testing of brain tissue have predicted a wide range of time constants [3, 23, 31, 32, 55–58], implying that the tissue exhibits complex time dependent behaviour, and cannot be characterised by a single relaxation time. Viscoelastic behaviour is exhibited over a wide range of time-scales, from milliseconds to minutes [54].

2.1.1.2 Non-linear time independent response

Many non-linear hyper-elastic material models have been used to model the shear behaviour of brain, including the Ogden, neo-Hookean, Mooney-Rivlin, Gent, and Demiray models[6, 14, 27]. These models were all[6] originally used to model hyper-elastic polymers. Models originally used for modelling fibrous tissues (such as arterial walls or skin) include the Gasser-Ogden-Holzapfel and Fung models, however these have been shown to model the behaviour of brain tissue less accurately than other hyperelastic models of similar complexity[15, 30]. Some of the more commonly used hyper-elastic models are discussed below - for a more exhaustive list of hyperelastic models of brain tissue the reader is referred to the work of Rooij and Kuhl [23]

Hyperelastic models express the material behaviour in terms of a scalar strain energy density function W. This strain energy density function describes the stored strain energy in the material as a function of the deformation gradient. This in turn allows one to express the stress tensor as a function of the deformation gradient tensor, allowing one to capture a wide variety of complex material behaviours.

[6]Barring the Demiray model, however very similar models had previously been proposed for rubbers

The Ogden model (first proposed by Ogden in 1972 for modelling rubbers [59]) models the strain energy density of the material as a function of the principal stretch (λ), shear moduli (μ), and strain hardening coefficients (α):

$$W_{Og} = \sum_{p=1}^{N} \frac{\mu_p}{\alpha_p} \left(\lambda_1^{\alpha_p} + \lambda_2^{\alpha_p} + \lambda_3^{\alpha_p} - 3 \right) \tag{2.5}$$

The neo-Hookean and Mooney-Rivlin models are subsets of the Ogden material model, with $(N = 1, \alpha = 2)$ and $(N = 2, \alpha_1 = 2, \alpha_2 = -2)$, respectively.

The Gent hyperelastic model [60] defines the strain energy density in terms of a shear modulus μ, the first invariant of the left Cauchy-Green deformation tensor I_1, and a limiting extension value I_m:

$$W_{Gn} = -\frac{\mu J_m}{2} \ln \left(1 - \frac{I_1 - 3}{J_m} \right) \tag{2.6}$$

where $J_m = I_m - 3$.

The Demiray hyperelastic model [61] is an exponential strain stiffening hyperelastic model in terms of the first invariant of the left Cauchy-green deformation tensor I_1, taking the form:

$$W_{Dm} = \frac{1}{\beta} \left[e^{\beta(I_1 - 3)} - 1 \right] \tag{2.7}$$

The Fung hyperelastic model combines a Neo-hookean and an exponential stiffening component, effectively combining the Demiray and neo-Hookean models:

$$W_{Fn} = \frac{C}{2\alpha} \left(\alpha(I_1 - 3) + e^{\alpha(I_1 - 3)} \right) \tag{2.8}$$

The Fung and Demiray models (and more complex models such as the Gasser-Ogden-Holzapfel model [62]) are well suited to modelling non-linear fibrous materials such as skin, but perform poorly when modelling very soft tissues such as brain or fat [15] as the non-linearity of these materials results from their porous cellular structure rather than from a fibre network [15, 49, 63].

Summary Whilst each of the above material models captured the behaviour of brain more effectively than a simple linear elastic model, it has been shown that only the Ogden model is able to capture the significant compression-tension asymmetry exhibited by brain tissue at high strains [14] - an example is shown in fig. 2.4. Mihai et al. [30] fitted a 3-term Ogden model (a combination of a 1-term Ogden and a Mooney-Rivlin model) to brain tissue, but this model did not significantly improve on the results of a single term Ogden model. The Ogden model has been criticized for being purely phenomenological in nature, however it is capable of capturing the nonlinear deviatoric behaviour of brain tissue with a small number of parameters and a high degree of accuracy [23]. The Ogden model does not accurately capture the dilatational response of brain tissue, however this is often not an issue given the relatively incompressible nature of brain tissue (and high shear:bulk modulus ratio of approximately 6 orders of magnitude [14].

It should be noted that simply increasing the order of the Ogden model results in a better fit, but risks leading to a series of non-unique material parameters which are strongly dependent on the initial estimate of the fitting process [64]. This issue is particularly prevalent when noisy experimental data are used.

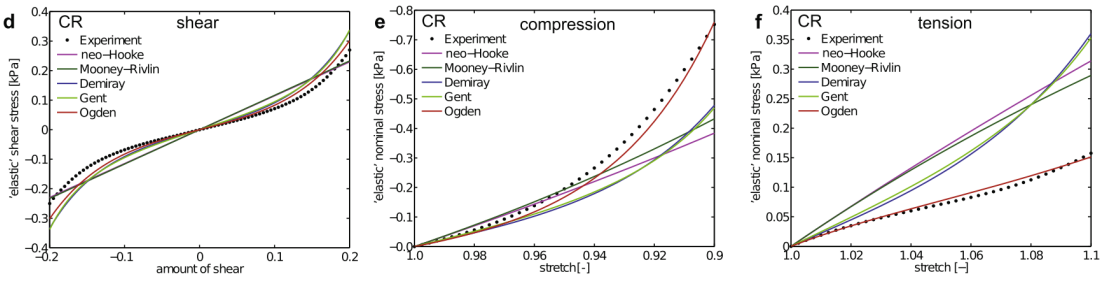


Figure 2.4: Fitting various hyper-elastic material models to experimental data on brain tissue. Note that the 1-term Ogden model out-performs the other hyper-elastic models significantly, in spite of only using 2 parameters. Note too that the 'compression' and 'tension' loading are unconfined, and as a result consists almost entirely of a deviatoric rather than a dilatational deformation. Figure adapted from Budday et al. (Jan. 2017) [14].

2.1.1.3 Nonlinear time dependent elasticity

Multiplicative decomposition of the deformation gradient into a time independent elastic component and a time dependent viscous part allows one to build up a non-linear time dependent material model capable of accounting for high strain rates and strains [23, 57] such as occurring during impact events.

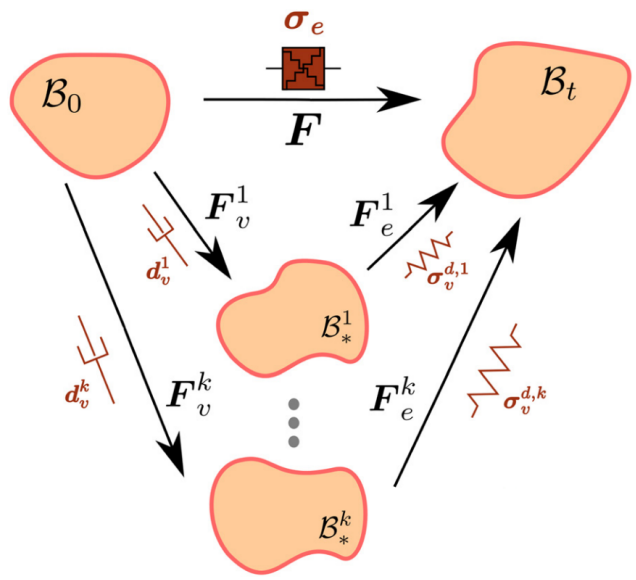


Figure 2.5: Multiplicative decomposition model. Individual constitutive models are required for the elastic stress σ_e, the viscous stress σ_v, and the viscous stretch rate d_v. Note the similarity in structure to the SLS model shown in fig. 2.3. Image adapted from Rooij and Kuhl (Jan. 2016) [23]

The fundamental approach is to multiplicatively decompose the deformation gradient $\boldsymbol{F}$ into an elastic and a viscous component:

$$\boldsymbol{F} = \boldsymbol{F}_e \cdot \boldsymbol{F}_v \tag{2.9}$$

The elastic part of the deformation decays with time, tending towards $\boldsymbol{I}$ as time approaches infinity. The strain energy density function can now be decomposed into an elastic and a viscous part, as shown in [65]:

$$W = W_\infty(\boldsymbol{C}) + W_v(\boldsymbol{C}_e) \tag{2.10}$$

Similarly to time independent hyper-elastic models, the Cauchy stress is defined in terms of the strain energy density function and the Right Cauchy-Green deformation tensor $\boldsymbol{C}$:

$$\boldsymbol{\sigma} = -p\boldsymbol{I} + \frac{2}{J}\left[\underbrace{\boldsymbol{F}\cdot\frac{\partial W_\infty}{\partial \boldsymbol{C}}\cdot\boldsymbol{F}^{\mathrm{T}}}_{\text{Elastic contribution}} + \underbrace{\boldsymbol{F}_v\cdot\frac{\partial W_v}{\partial \boldsymbol{C}_e}\cdot\boldsymbol{F}_v^{\mathrm{T}}}_{\text{Viscous contribution}}\right] \tag{2.11}$$

The velocity gradient is defined as:

$$\boldsymbol{l} = \dot{\boldsymbol{F}}\cdot\boldsymbol{F}^{-1} = \underbrace{\dot{\boldsymbol{F}}_e\cdot\boldsymbol{F}_e^{-1}}_{\boldsymbol{l}_e} + \underbrace{\boldsymbol{F}_e\cdot\dot{\boldsymbol{F}}_v\cdot\boldsymbol{F}_v^{-1}\cdot\boldsymbol{F}_e^{-1}}_{\boldsymbol{l}_v} \tag{2.12}$$

The symmetric viscous stretch rate can now be defined as:

$$\boldsymbol{d}_v = \frac{1}{2}\left[\boldsymbol{l}_v + \boldsymbol{l}_v^{\mathrm{T}}\right] = \boldsymbol{l}_v \tag{2.13}$$

The spin rate is assumed to vanish [18, 28]:

$$\boldsymbol{w}_v = \frac{1}{2}\left[\boldsymbol{l}_v - \boldsymbol{l}_v^{\mathrm{T}}\right] = \boldsymbol{0} \tag{2.14}$$

We now have expressions for the elastic deformation gradient $\boldsymbol{F}_e$, the viscous deformation gradient $\boldsymbol{F}_v$, and the viscous portion of the velocity gradient $\boldsymbol{d}_v$. This allows one to build up an appropriate non-linear time dependant material model. Three popular models in the literature are the Hrapko [28], Bilston [18], and Prevost [66] models. For the sake of brevity the Hrapko model alone will be covered, however the reader is directed to the work of Rooij and Kuhl (Jan. 2016) [23] for a review of these three models.

The Hrapko model is fundamentally similar to the SLS model, however it makes use of multiplicative decomposition for each branch rather than convolution. The strain energy density function is defined as [28]:

$$W^{\mathrm{hr}} = W_\infty(\boldsymbol{C}) + \sum_{k=1}^{n} W_v^k\left(\boldsymbol{C}_e^k\right) \tag{2.15}$$

Note that $1 + 2n$ constitutive equations are required: 1 for the elastic branch, and 2 for each viscoelastic branch. The viscous stretch rates $\boldsymbol{d}_v^k$ in each branch

depend on the deviatoric part of the viscous stresses $\boldsymbol{\sigma}_v^{d,k}$ analogously to a non-linear damper element:

$$\boldsymbol{d}_v^k = \frac{1}{2\eta^k}\boldsymbol{\sigma}_v^{d,k} \tag{2.16}$$

where η^k denotes the viscosity of the brain tissue in that viscous branch. The viscosity is expressed as a function of the stress measure $\tau = \sqrt{(1/2)\boldsymbol{\sigma}^d : \boldsymbol{\sigma}^d}$ using the Ellis model [65]:

$$\eta^k(\tau) = \eta_\infty^k + \frac{\eta_0^k - \eta_\infty^k}{1 + [\tau/\tau_0]^{n-1}} \tag{2.17}$$

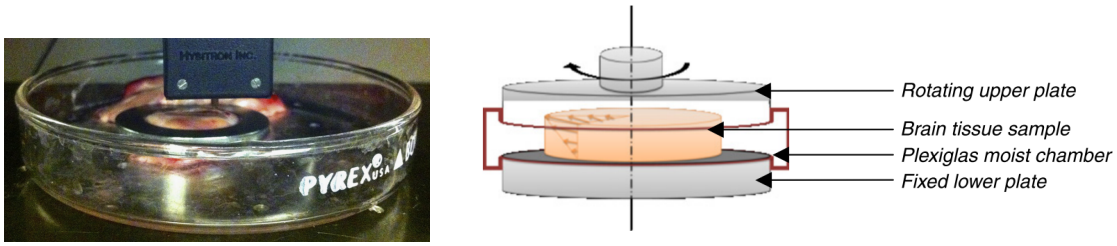
Note that if all constitutive equations of the Hrapko model are linear, the Hrapko model collapses down to the SLS model described in fig. 2.3 and eq. (2.4).

2.1.2 Dilatational response

Brain tissue is biphasic[4], consisting of approximately 80 % water [6]. As a result, it behaves as a saturated poroelastic material, with a very high bulk modulus due to the presence of the fluid [20]. This makes its behaviour highly dependent on the test setup - if the fluid is confined then one effectively measures the bulk modulus of the water, but if the water is allowed to escape then one can measure the bulk modulus of the matrix [6].

2.1.2.1 Effect of de-watering on repeated tests

Particularly when testing brain tissue *ex vivo* under unconfined compression, this de-watering effect can have a strong influence on the measured stiffness of the brain [4, 67]. Budday et al. (July 2019) [3] found that indentation testing on confined slices of brain tissue resulted in a significantly lower incidence of preconditioning when compared to unconfined testing. This is thought to be as a result of reduced de-watering of the brain sample [3]. The partially confined setup is shown in fig. 2.6a. Whilst fig. 2.6b shows brain being tested in unconfined shear, a significant number of tests in the literature use a fundamentally similar setup for direct shear, compression, and tension testing of brain tissue [20, 46, 57, 58, 67, 68].



(a) Partially confined indentation testing of brain tissue slices conducted by Budday et al. (June 2015) [3]

(b) Unconfined, humidity controlled shear rheometer test on brain tissue by Chatelin et al. (Feb. 2012) [5].

Figure 2.6: Partially confined and unconfined testing of brain tissue. Note that while humidity is controlled in fig. 2.6b, de-watering is not prevented. Dewatering is only partially prevented in fig. 2.6a

This poroelastic effect is an important part of how brain tissue behaves, and failure to take it into account is to be likely a significant contributing factor to the large disparity in mechanical properties reported in the literature.

2.1.2.2 Poroelasticity

Franceschini et al. (Dec. 2006) [6] showed that brain tissue follows consolidation theory, deforming similarly to filled elastomers under large strain, low rate loading with free drainage conditions. This effect is of particular importance for modelling developmental disorders such as hydrocephalus [4, 6, 33], but is less relevant to modelling high rate impact events as the timescale of impact events is significantly shorter than the timescale of poroelasticity. Note also that the brain does not directly experience free-drainage conditions under *in vivo* conditions.

2.1.2.3 Tension-compression asymmetry

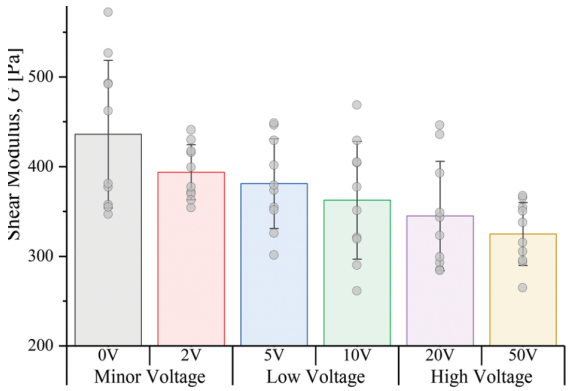
Brain tissue exhibits a significant tension-compression asymmetry, with a high compressive bulk modulus of approximately 2 GPa, but an apparent tensile modulus[7] of only 20-34 MPa after the tensile stress has exceeded approximately 4-4.6 MPa [16, 69]. This is congruent with the idea of the brain as a bi-phasic material – the fluid content strongly resists compression, but has limited capacity to resist tension [69, 70].

[7] Apparent modulus being $\frac{\partial \sigma}{\partial \epsilon}$ rather than $\frac{\sigma}{\epsilon}$

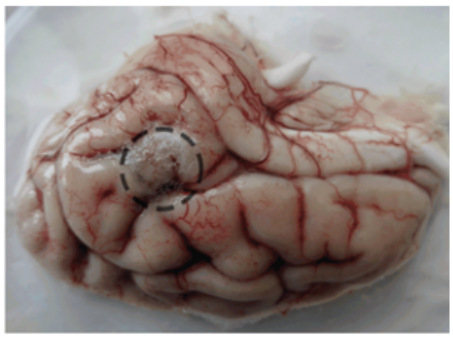
2.1.3 Electromechanical coupling

Electromechanical coupling in the brain is not a focus of this thesis, but is worth mentioning as ultimately, cognitive functions are affected by such coupling. At both cell [71, 72] and tissue [48] levels, the electrical and the mechanical response is coupled, requiring one to consider the electrical state when modelling the mechanical response. At the cell level this effect allows for ultrasound neuromodulation [72] via the application of non-invasive ultrasound to portions of the brain, able to alter the electrical activity of the cell through mechanical vibrations.

Qian et al. (Jan. 2019) [48] tested the shear modulus and relaxation time of porcine brain via indentation, and found that both the shear modulus and the relaxation time of brain decreased with increasing probe voltage. Interestingly, both the long term modulus G_∞ and the instantaneous moduli $G_{1,2}$ were affected by the voltage of the probe. Figure 2.7a shows the effect of the probe voltage on the measured instantaneous shear modulus, however it should be noted that the higher voltages in particular are significantly higher than those found *in vivo* – note too the burn marks in fig. 2.7b.



(a) Instantaneous modulus vs probe voltage [48]



(b) Burn marks left on brain from 20V probe used by Qian et al. (Jan. 2019) [48]

Figure 2.7: Shear modulus vs. probe voltage via indentation, and burn marks left by high voltage probe [48]

2.1.4 Post-mortem brain properties

The properties of brain tissue change significantly immediately after death [4, 45, 73–75], however the evidence for further changes during post-mortem storage is contradictory in the literature [45, 47, 76]. Zhang et al. (Dec. 2018) [77] showed that the presence of further changes during post-mortem storage is strongly dependent on the storage method, and can be largely ameliorated given the correct storage methods.

In vivo measurements of brain stiffness using MRE have consistently measured higher stiffnesses than *ex vivo* tests on brain tissue [45, 75], however pre- and post-mortem *in vivo* MRE tests found an increase of stiffness upon death of approximately 60% [73, 74].

This post-mortem change in properties is to be expected, considering that death fundamentally changes the electro-chemical activity of the brain; however the contradictory results given by the different test methods show the importance of controlling the effect of *ex vivo* testing and boundary conditions on the results obtained.

2.2 Phantom materials and ultra-soft Gels

Brain tissue can be difficult to obtain and use, so the use of phantom materials with the same properties can significantly simplify experimental procedure - particularly during the experimental validation stage. Additionally, soft polymeric gel materials are widely used as engineering polymers, and are worth study on their own account. Many of the challenges inherent to testing brain tissue are common to the testing of soft gels, and the two areas widely overlap

2.2.1 Phantom materials

Isotropic phantom materials tend to be either hydrogels[8] or Polydimethylsiloxane (PDMS, "silicone") gels due to ease of manufacture and use [25, 78–84]. More

[8]Hydrogel phantom materials used in the literature consist primarily of water, a gelling agent (such as agar, gelatine, fibrin, poly(vinyl alcohol), hyaluronic acid), and sometimes an additive (such as NaCl, alumina) in order to modify the electrical or magnetic properties of the phantom material

complex composite phantom materials have been developed in order to better mimic the structure and response of brain tissue [81], however these materials have the drawback of greater manufacturing complexity.

In addition to their use as a tissue mimicking phantom, these materials can also serve as a biological substrate (agarose being the most widely known). Being able to tune the mechanical and chemical response of a tissue substrate is particularly useful, as the mechanical properties of the tissue substrate can affect the behaviour of the cells. For example, the elastic modulus of the tissue substrate has been shown to be an important component in the regulation of cell mechanobiology [85], for instance when growing nerve cells [86]

Hydrogels can more closely mimic the electrical and thermal properties of brain tissue than PDMS phantom materials, whereas PDMS phantom materials can more easily mimic the rate-dependence of brain tissue. Additionally, PDMS phantom materials are less affected by temperature and storage time than hydrogels, making them easier to work with.

As the focus of this dissertation is the mechanical rather than the thermal or electrical properties of brain, a PDMS phantom was chosen for use when validating the experimental setup.

2.2.2 PDMS

Polydimethylsiloxane (PDMS) is a popular material used in a variety of applications [87], ranging from micro-optic systems[88, 89] and micro-mechanical sensors to micro-fluidic devices, biological substrates [90], and tissue simulants.

A particular advantage of PDMS as a phantom material is its thermal, biological, and temporal stability, as well as the wide range of achievable mechanical properties. In particular, Sylgard 184 has been widely used due to the low cost and ease with which the mechanical properties can be tailored via adjustment of the crosslink density. At low crosslink densities, PDMS retains a large percentage of uncrosslinked PDMS oil, resulting in highly viscous poro-elastic behaviour similar to that of extremely soft biological tissues. Unlike most other common tissue phantoms (such

as agar, gelatin, fibrin, PVA hydrogels or resin polymers), it is possible to achieve a range of mechanical properties representative of the entire range of tissue stiffnesses with the same material, simply by adjusting the crosslink density.

Good data on the mechanical properties of Sylgard 184 is lacking in the literature. This is shown in fig. 2.8 for instance, which shows a selection of modulus vs crosslinker data taken from the literature. There is a huge spread in the reported values, even for the nominally fully crosslinked material which is fairly stiff and relatively easy to measure. The relative spread in the data is even worse for the partially crosslinked material, likely in part due to the challenges inherent in testing soft materials.

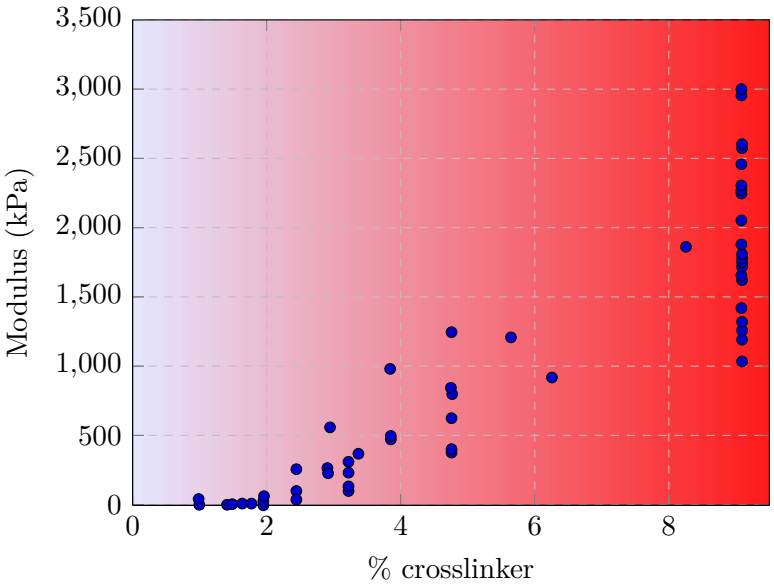


Figure 2.8: Reported Young's Modulus vs crosslinking ratio for Sylgard 184, taken from Glover *et al.* Note that for an incompressible material, Young's modulus (reported here) will be approximately 3 times the shear modulus (reported in the rest of this paper)

2.3 Test methodology

As seen above, test methodologies used in the literature broadly fall into those involving *in vivo* or *ex vivo* testing, however *ex vivo* test methods vary widely in how well they emulate *in vivo* conditions. In general, *ex vivo* testing is significantly easier to conduct than *in vivo*, however the properties of brain tissue appear to change significantly after death and during post-mortem storage [4]. For obvious clinical reasons, it is the *in vivo* properties of brain which are of interest.

2.3.1 *In vivo* mechanical testing

Magnetic Resonance Elastography (MRE) is a non-invasive method of determining the shear modulus of soft tissues [44], loading soft tissue with shear waves and recording the results with phase-sensitive Magnetic Resonance Imaging (MRI) apparatus [73]. Once the shear wave deformation has been recorded, the wave-field can be used to infer the stiffness distribution throughout the brain (or soft tissue of interest) [91].

Whilst initial MRE tests gave higher than expected stiffness values for brain tissue as well as contradictory results [44, 50], more recent tests have given more consistent results [43, 52, 74].

MRE has the advantage of being a truly[9] *in vivo* test methodology and therefore having test conditions exactly representative of real world brain behaviour. It suffers however from the following limitations:

1. Load frequency: MRE is limited in the range of allowable frequencies, and is unable to measure frequencies below approximately 5 Hz [92]. Frequencies up to 1000 Hz have been used [20], however higher frequencies result in shorter wavelengths and require more accurate imaging and higher load amplitudes. Animal testing is often conducted at higher frequencies than human testing, as potential brain damage is more acceptable in animals.

[9] In vivo indentation testing of brain tissue has been conducted [26], however the removal of the skull fundamentally changes the boundary conditions of the test - whilst the brain tissue is still living, the intercranial pressure and drainage conditions are fundamentally different from true *in vivo* conditions

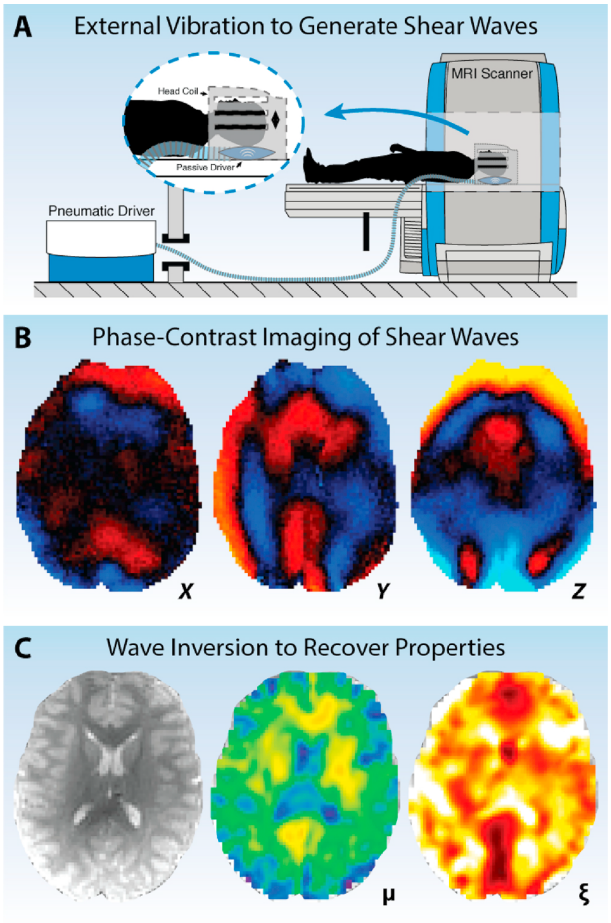


Figure 2.9: Overview of MRI elastography method adapted from [43].
A: generating shear waves in the brain via external actuation.
B: phase-contrast MRI of the resultant deformation field.
C: Extracting the mechanical property distribution from the imaged wave field.

2. Load magnitude: Particularly when used on living human subjects, MRE is limited to low amplitudes that will not cause injury to the subject. This limits the use of MRE to the low strain regime, and prevents its use in the study of TBI or similar events.

3. Assumption of linear viscoelasticity: The inversion algorithm used in MRE assumes a linear material response [20, 44, 93], which prevents testing of hyperelastic properties of brain tissue (as does the limitation on strain amplitude).

2.3.2 *Ex vivo* testing

2.3.2.1 Unconfined *ex vivo* testing of brain tissue

Testing small sections of excised brain using standard engineering test apparatus is a popular test methodology [4, 14, 20, 22, 27, 31, 35, 46, 49, 57, 58, 66, 68, 94], however *ex vivo* testing of this type has given inconsistent inter-sample results.

Figure 2.10 shows an example of this type of setup, see also fig. 2.6b. Whilst this is well suited for use with standard engineering apparatus, standard engineering test apparatus is not well suited to the testing of brain tissue. A significant portion of this inconsistency is likely to be a result of inadequate consideration of boundary conditions, drainage in particular [6]. Another source of error is the extreme softness of brain tissue: the force resolution of standard engineering test apparatus struggles to capture the low force response of brain tissue [4].

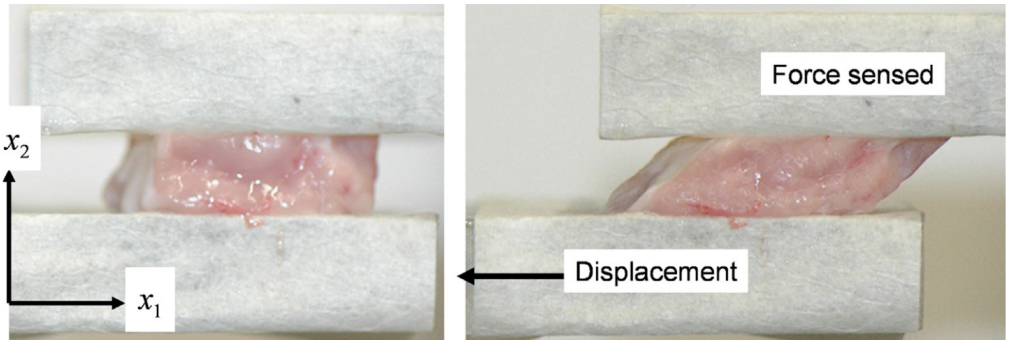


Figure 2.10: Unconfined *ex vivo* testing of brain tissue in shear by Rashid, Destrade, and Gilchrist (Dec. 2013) [57]

2.3.3 Indentation testing of brain tissue

Indentation testing of brain tissue is mathematically more complex to model than the methodologies described in section 2.3.2.1; however, indentation testing has given more consistent results [3, 26], which is likely to be a result of reduced de-watering and cell death between tests. Even indentation of slices or the surface of the brain allows for some de-watering, however, reducing how closely the test mimics *in vivo* conditions.

Under *in vivo* conditions, the brain is surrounded by cerebrospinal fluid and under mild hydrostatic pressure. This reduces de-watering of the brain under load, but also allows sections of the brain to 're-water' after partial de-watering (unlike most *ex vivo* testing, where 're-watering' cannot occur if the test environment is air).

Whilst most indentation testing in the literature has been conducted *ex vivo*, some nominally *in vivo* indentation testing has been conducted on live (anaesthetised)

subjects [26], this testing involved the removal of the skull - fundamentally changing the drainage and hydrostatic pressure conditions at the (tested) surface of the brain.

2.4 DIC and the VFM

2.4.1 DIC

Digital Image Correlation (DIC)) is a full field[10], non-contact optical measurement method capable of achieving surface deformation measurements with a displacement resolution[12] of 0.01 pixels or lower [95, 96]. This is achieved by tracking the deformation of an image via cross correlation with a reference (undeformed) image - this requires the image to have a high information content, which is often achieved via marking the surface of interest with speckles (such as those seen in fig. 2.11). Note that when speckles are applied to the surface of interest, the speckle material (e.g. paint) is in contact with the surface of the specimen, making it more accurate to characterise most DIC as a "minimal contact" rather than a "non-contact" measurement method.

The theoretical basis for DIC is not complex, but the computational and imaging apparatus necessary to make it feasible are a relatively recent phenomenon. Early practical DIC metrology was conducted by Parks and Chu, Ranson, and Sutton in the 1980s[97, 98], with DIC rapidly increasing in sophistication as computing and digital imaging technology improved. As DIC performance improved, it became more feasible to use it for material characterisation, particularly for applications where the deformation fields were complex or otherwise difficult to measure. Increasingly powerful high speed cameras have allowed for the use of DIC at higher and higher speeds, allowing for the application of DIC to high rate phenomena such as explosive loading of protective equipment[99]. The use of DIC data for material characterisation is covered in more detail in section 2.4.2.

A number of DIC calculation methods exist; a common one is to calculate the deformation field by comparing a greyscale image of the deformed object to a greyscale image of the undeformed object, and then applying a deformation field to

[10]Note that most DIC algorithms give a series of closely spaced but discrete datapoints across the surface[11] of interest, resulting in a dense dataset that is nonetheless not a truly full field measurement

[12]Note that the resolution of DIC measurements can be difficult to characterise, and it should be noted that there is an inherent conflict between displacement resolution, spatial resolution, and sensitivity to noise of the measurement [95]

the reference image such that the difference between the deformed image and the artificially deformed reference image is minimised using a cost function [95].

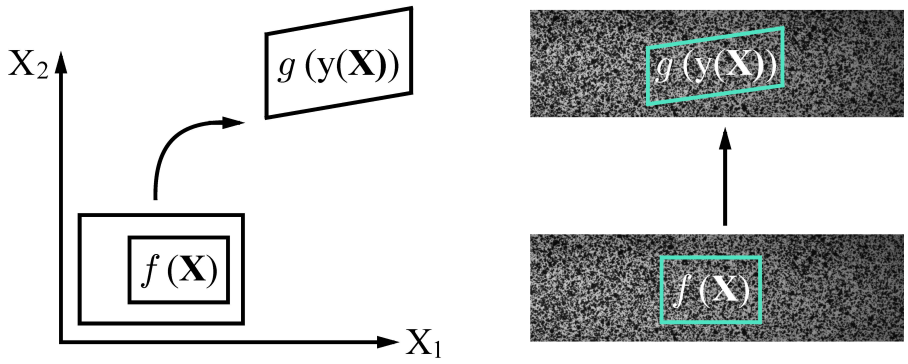


Figure 2.11: Grey scale profile of the reference image $f(\boldsymbol{X})$ and the deformed image $g(\boldsymbol{y}(\boldsymbol{X}))$. Image adapted from [100]

2.4.1.1 Cost function

Correctly selecting the cross-correlation cost function to be minimised is important. The cost function should be sensitive to deformation of the image, but not to differences in lighting or to spatial variations in brightness [101]. One of the most easily implemented cost functions is to simply use a least squares minimisation criterion, or Sum of Squares of intensity Differences (SSD), written as $C_{SSD} = \sum(f_i - g_i)^2$ where f_i and g_i are the intensity values of the reference and deformed image pixels. This method is highly sensitive to slight lighting differences between images, and weights bright areas of the image more highly than dark areas. Two more robust alternatives are the Normalised Sum of Squared intensity Differences (NSSD) and Zero Normalised Sum of Squared intensity Differences (ZNSSD) [101]:

$$C_{NSSD} = \sum \left(\frac{f_i}{\sqrt{\sum f_i^2}} - \frac{g_i}{\sqrt{\sum g_i^2}} \right)^2 \tag{2.18}$$

$$C_{ZNSSD} = \sum \left(\frac{\overline{f}_i}{\sqrt{\sum \overline{f}_i^2}} - \frac{\overline{g}_i}{\sqrt{\sum \overline{g}_i^2}} \right)^2 \tag{2.19}$$

NSSD is insensitive to the brightness of the area, but is still sensitive to offset changes in brightness (due to changes in lighting etc) [101]. ZNSSD is insensitive

to both scale and offset brightness changes, but is less accurate than NSSD when offset brightness changes are not present [101].

2.4.1.2 Deformation field

Having chosen a cost function, a method of expressing the deformation field is needed. DIC falls into two broad categories in this instance, global and local DIC [13]

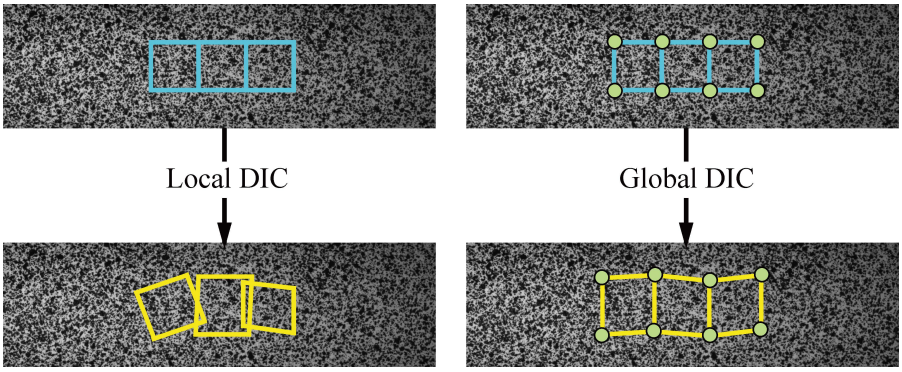


Figure 2.12: Local vs Global DIC deformation fields. Image taken from [100]

Local DIC is the most common method, and works by dividing the image up into a number of subsets and then solving for the deformation and movement of each subset independently. It should be noted that local DIC is not inherently volume-preserving, as each subset is allowed to deform independently of its neighboring subsets. In contrast, global DIC models the entire domain with a global deformation field (often but not always based on Finite Element (FE) shape functions), ensuring continuity of deformation. The question as to which method is better is application dependent; some reviews have found that global DIC achieves superior displacement and strain accuracy [102], whilst others have found that local DIC outperforms global DIC [103] in terms of measurement accuracy. Table 2.1 shows the type of problem that each approach is generally best suited to.

2.4.1.3 Speckle pattern

The DIC algorithm is highly robust, allowing for a wide range of patterns to be used. In some cases, the natural surface finish of the material has sufficient contrast

[13] Hybrid methods exist [95], but are not commonly used

Problem type	Best suited approach:	
	Local DIC	Global DIC
Crack detection	✓	
Noisy images		✓
Discontinuous deformation	✓	
Partial image loss	✓	
Low magnitude strains		✓

Table 2.1: Local vs Global DIC problem suitability

to require no additional patterning[14]. Where an artificial pattern is applied however, it is important to optimise the pattern for resolution and accuracy[107].If using local DIC, each subset requires at least three unique features (speckles) in each direction[96], in order to give a unique displacement solution[15]. For both local and global DIC, each speckle should be at least three to five pixels wide in order to avoid aliasing[16] - in practise this gives a minimum subset size of 11-21 pixels for local DIC, and limits the achievable effective spatial resolution. Note that whilst there is a hard limit on the minimum subset size, subsets can be overlapped in order to increase the effective spatial resolution.

2.4.2 The VFM

2.4.2.1 VFM overview

Standard engineering test methods such as the uni-axial tensile test have the advantage of allowing for easy analysis, but have the disadvantage of extracting only a small amount of information per test, and requiring contact measurements. This choice was logical before the advent of high fidelity full field measurement methods (such as Digital Image Correlation (DIC), Moiré interferometry, and grid methods [108]), but fails to take advantage of the rich data now available. Given the rich displacement (and by extension, strain and velocity/acceleration) data generated by DIC, the stresses in the material can be approximated under certain conditions.

[14]Examples range from glaciers [104, 105] to composite panels [106]

[15]In practice, one can sometimes get away with fewer than three speckles in each direction, but this rapidly reduces the robustness of the DIC algorithm and is not recommended

[16]An effect that occurs when the sampling frequency of a signal gets too close to the Nyquist frequency

For instance if the density of the material is known, as are the surface tractions, and the acceleration field, then the stress field can be calculated. A commonly used approach to extract material properties from experimental data is FEA inverse iteration. However, here the VFM is preferred - a particular advantage of VFM over FEA inverse iteration is that it allows one to express the inverse problem as a forward problem, resulting in a significant increase in computational efficiency [109].

2.4.2.2 Mathematical description

Consider some body occupying the domain Ω. Conservation of momentum gives rise to the following equilibrium equation:

$$\boldsymbol{\nabla} \cdot \boldsymbol{\sigma} + \boldsymbol{b} = \rho \boldsymbol{a} \tag{2.20}$$

The traction $\boldsymbol{T}$ acting on the surface S_f can be written as

$$\boldsymbol{T} = \boldsymbol{\sigma} \cdot \boldsymbol{n} \tag{2.21}$$

where

Symbol	Meaning	Order
$\boldsymbol{\sigma}$	Cauchy stress	tensor
$\boldsymbol{b}$	body force	vector
ρ	density	scalar
$\boldsymbol{a}$	acceleration	vector
$\boldsymbol{T}$	Surface traction	vector
S_f	loaded surface	
$\boldsymbol{n}$	outward facing unit normal	vector
$\boldsymbol{u}^*$	virtual displacement	vector
$\boldsymbol{\epsilon}^*$	virtual strain	tensor
V	Volume	

2.4.2.3 Virtual work

Given that eq. (2.20) apply at all points in the domain Ω, it can be multiplied by an arbitrary virtual displacement $\boldsymbol{u}^*$ in order to calculate the virtual work at any given point in the domain. Note that $\boldsymbol{u}^*$ can be arbitrary, but must be of order C^0 or higher[109]. Integrating over the domain results in the following expression for the virtual work[110]:

$$-\int_V \boldsymbol{\sigma} : \boldsymbol{\epsilon}^* dV + \int_{S_f} \boldsymbol{T} \cdot \boldsymbol{u}^* dS + \int_V \boldsymbol{b} \cdot \boldsymbol{u}^* dV = \int_V \rho \boldsymbol{a} \cdot \boldsymbol{u}^* dV \tag{2.22}$$

Because that the virtual displacement and strain functions can be arbitrary, one can chose them such that certain parts of eq. (2.22) are eliminated. Note that $\boldsymbol{\epsilon}^*$ is the spatial derivative of $\boldsymbol{u}^*$ - only one of the functions is arbitrary, as the other is dependant on it.

2.4.2.4 Problems suited to the VFM

Pierron and Grédiac (2012)[109] classify experimental solid mechanics problems into 3 types; the choice of virtual field is governed by the type of problem.

Information	**Known?**		
	Problem 1	Problem 2	Problem 3
Geometry	✓	✓	✓
Nature of constitutive equations	✓	✓	✓
Constitutive parameters	✓		✓
$\boldsymbol{T} = \bar{\boldsymbol{T}}$ over S_f	✓		✓
$\boldsymbol{u} = \bar{\boldsymbol{u}}$ over S_u	✓	✓	✓
$\boldsymbol{u}$		✓	✓
$\boldsymbol{\sigma}$			
$\boldsymbol{\epsilon}$		✓	✓

Table 2.2: Definition of the 3 types of problem as defined by Pierron and Grédiac (2012) [109]

In general, *Problem 1* consists of finding the stress, strain, and deformation of a body given the geometry, constitutive equation, and boundary conditions. These problems are commonly solved directly (via FEA when the geometry is complex), and are commonly seen during the design process. *Problem 2* consists of retrieving constitutive parameters and stresses for a body given the geometry, boundary conditions, and deformation field. Problems of this type are commonly seen during material characterisation tests, and are well suited to the use of the VFM. *Problem 3* consists of finding the boundary forces and stresses in a body, given the geometry, constitutive equation, and deformation field.

2.4.2.5 Parameter extraction and virtual field selection

Elimination of traction forces Elimination of the boundary force terms in eq. (2.22) via selection of an appropriate virtual field allows one to extract material parameters even when the boundary forces of the problem are not well known. Note of course that this approach is only useful if the acceleration fields are significant[17]. If the acceleration field is negligible and the traction is unknown, the VFM can still sometimes be used to find dimensionless stiffness values (such as Poisson's ratio, degree of orthotropy etc. [109])

Constitutive equation Having selected some material model such that the stress is written as a function of strain[18], eq. (2.22) can now be written as:

$$-\int_V \boldsymbol{\sigma}(\boldsymbol{\epsilon}) : \boldsymbol{\epsilon}^* dV + \int_{S_f} \boldsymbol{T} \cdot \boldsymbol{u}^* dS + \int_V \boldsymbol{b} \cdot \boldsymbol{u}^* dV = \int_V \rho \boldsymbol{a} \cdot \boldsymbol{u}^* dV \tag{2.23}$$

where $\boldsymbol{\sigma}(\boldsymbol{\epsilon})$ is the stress as a function of strain. Considering homogenous, isotropic, plane stress linear elasticity for simplicity, $\boldsymbol{\sigma}(\boldsymbol{\epsilon})$ becomes

$$\begin{bmatrix} \sigma_1 \\ \sigma_2 \\ \sigma_6 \end{bmatrix} = \begin{bmatrix} Q_{11}Q_{12}Q_{16} \\ Q_{12}Q_{22}Q_{26} \\ Q_{16}Q_{26}Q_{66} \end{bmatrix} \begin{bmatrix} \epsilon_1 \\ \epsilon_2 \\ \epsilon_6 \end{bmatrix} \tag{2.24}$$

where

$$Q_{11} = Q_{22} = \frac{E}{1 - v^2} \tag{2.25}$$

$$Q_{12} = Q_{21} = \frac{vE}{1 - v^2} \tag{2.26}$$

$$Q_{66} = \frac{Q_{11} - Q_{12}}{2} \tag{2.27}$$

Substituting eq. (2.24) into eq. (2.23) results in:

$$Q_{11} \int_V \left(\epsilon_1 \epsilon_1^* + \epsilon_2 \epsilon_2^* + \frac{1}{2} \epsilon_6 \epsilon_6^* \right) \mathrm{d}V + Q_{12} \int_V \left(\epsilon_1 \epsilon_2^* + \epsilon_2 \epsilon_1^* - \frac{1}{2} \epsilon_6 \epsilon_6^* \right) \mathrm{d}V = \int_{S_f} \overline{T}_i u_i^* \mathrm{d}S \tag{2.28}$$

[17] If the acceleration fields are negligible, then eliminating the traction terms from eq. (2.22) will result in $0 = 0$ – true but not useful

[18] Strain rate, hysteresis effects, etc can be included, but are excluded for simplicity in this example

Choosing two independent virtual displacement fields $\boldsymbol{u}^{*(1)}$ and $\boldsymbol{u}^{*(2)}$, eq. (2.28) can now be written as

$$\begin{bmatrix} \int_V \left(\epsilon_1\epsilon_1^{*(1)} + \epsilon_2\epsilon_2^{*(1)} + \frac{1}{2}\epsilon_6\epsilon_6^{*(1)}\right) \mathrm{d}V & \int_V \left(\epsilon_1\epsilon_2^{*(1)} + \epsilon_2\epsilon_1^{*(1)} - \frac{1}{2}\epsilon_6\epsilon_6^{*(1)}\right) \mathrm{d}V \\ \int_V \left(\epsilon_1\epsilon_1^{*(2)} + \epsilon_2\epsilon_2^{*(2)} + \frac{1}{2}\epsilon_6\epsilon_6^{*(2)}\right) \mathrm{d}V & \int_V \left(\epsilon_1\epsilon_2^{*(2)} + \epsilon_2\epsilon_1^{*(2)} - \frac{1}{2}\epsilon_6\epsilon_6^{*(2)}\right) \mathrm{d}V \end{bmatrix} : \begin{bmatrix} Q_{11} \\ Q_{12} \end{bmatrix} = \begin{bmatrix} \int_{S_f} \overline{T}_i u_i^{*(1)} \mathrm{d}S \\ \int_{S_f} \overline{T}_i u_i^{*(2)} \mathrm{d}S \end{bmatrix} \quad (2.29)$$

Choosing two independent virtual fields such that the left hand matrix in eq. (2.29) is invertible allows one to directly solve for Q_{11} and Q_{12}. Where one needs to solve for a greater number of variables, a greater number of independent virtual fields will need to be selected (linear elastic 2D orthotropy would require one to select 4 independent virtual fields for instance)

In addition to simple linear elastic material models such as the one shown above, the VFM can be used to extract parameters for non-linear material models too. Examples include elastomers [111, 112], foams [113], biological tissues, and masonry. For greater detail on the VFM, the reader is referred to Pierron and Grédiac [109] and Mei et al. [114].

2.5 Summary and motivation

Ex vivo mechanical testing of brain tissue is particularly challenging, and has resulted in a wide spread of (sometimes contradictory) results in the literature:

1. Brain tissue's extreme softness makes contact based measurement of stress and strain difficult to conduct accurately,

2. Brain tissue's extreme sensitivity to boundary conditions (drainage in particular) makes it difficult to emulate *in vivo* conditions via *ex vivo* testing.

This dissertation solves the above problems by using Digital Image Correlation (DIC) for non-contact stress and strain measurement, and a novel experimental setup for improved control of boundary conditions. This setup (described and validated in detail in chapter 4) solves the boundary condition problem whilst allowing for a wide range of loading frequencies and amplitudes. It should be noted that MRE solves the above problems, but can test only a small range of strains and frequencies.

3 Methodologies

As discussed in chapter 2, current test methodologies suffer from both measurement difficulties[1] and poor control of boundary conditions when measuring brain tissue. Through the use of non-contact stress and strain measurements (through the VFM and DIC respectively) and the use of a novel loading apparatus, these problems can be solved.

3.1 Metrology and Loading

3.1.1 Measurement and analysis

Given the extreme softness of brain tissue, non-contact stress measurement is the logical choice – in this case DIC. The DIC setup and processing settings are slightly different for testing on various soft materials, but all make use of the same 200mm lens and Photron high speed camera, as well as MatchID DIC software. For more details on the DIC for high rate imaging setup, the reader is referred to chapter 4, where the DIC setup is covered in detail, as well as significant analysis around sensitivity and accuracy for the DIC setup chosen.

Whilst chapter 2 covers the fundamentals of the VFM, the specific form used is discussed in chapter 4, along with a worked example and a mathematical derivation of the validity of the quasi-1d dynamic VFM setup. This same dynamic VFM

[1] Due to the extreme softness of brain tissue

analysis is used for the rest of the high rate testing throughout this thesis, with the exception of the static VFM in chapter 7. The static VFM in chapter 7 is instead conducted via MatchID software, rather than custom python code.

3.1.2 Loading

In order to characterise brain tissue under deviatoric loading, it is particularly important to load it under as pure a deviatoric loading as possible, without dilatational stresses. In order to do this, a cylindrical specimen is loaded in harmonic torsion, generating purely shear loading with no dilatational stresses. This apparatus and methodology is described in detail in chapter 4, including theoretical calculations, FEA simulations, and experimental results.

3.2 Phantom selection and characterisation

In order to commission this new apparatus, it is necessary to first have a "phantom" material with which to validate the apparatus. Brain tissue can be difficult to obtain and use, so the use of phantom materials with similar properties can significantly simplify experimental procedure - particularly during the experimental validation stage. The purpose of this phantom material is to have known, stable mechanical properties similar to brain tissue, such that testing can first be conducted on this material, allowing for both an easier set of initial tests[2] and baseline properties which the results can be compared to.

Isotropic phantom materials tend to be either hydrogels[3] or polydimethylsiloxane (PDMS, "silicone") gels due to ease of manufacture and use [25, 78–84]. More complex composite phantom materials have been developed in order to better mimic the structure and response of brain tissue [81], however these materials have the drawback of greater manufacturing complexity.

3.2.1 Selection of Phantom material

Hydrogels can more closely mimic the electrical and thermal[79] properties of brain tissue than PDMS phantom materials, however PDMS phantom materials can more easily mimic the rate-dependence of brain tissue. Additionally, PDMS phantom materials are less affected by temperature and storage time than hydrogels, making them easier to work with[81].

As the focus of this dissertation is the mechanical rather than the thermal or electrical properties of brain, a PDMS phantom was chosen for use when validating the experimental setup.

Two ultra-soft PDMS gels from Smooth-On were selected and tested for suitability. The two PDMS rubbers (Ecoflex 00-10 and Ecoflex GEL) have nominal

[2]without the challenges inherent to biological tissue, such as refrigeration, sanitation, etc

[3]Hydrogel phantom materials used in the literature consist primarily of water, a gelling agent (such as agar, gelatine, fibrin, poly(vinyl alcohol), hyaluronic acid), and sometimes an additive (such as NaCl, alumina) in order to modify the electrical or magnetic properties of the phantom material[44, 69, 78, 115]

shore hardnesses of 00-10[116] and 000-35[117] – see fig. 3.1 for an example of how stiff various shore hardnesses are. These materials can be further softened by the addition of a silicone thinner[118], which has the added advantage of increasing cure time and pot-life whilst decreasing uncured viscosity.

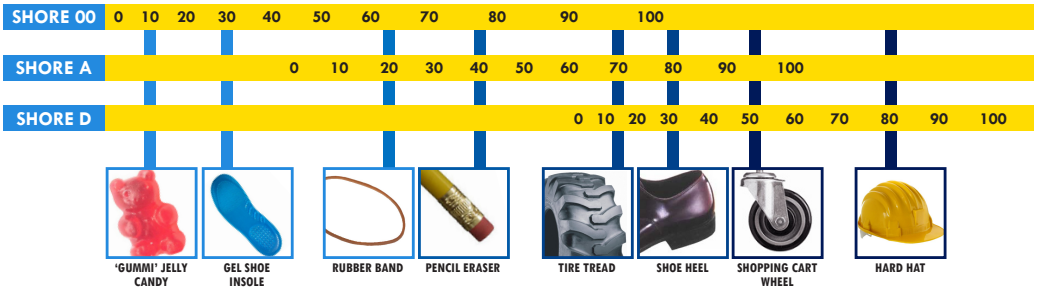


Figure 3.1: Shore hardness of various common polymers - note that Ecoflex 00-10 is at the bottom of the range of the scale, and Ecoflex GEL is softer than the measurement scale. Image taken from [119]

3.2.2 Mechanical characterisation of selected phantom

3.2.2.1 Casting of material

Both the Ecoflex 00-10 and the Ecoflex GEL were cast at room temperature (25°C) with a volume ratio of thinner:A:B of 10:45:45 following the manufacturer's instructions[4].

When casting the silicone in flat sheets, it was found that degassing was not needed. Once the height:depth ratio of the mould was greater than approximately 1:1[5], degassing was needed in order to prevent bubbles. Cure time for Ecoflex 00-10 and Ecoflex GEL was stated by the manufacturer to be 4 hours and 2 hours respectively; both polymers were allowed to cure for a full 24 hours in order to ensure full curing.

In order to guarantee that the silicone was fully cured and to investigate possible transition temperatures, a cured sample was loaded into a Differential Scanning

[4]The maximum allowable percentage thinner is 10%, limiting how much the material can be softened by. Even at 10% thinner, the thinner was found to gradually seep from the cured material if it was left on a porous surface (such as a sheet of paper) for an extended period of time (several days). As a result, thinner percentages above 10% were not investigated.

[5]I.E. when casting deep shapes or tubes rather than simple flat sheets

Parameter	Range	Steps	Spacing
Freq (Hz)	0.01 – 100	21	log
Temp(°C)	-20 – 25	10	linear
Amplitude	0.05% – 0.2%	4	linear

Table 3.1: Test parameters for shear DMA on silicone gel

Calorimeter (DSC) and cycled from 20° C to −90° C at various heating and cooling rates, before finally being heated to 40° C and held there.

This testing showed no significant further curing of the sample even at elevated temperatures[6]. Additionally, it was found that the glass transition temperature of the material lay at approximately −65 to −75° C when cooling[7] and at −40° C when heating. This temperature is well below those anticipated during use as a phantom material. This is useful to know, as it means that the specimen will not undergo a glass transition during use as a phantom material, making the properties more consistent and the material more useful as a reliable phantom.

3.2.2.2 Shear characterisation via Rheometry and TTS

In order to characterise the shear response of the material, DMA Rheometry was used to measure the shear storage and loss moduli over a range of temperatures and frequencies. Tests were also conducted over a range of amplitudes, in order to ensure that the testing was occurring in the linear regime. The test parameters and methodology are shown in table 3.1 and listing 3.1 respectively.

Listing 3.1: Rheometer test methodology

```
set T = -20 #Wait to equilibrate (according to Rheometer's inbuilt
    functionality)
wait(5 mins) #Margin of error to ensure equilibrium
for T in range(-20:25:5):#running from -20 to 25 in 5 C steps
wait(5 mins) #margin of error to ensure temperature equilibrium
for Amp in range(0.05:0.2:0.05): #running from 0.05% strain up to 0.2%
    strain in steps of 0.05%
wait(1 min) #Ensuring that the sample is fully adhered to the rheometer
    head
```

[6] If the sample was undergoing chemical reactions, this would be shown on the DSC results as an increase/decrease in energy independent of heat capacity. In combination with curing the specimens for 6-12 times longer than the quoted cure time, this showed that the specimen was no longer undergoing any significant curing.

[7] Faster cooling rates led to a delayed transition

```
for freq in range(0.01:100): #Run from 0.01 Hz up to 100 Hz (log spacing)
record loss and storage moduli
```

3.2.2.3 Results

Slipping of the Rheometer head appeared to occur at high frequencies: as a consequence, test results for frequencies above 10 Hz were ignored. In general, a sharp drop in storage modulus with frequency, an increase in tangent delta, and noisy data are often signs of slipping. This can be confirmed by re-running the test with higher normal force or smaller shear magnitudes – if the apparent slipping occurs later, then it is likely that the phenomenon is slipping of the rheometer head. Figure 3.2 shows this behaviour for low amplitude loading (where slipping is minimised) at both low and high temperatures.

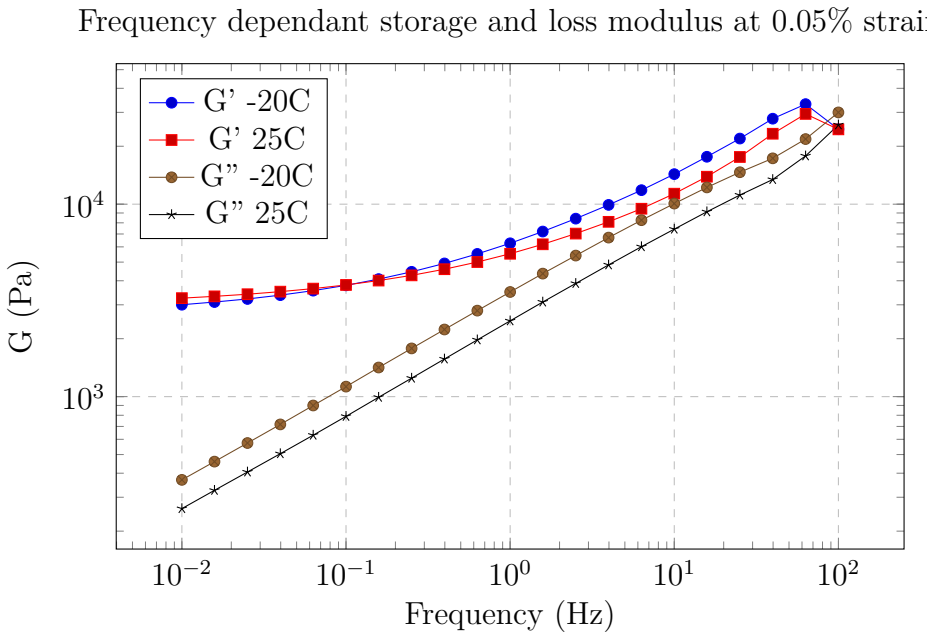


Figure 3.2: Example of a test where slipping occurred at high frequencies - note the sudden drop in storage modulus in particular. When testing at higher strain amplitudes, slipping occurred earlier as a result of increased forces.

Temperature dependence of this material behaves as expected for the loss modulus, however the storage modulus gives counter-intuitive results – the elastic branch of the material appears to increase in modulus as the temperature increases.

This behaviour is predicted by thermodynamics, and so entirely explainable, if unintuitive given that this behaviour is seldom experienced outside of the lab. Figure 3.3 shows the frequency dependent loss and storage moduli at various temperatures - note the behaviour of the storage modulus at low frequencies.

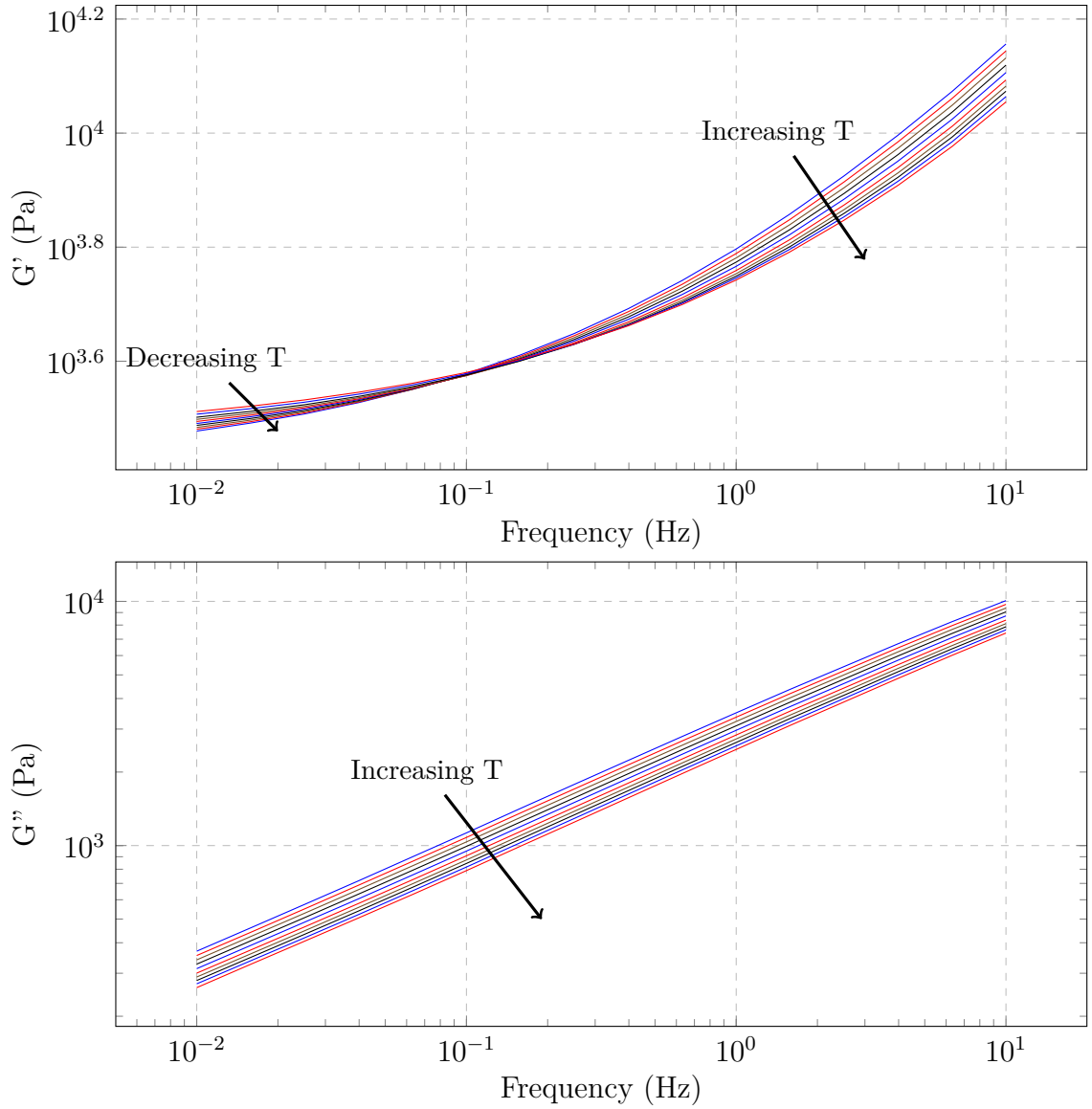


Figure 3.3: Shear storage and loss moduli for Ecoflex GEL over a range of temperatures and frequencies

Whilst the loss modulus decreases with temperature for a fixed frequency, the storage modulus does not. This is thought to be as a result of the elastic branch of the polymer stiffening with increasing temperature, unlike the viscous

branches. This causes the storage modulus to increase with temperature at low frequencies (where the storage modulus is primarily due to the elastic branch), but decrease with temperature at high frequencies (where the viscous branches dominate the storage modulus).

Based on the work of Williams, Landel, and Ferry (1955) [120], Time Temperature Superposition (TTS) can be used to express the data shown in fig. 3.3 in terms of frequency alone, using shift factors. These shift factors are shown in fig. 3.4 - note that even a 45° C shift result in a frequency shift of approximately a third of a decade. As a result, the loss modulus TTS mastercurve will be almost identical to the curve from a single test in fig. 3.3, but with a frequency range of 3.3 decades rather than 3 decades. The downside of this stability is that it prevents one from effectively using TTS to characterise the material, however a significant upside is the stability of the material. Small changes in temperature during the test will have minimal effect on the behaviour of the material, making it easier to work with.

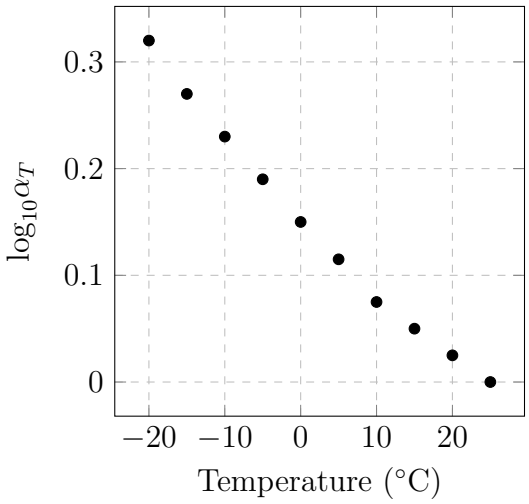


Figure 3.4: Shift factors vs temperature for Ecoflex GEL, taking 25° C to be reference temperature

Suitability as a phantom material

The above tests show that this is a suitable phantom material for deviatoric testing, as it exhibits similar mechanical behaviour to brain tissue, but is significantly easier to work with - it is almost unaffected by temperature, and is biologically inert.

Given that brain tissue has a shear modulus of approximately 1-2 kPa[14], this phantom material is slightly stiffer than brain tissue, but still sufficiently close to be useful as a phantom material – particularly when commissioning and validating test methodologies for ultra-soft materials.

Not only is this material useful as a phantom for brain tissue, it is useful in its own right. Soft and ultrasoft materials are widely used as energy absorbing materials, however they are challenging to characterise at high rates. Characterising this material and others like it extends the range of high quality material data available in the literature, and allows for more accurate design and simulation of energy absorbing components and structures.

4

Validation of apparatus and methodology

This chapter takes the form of a paper, focusing on the development, commissioning, and validation of a novel apparatus and analysis methodology for the high rate mechanical characterisation of ultra-soft materials.

A mathematical worked example and derivation of the analysis is conducted, followed by FEA simulations showing the validity of the analysis technique. This is followed by results for experiments conducted on an ultra-soft polymer at high rates.

The apparatus and analysis technique shown in this chapter formed the basis of the DPhil, with the following 2 chapters using this same technique on more complex materials.

Characterising the frequency-response of ultra-soft polymers with the Virtual Fields Method

Aaron Graham*, Clive Siviour

Department of Engineering Science, University of Oxford, UK

Abstract

This paper presents a novel apparatus, combined with application of the Virtual Fields Method (VFM) for the high frequency characterisation of the mechanical response of ultra-soft materials. The viscoelastic response is characterised under harmonic deviatoric loading at a range of frequencies using the dynamic VFM in the frequency domain. Obtaining useful high rate data on soft materials is challenging using typical test methodologies, as the low speed of sound in the material makes stress equilibrium difficult to obtain; additionally, the low stiffness results in small stresses and weak measurement signals. This novel apparatus and analysis method has been shown capable of obtaining important material characterisation data that would be impossible to access using currently existing test techniques.

Keywords: Digital Image Correlation, Frequency response, Mechanical characterisation, Soft materials, Virtual Fields Method

1. Introduction

Soft materials may be defined as materials that have low mechanical stiffness and strength, and include polymers, foams, and biological tissues [1]. These materials are widely used in applications in which large amplitude dynamic or impact deformations are experienced; however, there is a paucity of data on their properties at high strain rates and frequencies when compared to metals and ceramics. One reason for this is that they are challenging to characterise under these loading conditions [1, 2, 3, 4].

Typical engineering test methodologies rely on the inertial stresses in the specimen being negligible in comparison to the strain induced stresses[5, 6]; however, the low modulus to density ratio of soft materials makes this difficult to achieve in high rate characterisation experiments, because the speed of sound in the material is low. Additionally, owing to the low stiffness and strength, stresses are small[1]; this causes difficulty in measurement of the stress state using conventional stress measurement techniques.

The above limitations can be partially mitigated via adaptation of standard test methodologies. Approaches such as Dynamic Mechanical Analysis (DMA) and Rheometry can adequately solve the problem with low forces, but struggle to obtain data at frequencies above 50-100 Hz. At higher rates, the use of semi-conductor strain gauges and very thin specimens on a Split Hopkinson Pressure Bar (SHPB) partially mitigates problems with weak transmitted signals and specimen stress equilibrium respectively [1]. These adaptations can lead to other issues, however, such as the exacerbation of radial inertial effects.

The behaviour of polymers outside the envelope of testable strain rate regimes can be predicted via Time Temperature Superposition (TTS) [7, 8], where changes in rate can be related to changes in temperature. This allows for the high rate behaviour of a material to be predicted from low rate low temperature data [9, 10]; however, there are some significant limitations to this method. TTS is mainly validated for small amplitude loading in which the polymer response remains linear viscoelastic: it is only recently that this approach has been shown to work for larger strains [8]. Furthermore, some polymers (such as the one tested in this paper) exhibit low sensitivity to temperature, and some materials (such as biological tissue) degrade when taken outside of a narrow range of temperatures[2, 11, 12]. This means that TTS is of limited utility for these materials.

A further limitation of standard engineering test methodologies is the assumption of homogeneity: detection of material heterogeneity or specimen strain localisation, for example, requires a form of full-field measurement[13]. Additionally, if 1D tests are used, multiple tests are required in order to detect material anisotropy[14, 15]. As a result, inter-specimen variability can cause errors when quantifying effects of of inter-test changes such as specimen orientation or location. In order to overcome these limitations, the use of full-field measurements allows for the direct measurement of heterogeneity[15], and the use of the Virtual Fields Method (VFM, further described below) can allow for multiple model parameters to be extracted from a single test [16]. Additionally, VFM analysis can be designed

*Corresponding author
Email address: Aaron.Graham@eng.ox.ac.uk (Aaron Graham)
[1]on the order of Pa

to make fewer assumptions about specimen stress equilibrium or deformation state, allowing for greater flexibility in the choice of test boundary conditions.

Ultra-soft materials such as biological tissue often have a shear modulus (μ) that is orders of magnitude lower than the bulk modulus (K): e.g. for brain tissue $\mu \approx 2\times10^3$ Pa and $K \approx 2 \times 10^9$ Pa. This means that low rate measurements of the Young's modulus will effectively measure the shear modulus[2], and high rate measurements of the Young's modulus will measure the shear modulus plus an error due to inertial effects. As a result, tests to establish Young's modulus are not particularly valuable: testing should instead focus on separating the deviatoric and the dilatational response, particularly if high rate characterisation is required. Additionally, the large difference in deviatoric and dilatational moduli results in a large difference in the related wave-speeds; as a result, the specimen may be in longitudinal (static) stress equilibrium fairly early in the test, but may not reach shear stress equilibrium before the test is over. Hence, when characterising the shear response of soft materials, it is important that the dilatational loading is accounted for.

In order to adequately characterise the frequency-response of an ultra-soft material at high rates, a novel experimental apparatus has been designed and built. Stress and strain measurements are non-contact, in order to allow for the testing of ultra-soft materials, and full-field, in order to allow for spatial discretisation of heterogeneous material properties. An important component of the designed experimental apparatus is the use of the VFM, described in the next section.

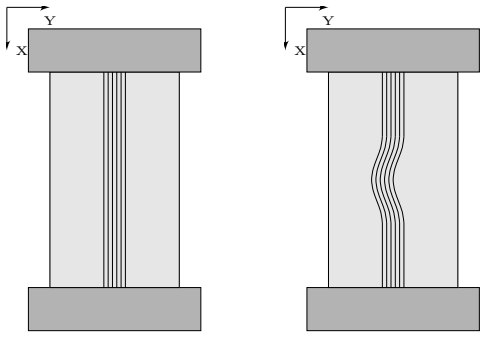
1.1. The Virtual Fields Method

High fidelity full-field measurement methods such as DIC, Moiré interferometry, and grid methods provide rich experimental data, however standard engineering test methodologies such as the uniaxial tensile test fail to fully exploit these [17]. In contrast, the VFM allows one to take advantage of this rich dataset, enabling the extraction of multiple material parameters (and their spatial distribution) from a single experiment. This allows one to obtain material parameters from far fewer tests than traditionally required – a particular advantage when specimens are difficult or expensive to obtain.

Furthermore, traditional engineering test methods that rely on measurements of forces or displacements at a small number of discrete locations assume a given stress distribution, and give results of reduced quality when these assumptions are not correct. The VFM allows for a heterogeneous stress state, indeed heterogeneous stress states are desirable[3], as they allow for the extraction of multiple material parameters from a single experiment [14]. The VFM is based on the Principle of Virtual Work (PVW), which can be manipulated to remove the effect of traction or acceleration terms – something that is particularly valuable for dynamic characterisation. In practice, removal of the traction term allows one to use the specimen inertia as a virtual load cell: rather than trying to obtain static stress equilibrium, the dynamic acceleration field is used to the advantage of the researcher[18].

Worked example

In order to demonstrate the use of the VFM in dynamic simulations, a simple worked example is helpful. Consider a homogeneous linear elastic cylindrical rod, with a density $\rho = 1000$ kg/m^3, shear modulus $\mu = 4000$ Pa, shear wavespeed $c_s = \sqrt{\mu/\rho} = 2$ m/s, and length $L = 10$ mm. Both ends are fixed in place using rigid clamps. Under the chosen loading, the bottom clamp is oscillated in rotation at 500 Hz for 2 ms such that the displacement amplitude at the surface of the specimen is A. The surface rotational displacement of the loaded end is given by $u(t) = A(\cos(1000\pi t) - 1)$ until $t = 2$ ms, after which the loaded end is stationary. After 3.5 ms, the distribution of surface displacements along the specimen length is as shown in fig. 1:



(a) $t = 0$ ms (b) $t = 3.5$ ms

Figure 1: Horizontal component of surface displacement field in the region of interest at times 0 and 3.5 ms respectively. Displacement magnitude is greatly exaggerated for clarity. Region of interest shown on specimen by hatched region

Considering a thin, quasi-1D strip at the surface of the sample: if the upper end were unclamped, shear stresses along the length could simply be calculated via direct integration of the dynamic equilibrium equation[4] from the free end of the sample. However, if the end is not free and the distribution of traction forces is unknown (or if the displacement field is not known for the entire domain), the full VFM is required.

The virtual work equation is obtained by multiplying the dynamic equilibrium equation through by a compatible virtual displacement and strain to give [14]:

[2] $E_y = \frac{9K\mu}{3K+\mu} \approx 3\mu$ where $K \gg \mu$

[3] It should be noted however that VFM using DIC data typically needs to make an assumption about the through thickness stress. A heterogeneous through thickness stress distribution is not desirable

[4] $\nabla\boldsymbol{\sigma} = \boldsymbol{b} + \rho\ddot{\boldsymbol{u}}$. The divergence of the stress tensor is equal to the sum of the body force and the density times the acceleration field

$$\underbrace{-\int_V \boldsymbol{\sigma} : \boldsymbol{\epsilon}^* dV}_{\text{Internal virtual work}} + \underbrace{\int_{S_f} \boldsymbol{T} \cdot \boldsymbol{u}^* dS}_{\text{External virtual work}} = \underbrace{\int_V \rho \ddot{\boldsymbol{u}} \cdot \boldsymbol{u}^* dV}_{\text{Acceleration virtual work}} \quad (1)$$

where the terms are as follows:

$\boldsymbol{\sigma}$	Cauchy stress	$\boldsymbol{b}$	body force
ρ	density	$\ddot{\boldsymbol{u}}$	acceleration
$\boldsymbol{T}$	Surface traction	S_f	loaded surface
$\boldsymbol{n}$	outward facing unit normal	$\boldsymbol{u^*}$	virtual displacement
$\boldsymbol{\epsilon}^*$	virtual strain	V	Volume

In quasi-static experiments the inertial contributions to the stress field (i.e. acceleration virtual work in eq. (1)) are negligible, and this term can be neglected – material characterisation is instead done by accurately measuring the surface tractions. In contrast, acceleration terms are often significant in dynamic experiments, and surface tractions can be difficult to measure: appropriate selection of the virtual field can eliminate the traction terms as follows.

Firstly, a virtual displacement field, $\boldsymbol{u}^*$, is chosen such that only one component ($\boldsymbol{\epsilon}^*_{XY}$) of the compatible virtual strain tensor is non-zero. This, combined with the quasi-1D nature of the deformation field[5], allows one to analyse the problem in only one dimension. In 1D linear-elastic shear, with $\boldsymbol{\sigma} = \mu\boldsymbol{\epsilon}$, eq. (1) becomes:

$$\underbrace{-\int_{X_0}^{X_1} \mu\boldsymbol{\epsilon} : \boldsymbol{\epsilon}^* dX}_{\text{Strain gradient term}} \underbrace{- T(X_0)\boldsymbol{u}^*(X_0) + T(X_1) * \boldsymbol{u}^*(X_1)}_{\text{Traction term}} = \underbrace{\int_{X_0}^{X_1} \rho\ddot{\boldsymbol{u}} \cdot \boldsymbol{u}^* dX}_{\text{Inertial term}} \quad (2)$$

where X_0 and X_1 are the boundaries of the domain, and μ is the shear modulus. Careful selection of the virtual displacement allows the traction force term to be eliminated from eq. (2). The virtual field used by [13, 19] can be adapted for shear:

$$\begin{cases} u^*_Y = X(X-L) \\ u^*_X = 0 \end{cases} \Rightarrow \begin{cases} \frac{\partial u^*_Y}{\partial X} = 2X - L \\ \frac{\partial u^*_Y}{\partial Y} = \frac{\partial u^*_X}{\partial Y} = \frac{\partial u^*_X}{\partial X} = 0 \end{cases} \quad (3)$$

where u^*_X and u^*_Y are the virtual displacements in the X and Y directions respectively. This eliminates the traction force term, resulting in:

$$\mu = \frac{\int_{X_0}^{X_1} \rho\ddot{\boldsymbol{u}} \cdot \boldsymbol{u}^* dX}{-\int_{X_0}^{X_1} \boldsymbol{\epsilon} : \boldsymbol{\epsilon}^* dX} \quad (4)$$

[5] See Appendix D for more detail on the quasi-1D nature of the problem

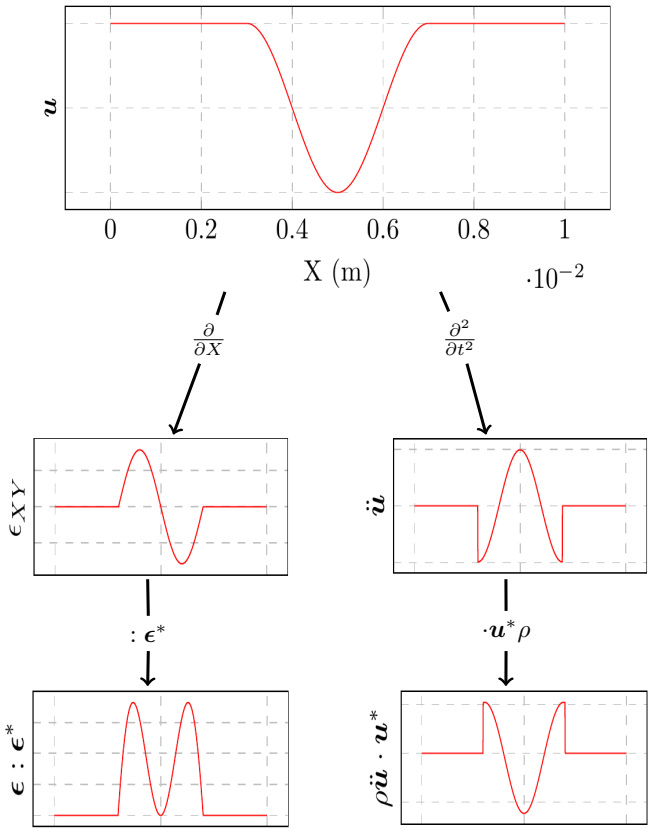


Figure 2: Plot of the displacement field, and derived temporal (acceleration, VFM inertial term) and spatial (strain, VFM strain gradient term) fields for the problem described in fig. 1. Full plots with numerical values, as well as equations describing the various fields are shown in Appendix B.

Substituting the displacement fields described in fig. 1 and the virtual displacement fields described in eq. (3) into eq. (4) at time $t = 3.5$ ms results in:

$$0.08\mu = 320$$
$$\mu = 4000 \text{ Pa}$$

giving a predicted shear modulus of 4 kPa – this matches the given material parameters. Figure 2 shows the shape of the displacement, strain, acceleration, and virtual work fields at time $t = 3.5$ ms; plots with numerical values and more detail are shown in Appendix B.

Analysis in the frequency domain

As the purpose of this experiment is to investigate the frequency-response of soft materials, it is logical to examine the data in the frequency domain rather than the time domain. To this end, a Fast Fourier Transform (FFT) is used to obtain the strain and acceleration for each location on the observed specimen surface in the frequency domain. This allows eq. (4) to be solved in the frequency domain, directly obtaining the visco-elastic frequency dependant complex modulus for each frequency in terms of

the frequency domain acceleration and strain components:

$$\tilde{G}(f) = G' + iG'' = \frac{\int_{X_0}^{X_1} \rho \tilde{\ddot{\boldsymbol{u}}}(f) \cdot \boldsymbol{u}^* dX}{-\int_{X_0}^{X_1} \tilde{\boldsymbol{\epsilon}}(f) : \boldsymbol{\epsilon}^* dX} \quad (5)$$

Here, both strain and acceleration are now complex valued and selected for a single frequency only, giving the complex shear modulus for that frequency f. The apparatus is designed to excite a 'pure' frequency, making almost all of the signal reside on a single frequency band. As a result, the noise-floor can be raised, allowing other frequencies to be readily discarded as noise rather than weak signals.

2. Experimental Design

2.1. Apparatus

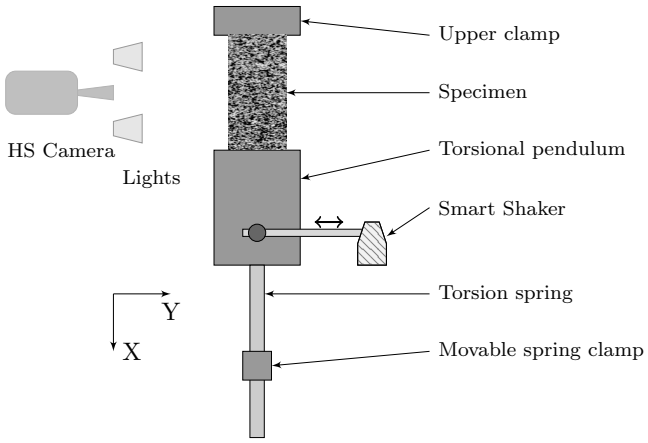


Figure 3: Experimental apparatus used for torsional loading of samples

Loading device

The loading device (shown in fig. 3) consists of a torsional pendulum with a tunable resonant frequency, driven by a pair of programmable smart shakers. The spring clamp can be moved in order to change the effective length of the torsion spring, allowing one to tune the resonant frequency of the device. The upper clamp can be rotated, allowing for the specimen to be preloaded if needed. This clamp provides a static displacement boundary condition[6] with a wide range of allowable (quasi-static) motion. The lower clamp provides a displacement boundary condition with a limited range of motion, but a wide range of possible frequencies. The device was designed to use two interchangeable masses on the torsional pendulum, in order to provide for a larger range of resonant frequencies than would be obtainable via the changing of the spring length alone; however, the experiments conducted for this paper made use of the low frequency head only. For the current setup, the maximum oscillatory displacement is limited by the performance of the Smart Shaker pair; if greater displacements are required, the location of the smart shaker pair can be changed.

If the experiment does not aim to probe a large range of macroscopic strain states, then the upper clamp can be omitted. This omission provides a stress-free boundary condition at the upper surface of the specimen, obviating the need for the full VFM – stresses can instead be obtained via simple integration of the acceleration field.

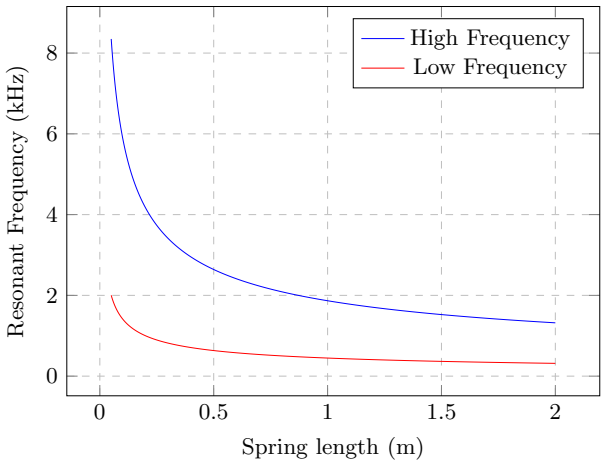


Figure 4: Range of obtainable resonant frequencies using the high frequency (light) or low frequency (heavy) pendulum head

Data acquisition

In order to obtain DIC images, a Photron FASTCAM SA-X2 1080K-M4 camera is used, running at 25 000 fps using a lens of 200 mm focal length. Light is provided by four custom built LED lights, and glare is avoided via the use of cross-polarisation. To achieve this, vertically oriented linear polarisers were placed on the lights, and a horizontally oriented linear polariser film was mounted on the lens. The light arriving on the specimen is vertically polarised: specular reflection (glare) does not change the polarisation of the light, allowing the horizontal polariser filter on the camera to remove glare (and hence over-exposure of the image). In contrast, diffuse reflection (the actual image) randomises the polarisation of the light, allowing it to pass through the horizontal polariser filter on the camera. For further detail on this technique, the reader is referred to [20]. The downside of this method is that significant amounts of light are inevitably lost in the double polariser filters, requiring the use of brighter lights than would otherwise be required. An alternative method for avoiding specular reflection is to instead ensure that the surface of the specimen has a matte finish (via the application of talc powder for instance), however this is

[6] The acoustic impedance of the specimen is negligible in comparison to the acoustic impedance of the upper and lower clamps, allowing the boundary conditions to be modelled as displacement boundary conditions

not always possible, particularly when imaging biological samples.

Specimen preparation

Samples consisted of an ultra-soft platinum cure Poly-DimethylSiloxane (PDMS, silicone) elastomer sourced from Benam Chemicals, England. Both EcoFlex GEL and EcoFlex 10 were used, exhibiting nominal Shore hardnesses of 000-35 and 00-10 respectively. The Ecoflex gel was mixed with 10% thinner by weight, in order to increase pot-life and further decrease the shear modulus. Both polymers are normally transparent, however 0.5wt% black pigment was added to both, in order to allow adequate imaging quality for DIC. The casting procedure was the same for both: vacuum degassing at approximately 5 kPa (absolute) followed by curing at 20 °C for 24 hours. The silicone exhibited no observable volume change while curing (less than 0.1%, according to the manufacturer's datasheet [21, 22]). Samples all had a diameter of 30 mm and a height of approximately 70 mm. The region of interest was near the bottom of the specimen, however the extra length above the region of interest reduced the magnitude of waves reflected from the top of the specimen. This extra length was not needed, and can be neglected, however it makes the experiments slightly easier to run.

Specimens for rheometer testing were cast in flat sheets of 3 mm thickness from which circles were cut with a punch once curing was complete. Specimens for use in the new apparatus were cast in smooth cylindrical moulds, and extracted once curing was complete. The speckle pattern was then applied with an airbrush, using a silicone based paint. This paint consisted of approximately 50 wt% white silicone pigment, 20 wt% silicone thinner, and 30 wt% of the same silicone used for the samples.

2.2. Experimental procedure

The frequency response of the material was probed at a variety of frequencies. First, the specimen was fixed in the clamps, and reference images of the (static) specimen were taken. After each change in loading state (oscillation frequency or oscillation magnitude), this state was held for at least 60 s before any data were recorded, in order to allow for high frequency relaxations to occur. In the experiments reported here, the static (DC) strain state of the specimen was not varied; however, the apparatus is capable of doing so. It is intended to include this change in future experiments in order to evaluate the hyper-viscoelastic frequency response of specimens.

2.3. Data extraction

MatchID DIC software was used to convert video to spatial data. The strain, displacement, and acceleration data were extracted directly from the DIC software. Whilst the domain was idealised as 1D, in reality the imaging domain was 1024 pixels long and 384 pixels wide. The displacement along the central 150 pixels in the width direction were averaged in order to obtain the central displacement – this had the effect of significantly reducing noise without affecting signal quality.

Table 1 shows the imaging parameters as well as the processing parameters used when calculating the deformation and the spatial and temporal derivatives (strain and acceleration). After extraction from the DIC software, the strain and acceleration data were transformed from the temporal domain to the frequency domain via an FFT, resulting in complex valued data at a range of frequencies for each spatial point.

Camera	**FASTCAM SA-X2 1080K-M4, Photron**
Pixel depth	12 bits
Camera noise	0.45%
Spatial resolution	0.0084 pixels
DIC software	MatchID 2020.1.1
Field of view (px)	1024×384 pixels
Field of view (mm)	28.4×10.7 mm
Average speckle size	4.1 pixels
Interframe time	40 μs
Subset size	25×25
Subset spacing	5
Spatial smoothing	none
Correlation method	ANSSD
Pixel interpolation	Bicubic Spline
Subset shape function	Quadratic (12 parameter)
Correlation threshold	0.9 (90%)
Image prefiltering	Gaussian, kernel 5
Strain window	5
Strain interpolation	Q9
Acceleration interpolation	Quadratic moving window width 5

Table 1: Imaging and DIC specifications

2.4. Simulations

Prior to commencing experiments, the proposed experimental setup was simulated using Abaqus© FEA software. The nodal displacements from this simulation were then fed through the analysis chain in order to validate the feasibility of the proposed experimental setup. Once this step was validated, the full experimental setup and analysis chain (including DIC) was simulated as shown in fig. 5. A photo of a specimen was taken using the same camera as used in the experiments, and the camera optics were calibrated. Calibration is performed by taking images of calibration plates with known dimensions in order to generate a mapping between image co-ordinates in pixels and real-world spatial co-ordinates. The nodal deformations from the FEA simulation were then used in conjunction with the camera calibration data to deform the speckled image. Note that this simulated image deformation took

full 3D optical effects into account. These artificially deformed images were then analysed using DIC in order to extract displacement data, and this displacement data was then fed into the analysis chain. Artificial deformation of images was conducted using MatchID's FE-Def module, as was DIC reconstruction of the deformation fields. All cameras have some inherent noise associated with the images – the camera used for these experiments had a grey-scale noise level of approximately 0.45% of full scale. The effect of noise on the obtained material parameters will be explored in section 4.

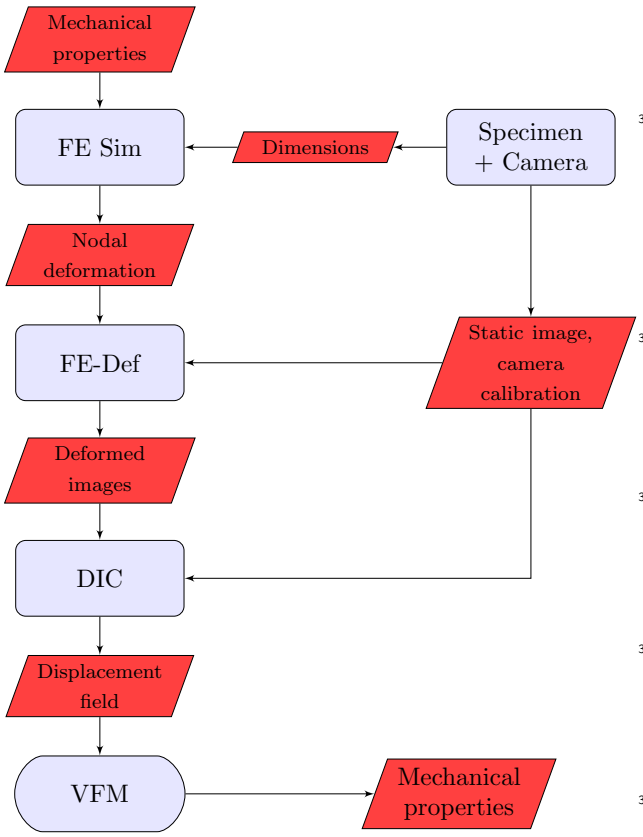


Figure 5: Flowchart showing simulation procedure for test method validation.

Simulation results

The simulation performed was of an experiment in which the frequency of oscillation was 1 kHz, and the surface displacement amplitude 0.033 mm. The specimen was allowed to reach steady state before the deformation state was recorded, in order to emulate the proposed experimental protocol. The frequency dependent storage (19.6 kPa) and loss (4 kPa) moduli at 1 kHz were directly input to Abaqus, in order to allow for direct comparison with the material properties calculated by the VFM. Each element was 150 μm in size, approximately equivalent to 5 pixels. An Lagrangian formulation using C3D8R elements and a linear visco-elastic material model was used, and Abaqus's Explicit Dynamic solver used for the dynamic simulations. In this simulated experiment, data were recorded for only 1 ms (1 loading cycle). This recorded FEA displacement was then used to deform images of the experimental setup via MatchID's FE-DEF module, before performing DIC on the output images. The deformations computed by the DIC were then used to characterise the material properties using eqs. (4) and (5) and the virtual field described in eq. (3).

When simulated with no artificial noise, time domain analysis (eq. (4)) overestimated the complex modulus by 5%; however, frequency domain analysis (eq. (5)) estimated the complex modulus with an error of only 0.1%. This showed that the frequency domain analysis was sufficiently accurate for the experiments to go ahead. Section 4 includes an extensive analysis of the effect of camera noise on the accuracy of the measured mechanical properties, as well as a comparison of time domain and frequency domain analysis.

3. Experimental results and analysis

3.1. Low frequency tests on silicone rubber

Two materials were tested in this set of experiments, as previously described: the stiffer polymer was used in order to validate the new apparatus against DMA rheometry data. This stiffer polymer (EcoFlex 10) was used during the commissioning phase in order to avoid some of the difficulties inherent in testing extremely soft materials whilst the device was still being commissioned. Note that EcoFlex 10 is still extremely soft: it is only stiff in comparison to EcoFlex GEL or brain tissue. The deviatoric complex modulus of EcoFlex 10 was characterised on an Anton Paar Physica MCR 301 rheometer at a range of temperatures and frequencies. Specimens were 25 mm in diameter, and 3 mm in thickness, punched from a sheet of material, which was cast as described in section 2.1.

Figure 6 shows low frequency storage and loss modulus measurements for the EcoFlex 10 material at a range of frequencies obtained on the rheometer, as well as the storage and loss moduli measured by the new apparatus for the same material. Both measurement methods give similar results, validating the new apparatus. Note that 20 Hz is near the upper limit of testable frequencies on the rheometer, and near the lower limit of testable frequencies on the new apparatus.

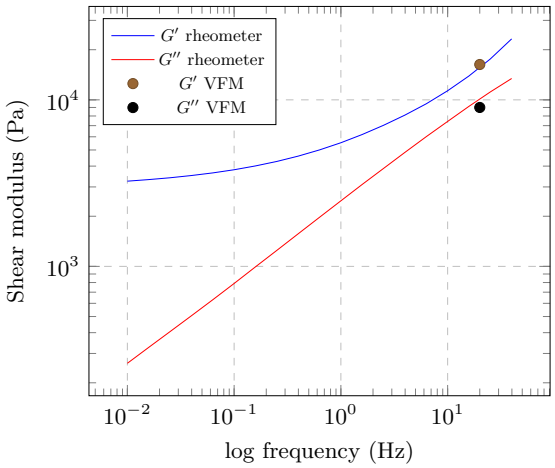


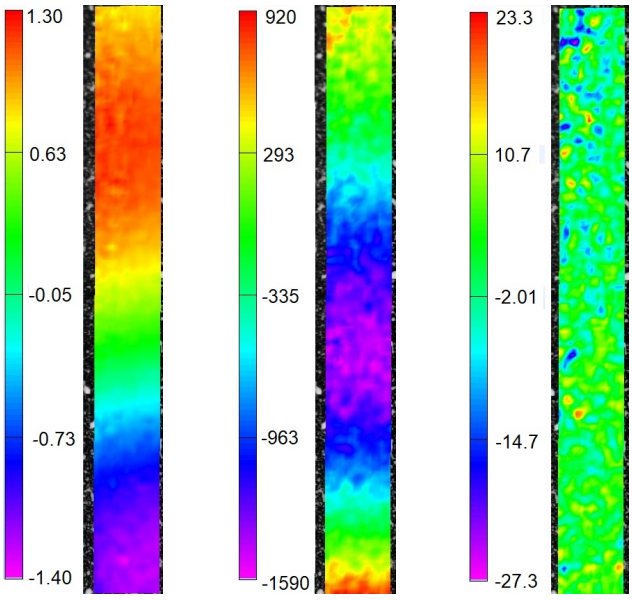
Figure 6: Low frequency storage and loss modulus data from standard rheometry tests on phantom polymer at 25 °C, as well as via VFM on the new apparatus at 20 Hz.

3.2. High frequency VFM

After commissioning and validating the apparatus using EcoFlex 10, experiments using EcoFlex GEL were conducted with confidence. Whilst EcoFlex GEL is still stiffer than brain tissue, it is the softest readily available silicone elastomer.

3.2.1. Worked example

Once the images have been taken and processed using DIC software, the full-field deformation and strain fields are extracted. Note that the strain data calculated by the DIC software are inherently smoothed via the choice of Strain Window (SW) size; this is discussed in Appendix A. If material characterisation calculations are performed in the temporal domain, the full-field acceleration field is also extracted from the DIC software. Figure 7 shows an example of the displacement, velocity, and acceleration fields for a single time-step in an experiment. The time window used for calculation of temporal derivatives in these images is only 3 frames, resulting in noisy temporal derivatives (see Appendix A for further detail). This would be a problem if processing was conducted in the time domain, however all temporal calculations are performed in the frequency domain, effectively filtering the noise from the acceleration field.



(a) Horizontal displacement (b) Horizontal velocity (c) Horizontal acceleration

Figure 7: Horizontal displacement, velocity, and acceleration using a time window of 3 time-steps. Units are pixels, pixels/s, and pixels/ms^2 respectively

Once the full-field deformation data[7] have been extracted from the DIC, further processing is performed. As the Region of Interest (ROI) is approximately 30 datapoints wide, spatial averaging of horizontal datapoints is possible; this significantly reduces noise, and is done for all data extracted from the DIC process. Care is taken to keep the ROI narrowly centred around the centre of the cylinder, in order to avoid errors due to surfaces that are not perpendicular to the camera. An example of this is shown in fig. 8, where the grey dots are the raw (noisy, 2D) data-field extracted directly from the DIC, and the red line is the 1D averaged value.

If material characterisation calculations are being performed in the temporal domain, no further data processing is required before calculation of eq. (4). If material characterisation calculations are to be done in the frequency domain (as was the case for the set of experiments shown in this paper), the displacement and strain data are passed through a temporal FFT in order to obtain the spatially varying frequency components of displacement and strain:

$$\boldsymbol{u}(\boldsymbol{X},t) \overset{\text{FFT}}{\Rightarrow} \tilde{\boldsymbol{u}}(\boldsymbol{X},f) \tag{6}$$

$$\boldsymbol{\epsilon}(\boldsymbol{X},t) \overset{\text{FFT}}{\Rightarrow} \tilde{\boldsymbol{\epsilon}}(\boldsymbol{X},f) \tag{7}$$

The frequency components of acceleration are obtained directly from the frequency components of displacement[8] us-

[7] displacement, strain, acceleration

[8] rather than via a finite difference calculation, as in the temporal domain calculations

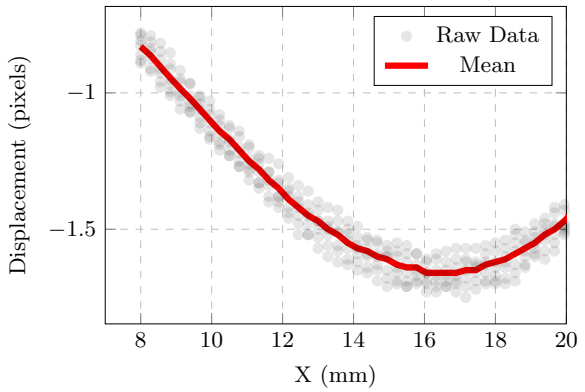


Figure 8: Horizontal displacement vs co-ordinate. Full field (2D) datapoints are shown in grey, with 1D (horizontally averaged) values shown in red. Note how the horizontal spatial averaging greatly decreases the effect of noise, as multiple samples are taken for each X position. See fig. 1 for indication of the meaning of the X axis values.

ing:

$$\tilde{\ddot{\boldsymbol{u}}}(\boldsymbol{X}, f) = -(2\pi f)^2 \tilde{\boldsymbol{u}}(\boldsymbol{X}, f) \tag{8}$$

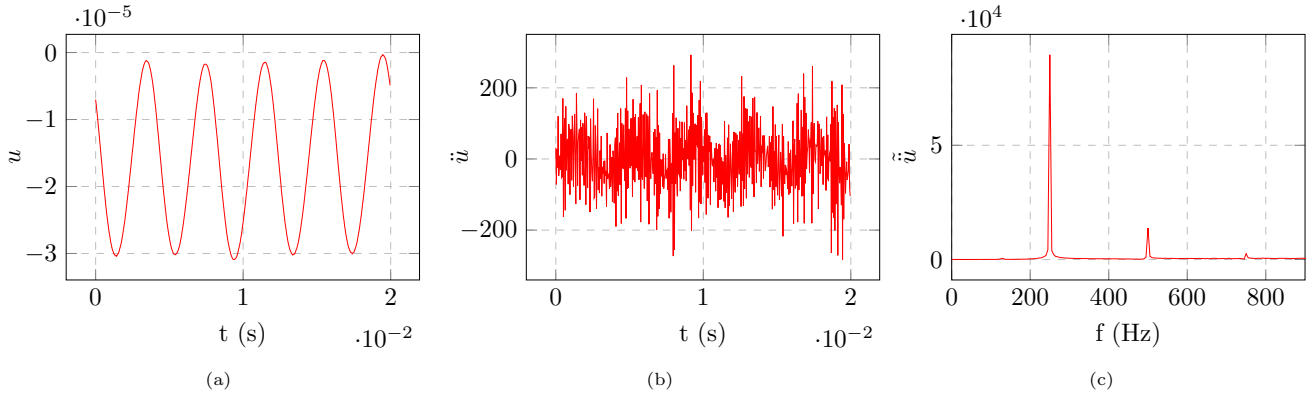
Figure 9 shows an example of the displacement in the time domain, and the acceleration in both the time and frequency domains for a single point. The time domain displacement is relatively smooth, and appears to have minimal noise. The time domain acceleration is very noisy, however, as the double derivative has the effect of amplifying noise. In spite of this, the signal is isolated to only a small number of frequencies; therefore, in the frequency domain (fig. 9c), it is straightforward to isolate the signal from the noise. Note the presence of harmonics at double and triple the primary frequency, allowing for the extraction of moduli at three frequencies from a single experiment (fourth and higher harmonics exist, but have a low magnitude approaching the noise floor, preventing the extraction of useful information). The presence of these harmonics was not expected (as the loading was nominally a pure sine wave), however they are useful.

Spatially varying complex moduli are now calculated using the frequency domain acceleration and strain data and eqs. (3) and (5). Unlike typical test methods, the extracted complex moduli do not assume a homogeneous material, allowing for spatially varying results. The material properties are calculated for each datapoint by integrating over a narrow virtual field of interest centred about that point. For a point at position X_i, the virtual field is described by eq. (3), with the limits X_0 and X_1 given by:

$$X_0, X_1 = X_i \pm w \tag{9}$$

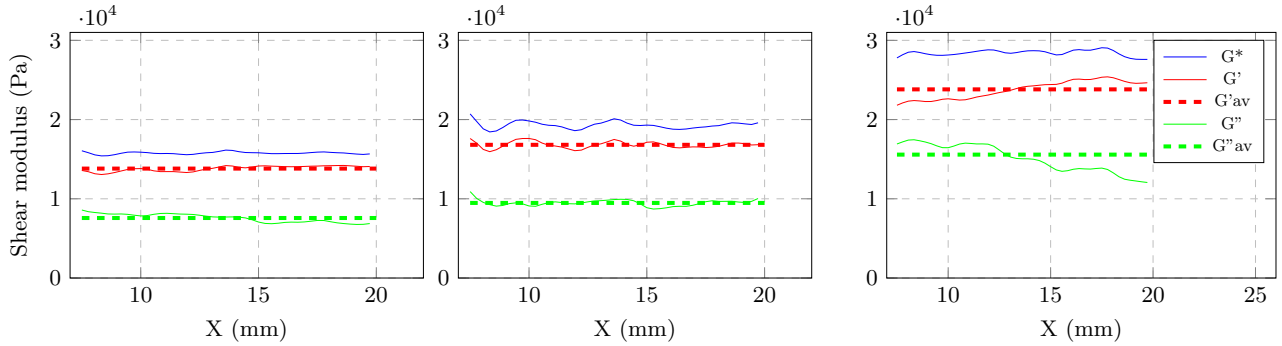
This method effectively provides a moving average of the material properties, where increasing the domain half-width (w) increases the degree of smoothing, reducing noise at the expense of spatial resolution. For the experiments described in this paper, a domain half-width of 100 pixels was selected.

Figure 10, shows examples of the spatially varying complex modulus extracted from this experiment at the nominal loading frequency of 250 Hz and the two harmonics at 500 and 750 Hz. Whilst the material tested in this set of experiments is fairly homogeneous (obviating the need for spatially varying analysis), this methodology is designed to eventually be used on soft biological tissue such as brain tissue (which is heterogeneous on both a cellular and a tissue level scale).



(a) (b) (c)

Figure 9: (a) displacement (m) vs time, (b) acceleration (m/s^2) vs time, and (c) acceleration (m/s^2) vs frequency for a single spatial location. Time and frequency axes are both truncated, in order to show graphs with a meaningful aspect ratio. In fact, data were obtained for 200 ms, equivalent in this case to 50 cycles. Note that the Fourier transform of the acceleration was not normalised, hence the large values.



(a) (b) (c)

Figure 10: Spatial distribution of storage, loss, and complex moduli at (a) 250, (b) 500, and (c) 750 Hz.

3.2.2. Results

As the material tested in this set of experiments is fairly homogeneous (as shown in figs. 10 and 12), the mean complex modulus for a series of further experiments performed at different frequencies is plotted in fig. 11. While this apparatus was designed to operate above 100 Hz, some experiments were conducted at frequencies as low as 10 Hz in order to probe the lower limits of the apparatus's operating envelope[9]. Note that fig. 11 includes repeated tests at 20 Hz and 200 Hz; the experiments at 20 Hz (8.5 kPa and 9.4 kPa) have less overlap than the experiments at 200 Hz (14.7 kPa and 15.1 kPa), implying that the experiments at 200 Hz are more reliable/repeatable. This is not surprising, as the acceleration field is much lower for low frequency experiments, resulting in weaker signals and a greater sensitivity to noise. If this apparatus is to be used at frequencies below 30 Hz, it is recommended that the surface traction forces are recorded and taken into account during the VFM calculation, in order to increase the magnitude of the signal. This would be done by modifying the selected virtual field to be non-zero on the boundaries, making the traction term in eq. (2) non-zero. For further detail on how this may work, the reader is referred to [14, 23, 24].

[9]Note too that the FFT has a frequency resolution of 5Hz per bin – if low frequency tests are to be conducted, the framerate of the camera should be reduced and the recording time increased, in order to obtain a more appropriate frequency resolution.

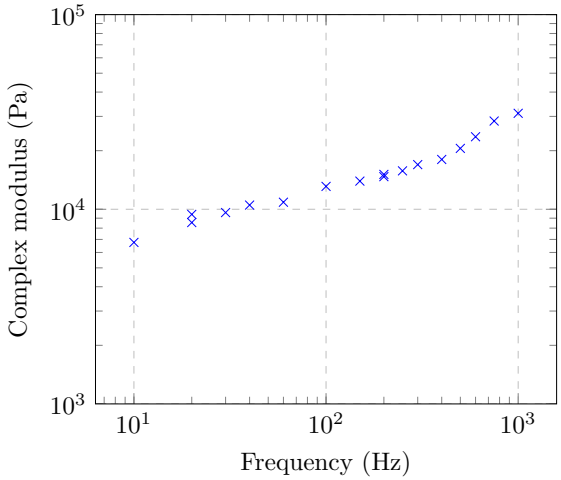


Figure 11: Spatially averaged frequency dependent complex moduli extracted from experiments.

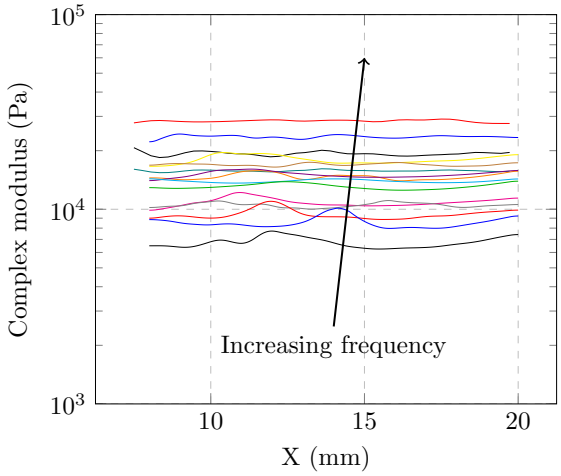


Figure 12: Spatial distribution of complex moduli for a range of frequencies.

4. Effect of camera noise on measured mechanical properties

Section 2.4 showed through simulations that the new apparatus could give correct results, but did not cover the effect of noise on the accuracy of the measured mechanical properties. All cameras have some noise, however, and this affects the accuracy of the DIC measurements. Therefore, simulations were conducted in which artificial grey-scale noise ranging from 0 to 8% was added to the deformed images. This allows for a quantification of the effects of camera noise on the measured mechanical properties. Unlike the set of experiments conducted in this paper, the specimens simulated in this section were set up with a free end. This allowed for calculation of the stress via direct integration, as the stress at the free end is known to be zero. This was done in order to minimise the effect of choice of virtual field on the outcome of the numerical analysis, and to allow for a direct visualisation of the calculated stress field; whilst the full VFM calculates the material properties, it does not directly output the stress field. In order to achieve this, the dynamic equilibrium equation is integrated from the free end, $X = 0$:

$$\boldsymbol{\sigma}(X) = \int_0^X \rho \boldsymbol{a} dX \tag{10}$$

Where the acceleration is either calculated using a finite difference scheme with a window width of 3 time-steps, or from the FFT as indicated in eq. (8). This calculated stress field can now be directly compared to the strain field measured by the DIC. Direct integration was not used for the experiments as it would prevent the application of pre-strains or require that the traction at the ends was measured; this would reduce the flexibility and robustness of the experimental methodology.

Figure 13 shows the measured horizontal displacement field for various levels of artificial camera noise ranging from noiseless on the left to 8% noise on the right; note that the increment of noise between images are not constant. Whilst this image displays the effects of increasing pixel noise, a similar effect will occur as the result of decreasing speckle pattern quality. It is not expected that camera pixel noise levels will ever reach 8% (the images taken for the experiments in this paper had a noise level of approximately 0.45% for instance); however, poor speckle quality or lighting could nevertheless result in DIC with significant errors. Whilst the displacement field itself is relatively smooth up until camera noise levels of 1-2%, the process of spatial or temporal differentiation amplifies the noise in the strain and acceleration fields respectively. Further detail around optimisation of DIC processing parameters for spatial and temporal differentiation is given in Appendix A.

Figure 14 shows an example of the calculated stress and strain distribution at a single time-step for varying levels of camera noise. When using a Finite Difference (FD) scheme to calculate temporal derivatives (and hence the stress distribution, via eq. (10)) as shown in fig. 14a, it is clear that camera noise levels of 4% and above are too high to allow for meaningful material characterisation. In contrast, when using a Fourier Transform (FT) to calculate accelerations (and hence stress distributions) as shown in fig. 14b, camera noise has significantly lower effects on the quality of the calculated stress distribution.

When calculating complex moduli from time domain data, not only is the calculation highly sensitive to noise (as shown in fig. 15), it is also not simple to calculate the storage and loss moduli; only the magnitude of the complex modulus is easily obtained.

Figure 16 shows the frequency dependant shear moduli calculated from the frequency domain data. Note that the calculation is remarkably resistant to the effects of camera noise – as the noise is effectively random for each frame,

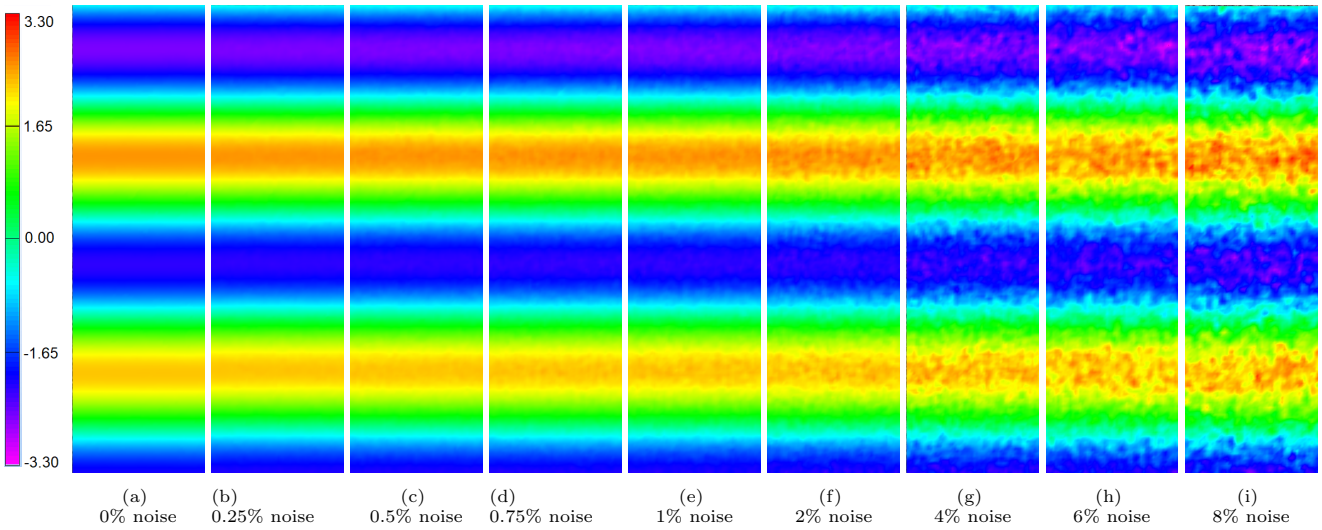
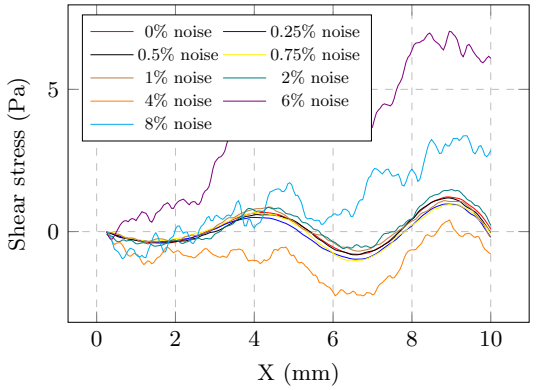


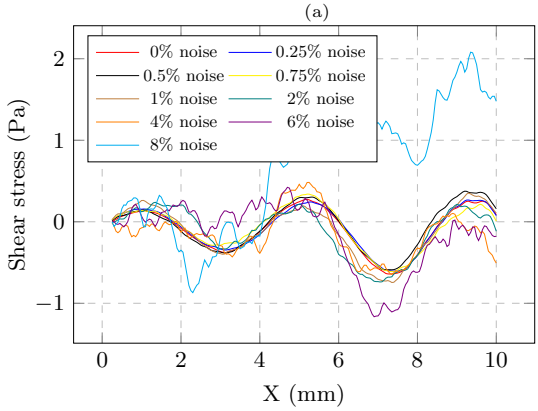
Figure 13: Calculated horizontal displacement field for various levels of artificial image noise. Scale is in pixels. All images were produced from the same underlying deformation field.

the FFT easily removes the noise while leaving the signal of interest. Whilst fig. 14b is a significant improvement over the stress field calculated by a Finite Difference Scheme, it still contains spurious high frequency components. In contrast, fig. 16 utilises only the frequency of interest, and as a result is unaffected by any noise components at other frequencies. Additionally, the phase angle of the complex modulus is easily calculated when using the frequency domain method, unlike the time domain method.

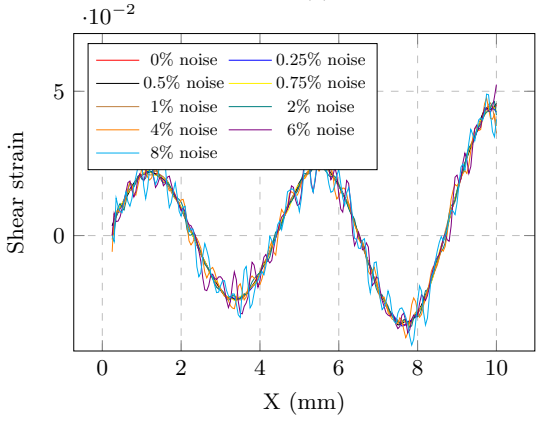
These simulations showed that the new apparatus and analysis method are robust, particularly when calculations are conducted in the frequency domain. Furthermore, analysis shows that analysing the data in the frequency domain (rather than the time domain, as is common in the literature) gives significantly more accurate results, even when high levels of noise are added to the data. Traditional time domain methods optimise the virtual field to minimise the effect of noise (something that was not done here), however there is a limit to how much said method can minimise the effects of noise, and it is less robust than the frequency domain method outlined here.



(a)



(b)



(c)

Figure 14: Stress calculated via a finite difference scheme (a), stress calculated via a Fourier transfer (b), and strain (c) vs spatial position for varying levels of camera noise. All images refer to data at 0.6 ms.

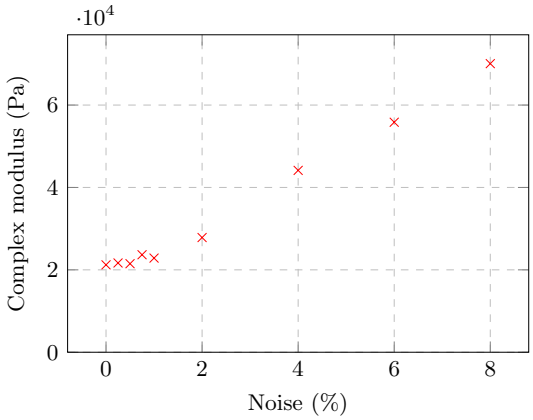


Figure 15: Measured frequency dependant complex vs image noise level using time domain analysis. Note the significant overestimation of the modulus even for noise levels as low as 2%.

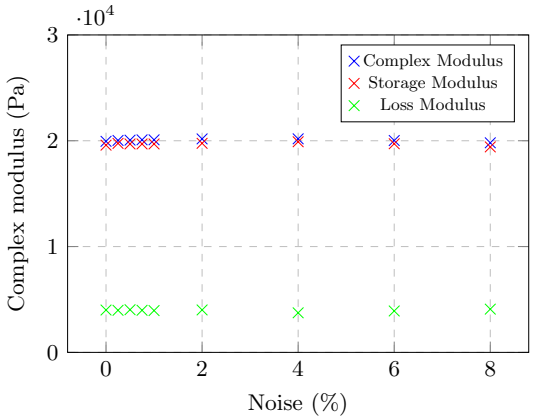


Figure 16: Measured frequency dependant moduli vs image noise level. Note that the FFT based analysis allows tests with noise levels of 8% to give useful results, in contrast with fig. 15

5. Discussion

5.1. Frequency domain analysis

Unlike most previous experiments in the literature, this set of experimental data contains multiple oscillations of each frequency, allowing for the use of a Fourier transform without being significantly affected by the Gabor limit. As a result, the measured frequency data is sharply band limited, in contrast to data obtained from traditional test methodologies. This method of analysis has a significant advantage, particularly when the data is noisy. During simulated experiments, the time domain approach started to give erroneous results once the camera noise level approached 2% and above, whereas the frequency domain approach was capable of giving accurate results even when the camera noise level was 8%. This will be particularly advantageous if it allows for the use of cameras which exploit on-chip storage to allow speeds of a few millions of frames per second. Such cameras have high resolutions at very high frame rates, but can have substantially higher levels of noise [25].

5.2. Spatially varying mechanical characterisation

Whilst this apparatus and analysis method allow for heterogeneity in the tested materials, this property was not fully exploited for these tests as the material was close to homogeneous. This property is still valuable however, as this apparatus will be used on soft biological tissue in the future. Ongoing tests are being conducted on soft polymers deliberately manufactured to have spatially varying properties, in order to quantify the ability of this methodology to accurately characterise visco-elastic heterogeneous materials.

5.3. Range of testable frequencies, sample stiffnesses

This apparatus is capable of characterising soft materials at frequencies from 20-1000 Hz, a significant improvement over standard test methods such as a rheometer. The upper limit on testable frequencies is limited by the obtainable frame-rate, as well as the travel of the apparatus; as the frequency increases, the displacement amplitude decreases significantly, requiring greater spatial resolution. Future tests at higher frequencies are planned, using the lighter torsional pendulum, with a higher resonant frequency, and a lens with a higher zoom ratio in order to mitigate the problems caused by the small displacement amplitudes at high frequencies. Fundamentally, however, the amplitude is limited by the displacement capability of the shakers. Whilst the material tested in these experiments is insensitive to temperature, future tests on a temperature sensitive material would allow for experimental validation of the high frequency high temperature material response predicted by TTS shifting of low temperature low frequency data.

This apparatus was designed for very soft materials such as brain tissue, and it has performed as required. It has not been tested on stiffer materials however; future tests and simulations should be conducted in order to evaluate the range of sample stiffnesses over which the apparatus can operate. It is likely that the range of testable frequencies will be strongly influenced by the stiffness of the material, with lower modulus materials allowing for lower frequency tests.

For a qualitative guide to testable frequencies with various high speed cameras the reader is referred to Appendix C. This appendix briefly investigates the trade-offs between displacement magnitude, displacement resolution, driving frequency, and material properties.

5.4. Hyper-elastic frequency dependant characterisation

Whilst this set of experiments did not probe the frequency response of the material at a variety of static (DC) strain states, the apparatus is capable of doing so. Future experiments aim to obtain the hyper-elastic behaviour of the material at a range of strains and frequencies, data that is particularly valuable for soft biological tissue (which exhibits strongly non-linear elastic behaviour). This proposed experimental procedure is shown in fig. 17. For further reading on hyper-viscoelastic material characterisation via the VFM, the reader is referred to [5].

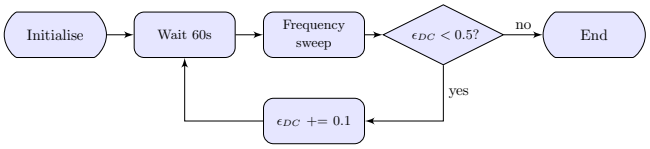


Figure 17: Flowchart showing proposed experimental procedure for hyper-viscoelastic material characterisation.

5.5. Comparison with similar methods in the literature

The most similar existing method in the literature is the ultrasonic horn method developed by Seghir and Pierron (2018) [26], which utilises a combination of high speed DIC, high power ultrasonic loading, and infrared thermography in order to characterise the visco-elastic behaviour of a polymer specimen including thermal effects in oscillatory tension/compression. One of the primary differences between Seghir's methodology and the new apparatus is that Seghir's methodology requires the existence of a standing wave in the specimen (and operates best if the specimen resonates). This limits the testable frequencies depending on the specimen properties and geometry. The current methodology is capable of testing significantly softer materials over a wider range of frequencies, but would not be suitable for very stiff polymers, which can be tested using Seghir's method. Additionally, Seghir's method characterises the material under longitudinal loading, whilst this method characterises the material under pure deviatoric loading – something that is important for near incompressible materials, as discussed earlier in this paper.

6. Conclusions

This novel apparatus is capable of accurately measuring the full-field mechanical properties of low modulus materials at high frequencies via the VFM. Unlike traditional test methods such as DMA rheometry, the methodology makes no assumption of material homogeneity, and is able to characterise heterogeneous materials. This will be particularly valuable for testing soft biological materials (such as brain tissue) which exhibit strong frequency dependence, but are heterogeneous and ultra-soft. Furthermore, this apparatus is capable of directly characterising low modulus materials at frequencies which are normally only predicted via TTS; as a result, this methodology could be used to either validate TTS data, to further extend the range of frequencies predicted by TTS, or on materials such as biological tissue for which TTS is not appropriate. Overall, this apparatus and analysis method has been shown capable of obtaining important material characterisation data that would be impossible to access using currently existing test techniques.

7. Acknowledgements

Aaron Graham thanks the Rhodes Trust for funding his DPhil Studies. The authors would also like to thank the Solid Mechanics Technicians, Richard Duffin, Neil Warland and Andy Batemen for constructing the experimental apparatus that was used in this project. The authors thank Antoine Jérusalem for very useful discussion during the course of the research, and Nick Hawkins for assistance with the rheology.

This material is based upon work supported by the Air Force Office of Scientific Research, Air Force Material Command, USAF under Award No. FA9550-15-1-0448.

References

[1] W. W. Chen, Experimental Methods for Characterizing Dynamic Response of Soft Materials, Journal of Dynamic Behavior of Materials 2 (2016) 2–14.

[2] S. Budday, T. C. Ovaert, G. A. Holzapfel, P. Steinmann, E. Kuhl, Fifty Shades of Brain: A Review on the Mechanical Testing and Modeling of Brain Tissue, Archives of Computational Methods in Engineering (2019) 1–44.

[3] G. Z. Voyiadjis, A. Samadi-Dooki, Hyperelastic modeling of the human brain tissue: Effects of no-slip boundary condition and compressibility on the uniaxial deformation, Journal of the Mechanical Behavior of Biomedical Materials (2018).

[4] S. Budday, G. Sommer, J. Haybaeck, P. Steinmann, G. A. Holzapfel, E. Kuhl, Rheological characterization of human brain tissue, Acta Biomaterialia (2017).

[5] S.-h. Yoon, I. Giannakopoulos, C. R. Siviour, Application of the Virtual Fields Method to the uniaxial behavior of rubbers at medium strain rates, International Journal of Solids and Structures 69-70 (2015) 553–568.

[6] J. Field, S. Walley, W. Proud, H. Goldrein, C. Siviour, Review of experimental techniques for high rate deformation and shock studies, International Journal of Impact Engineering 30 (2004) 725–775.

[7] M. L. Williams, R. F. Landel, J. D. Ferry, The Temperature Dependence of Relaxation Mechanisms in Amorphous Polymers and Other Glass-forming Liquids, Journal of the American Chemical Society 77 (1955) 3701–3707.

[8] C. R. Siviour, J. L. Jordan, High Strain Rate Mechanics of Polymers: A Review, Journal of Dynamic Behavior of Materials 2 (2016) 15–32.

[9] H. Chen, A. R. Trivedi, C. R. Siviour, Application of Linear Viscoelastic Continuum Damage Theory to the Low and High Strain Rate Response of Thermoplastic Polyurethane, Experimental Mechanics 60 (2020) 925–936.

[10] A. R. Trivedi, C. R. Siviour, A Simple Rate–Temperature Dependent Hyperelastic Model Applied to Neoprene Rubber, Journal of Dynamic Behavior of Materials 6 (2020) 336–347.

[11] A. Garo, M. Hrapko, J. A. W. van Dommelen, G. W. M. Peters, Towards a reliable characterisation of the mechanical behaviour of brain tissue: The effects of post-mortem time and sample preparation., Biorheology 44 (2007) 51–8.

[12] J. Zhang, N. Yoganandan, F. A. Pintar, Y. Guan, B. Shender, G. Paskoff, P. Laud, Effects of tissue preservation temperature on high strain-rate material properties of brain, Journal of Biomechanics 44 (2011) 391–396.

[13] R. Moulart, F. Pierron, S. R. Hallett, M. R. Wisnom, Full-Field Strain Measurement and Identification of Composites Moduli at High Strain Rate with the Virtual Fields Method, Experimental Mechanics 51 (2011) 509–536.

[14] F. Pierron, M. Grédiac, The Virtual Fields Method, Springer New York, New York, NY, 2012. URL: http://link.springer.com/10.1007/978-1-4614-1824-5. doi:10.1007/978-1-4614-1824-5.

[15] T. K. Tonge, L. S. Atlan, L. M. Voo, T. D. Nguyen, Full-field bulge test for planar anisotropic tissues: Part I-Experimental methods applied to human skin tissue, Acta Biomaterialia (2013).

[16] M. Grédiac, E. Toussaint, F. Pierron, Special virtual fields for the direct determination of material parameters with the virtual fields method. 1—Principle and definition, International Journal of Solids and Structures 39 (2002) 2691–2705.

[17] S. Avril, M. Bonnet, A.-S. Bretelle, M. Grédiac, F. Hild, P. Ienny, F. Latourte, D. Lemosse, S. Pagano, E. Pagnacco, F. Pierron, Overview of Identification Methods of Mechanical Parameters Based on Full-field Measurements, Experimental Mechanics 48 (2008) 381–402.

[18] F. Pierron, H. Zhu, C. Siviour, Beyond Hopkinson ' s bar Beyond Hopkinson ' s bar, Philosophical Transactions of the Royal Society A 372 (2014) 20130195.

[19] S.-h. Yoon, M. Winters, C. R. Siviour, High Strain-Rate Tensile Characterization of EPDM Rubber Using Non-equilibrium Loading and the Virtual Fields Method, Experimental Mechanics 56 (2016) 25–35.

[20] W. S. LePage, S. H. Daly, J. A. Shaw, Cross Polarization for Improved Digital Image Correlation, Experimental Mechanics 56 (2016) 969–985.

[21] S.-O. lnc, Ecoflex ™ GEL, Technical Report, 2018. URL: https://www.smooth-on.com/tb/files/ECOFLEX{_}GEL{_}TB.pdf.

[22] S.-O. lnc, Ecolfex Series technical bulletin, Technical Report, 2018. URL: https://www.smooth-on.com/tb/files/ECOFLEX{_}SERIES{_}TB.pdf.

[23] S. H. Yoon, C. R. Siviour, Application of the Virtual Fields Method to Rubbers Under Medium Strain Rate Deformation Using Both Acceleration and Traction Force Data, Journal of Dynamic Behavior of Materials 3 (2017) 12–22.

[24] S. ho Yoon, C. R. Siviour, Application of the Virtual Fields Method to a relaxation behaviour of rubbers, Journal of the Mechanics and Physics of Solids 116 (2018) 416–431.

[25] F. Pierron, R. Cheriguene, P. Forquin, R. Moulart, M. Rossi, M. Sutton, Performances and Limitations of Three Ultra High-Speed Imaging Cameras for Full-Field Deformation Measurements, Applied Mechanics and Materials 70 (2011) 81–86.

[26] R. Seghir, F. Pierron, A Novel Image-based Ultrasonic Test to Map Material Mechanical Properties at High Strain-rates, Experimental Mechanics 58 (2018) 183–206.

Appendix A. DIC settings optimisation

Spatial discretisation

In order to select the optimal DIC settings, a performance analysis was conducted on a set of artificially deformed images. A reference image taken from one of the experiments was deformed with a series of known sine waves, and DIC analysis was then conducted on the resulting images. The measured deformation was then compared to the input deformation, allowing for the quantification of the displacement and strain resolution of the DIC. This allowed for the selection of optimal processing parameters, as well as a quantification of range of conditions under which the DIC measurements are valid. Figure A.20 shows the full-field deformation generated by conducting DIC on these artificially deformed images in order to give the reader a qualitative appreciation of the fields used, whilst figs. A.18 and A.19 give a quantitative measure of the performance of the DIC process. For a detailed description of what the Strain Window (SW) size is and how it affects the virtual strain gauge, the reader is directed to `http://www.matchid.eu/Documentation/doku.php?id=matchid:training:lessons:dic`

Given that the images were deformed with a sine wave of known amplitude and period, the correct (analytical) displacement and strain field is known for each artificially deformed image. The displacement and strain field measured by the DIC analysis is then compared to the analytical solution, and the measurement error is calculated by:

$$E_{\text{displacement}} = \frac{u_{\text{measured}} - u_{\text{analytical}}}{u_{\text{analytical}}} \tag{A.1}$$

$$E_{\text{strain}} = \frac{\epsilon_{\text{measured}} - \epsilon_{\text{analytical}}}{\epsilon_{\text{analytical}}} \tag{A.2}$$

A positive error means that the quantity of interest has been over-estimated, and a negative error means that the quantity of interest has been under-estimated. Particularly for high frequency deformation, negative error occurs as a result of the deformation being smoothed by the overly large facets: the period of each sine wave is only 25.6 pixels for the final data-point in fig. A.19 for instance, resulting in a large underestimation of the displacement when facets of width 25 are used to measure the displacement.

Temporal discretisation

In order to calculate the acceleration for each data-point at each time-step, a finite difference scheme was used to fit a polynomial to a moving window about the time-step. Figure A.21 shows an example of the horizontal displacement, velocity, and acceleration for a given time-step, taken from an experiment conducted with a loading frequency of 250 Hz and an imaging frequency of 25 000 fps. Note the low amount of noise in fig. A.21a, which is amplified by the finite difference scheme in fig. A.21b and further amplified in fig. A.21c. This amplified noise can be reduced by increasing the number of datapoints used to calculate the temporal derivatives, reducing the impact of noise at each individual datapoint.

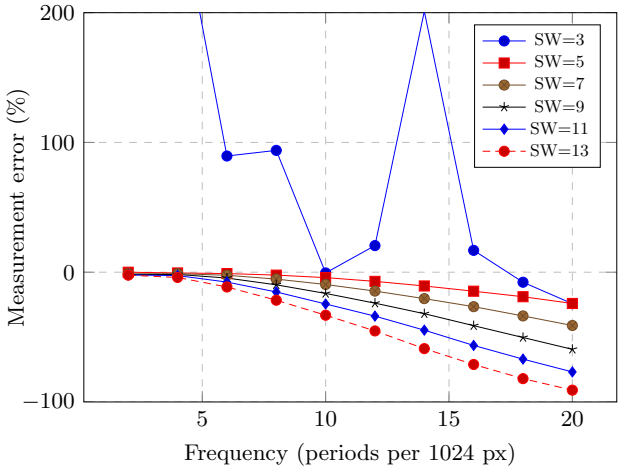


Figure A.18: Strain magnitude measurement error vs deformation frequency for various SW sizes. Y axis is artificially truncated, as the first 2 data-points for a SW of 3 are 850% and 290%. Note that a SW of 5 is superior in almost all cases – the SW of 3 outperforms for frequencies of 10,16, and 20, but is highly inaccurate in other cases. The SW of 5 has an error of less than 5% up to a frequency of 10, but error rapidly increases after this, reaching 24% underestimation for a frequency of 20

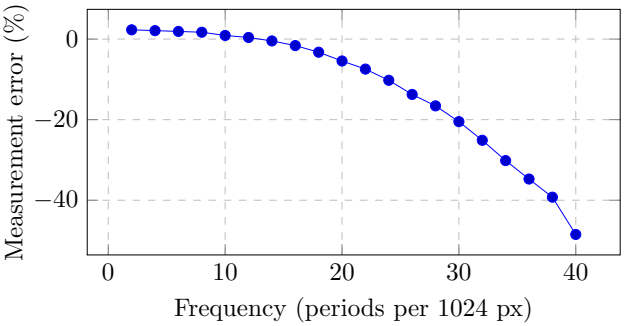


Figure A.19: Deformation magnitude measurement error vs deformation frequency

Figure A.22 shows the acceleration field for the same frame, using a range of smoothing window durations. Note that fig. A.22a is dominated by noise, as the finite difference scheme exaggerates the noise inherent to the DIC measurement. Figure A.22e has minimal noise, however a smoothing window of duration 23 inevitably removes a significant portion of the signal in addition to the noise. A window of duration 5 was used, as the spatial integration of the acceleration field smoothed a significant portion of the noise amplified by the temporal discretisation. Additionally, the noise is Gaussian, making it trivial to remove via an FFT during post-processing.

$u(x) = sin(2x\frac{2\pi}{1024})$

$u(x) = sin(4x\frac{2\pi}{1024})$

$u(x) = sin(8x\frac{2\pi}{1024})$

$u(x) = sin(12x\frac{2\pi}{1024})$

$u(x) = sin(20x\frac{2\pi}{1024})$

$u(x) = sin(30x\frac{2\pi}{1024})$

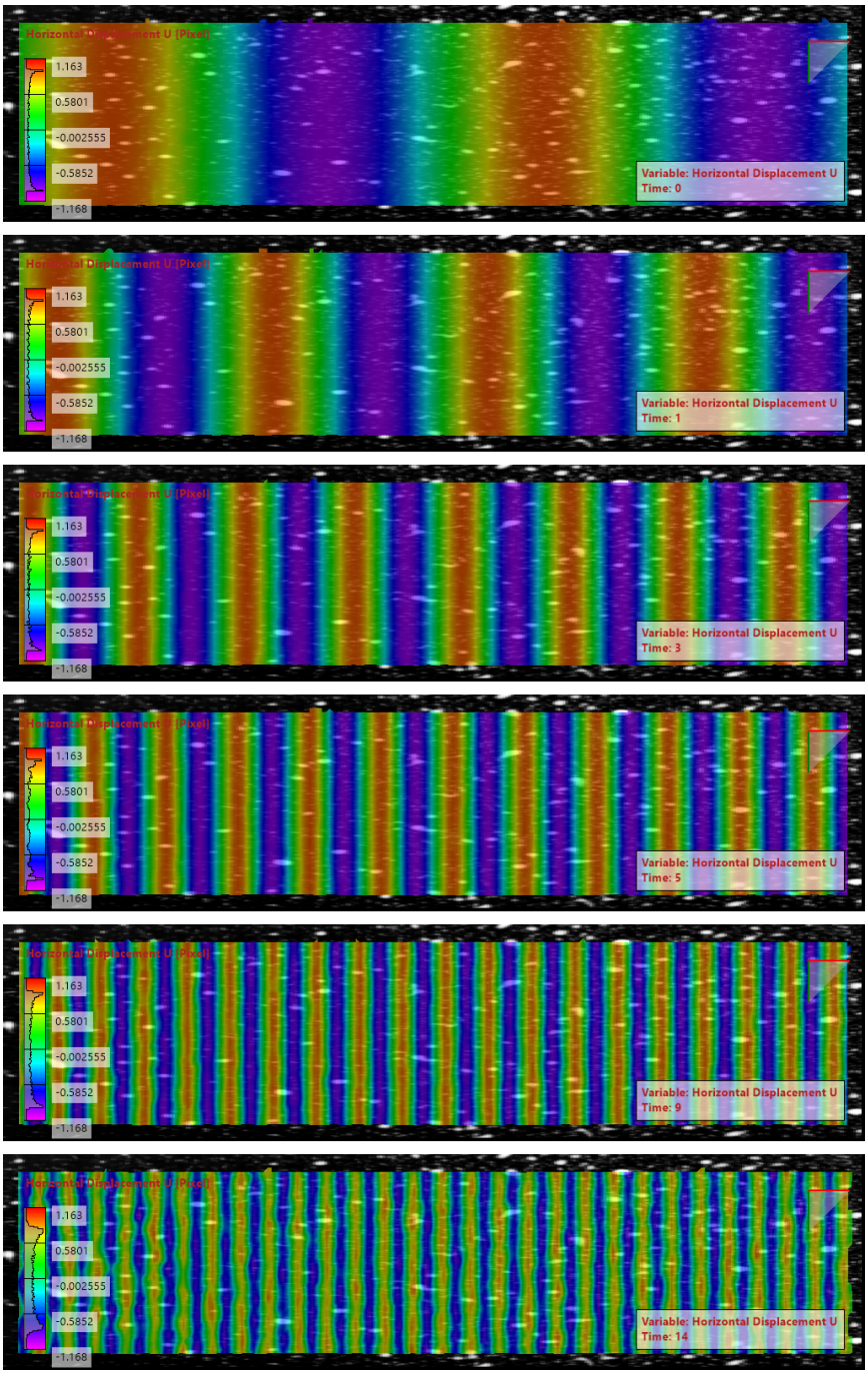
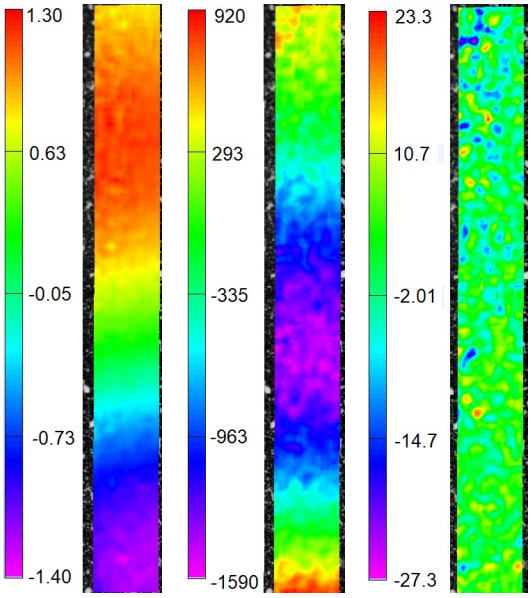


Figure A.20: Deformation fields obtained from DIC analysis of images with applied deformation fields. Here, $u(x)$ represents the vertical displacement field applied to the image in pixels, where x represents the horizontal position along the image, which itself was 1024 pixels long and 256 pixels high. The top image has a spatial frequency of 512 pixels, and the data exhibit almost no artificial smoothing or noise. IN contrast, the bottom image has a spatial frequency of only 24.1 pixels, resulting in significant noise and underestimation of the deformation magnitude. Note however that the subset size used was 25x25 pixels; it is surprising that the bottom image was not even less accurate. A quantitative measure of the underestimation in this image is shown in fig. A.19 and fig. A.18

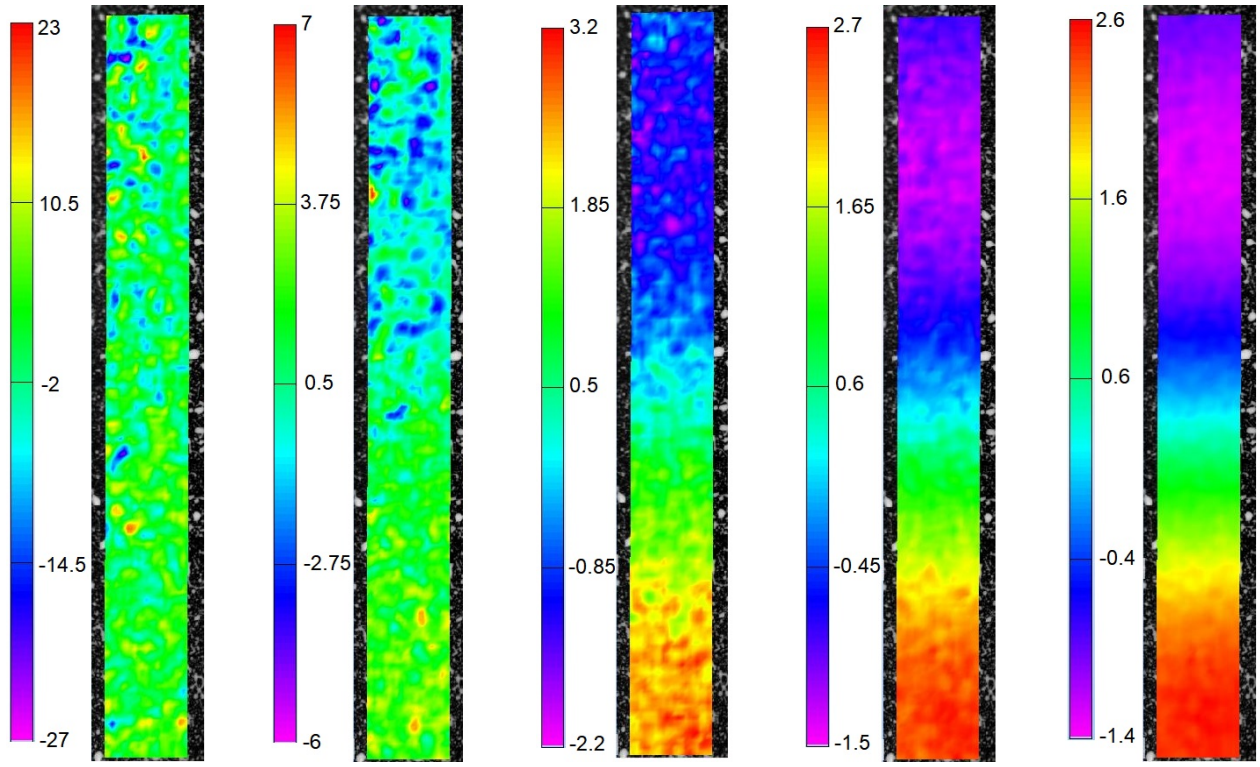


(a) Horizontal displacement

(b) Horizontal velocity, window 3

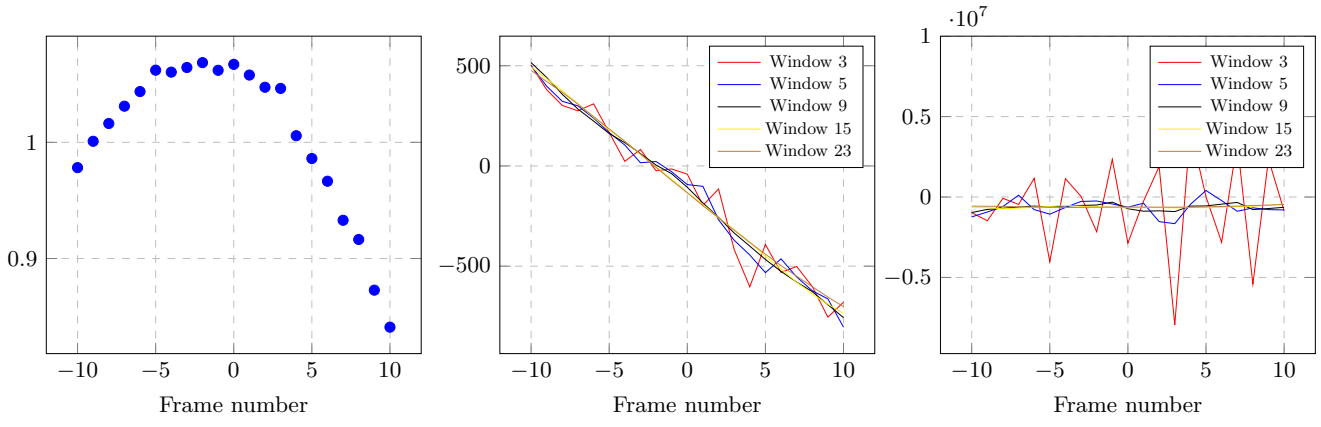
(c) Horizontal acceleration, window 3

Figure A.21: Horizontal displacement, velocity, and acceleration using a time window of 3 time-steps. Units are pixels, pixels/s, and pixels/ms^2 respectively



(a) Window 3 (b) Window 5 (c) Window 9 (d) Window 15 (e) Window 23

Figure A.22: Horizontal acceleration field at a single timestep, using a smoothing window of 3, 5, 9, 15, and 23 time-steps respectively. Acceleration in units of pixel/ms^2



(a) (b) (c)

Figure A.23: Displacement (a), velocity (b) , and acceleration (c) vs frame no (time) for a single spatial point. Y axis units are pixels, pixels/s, and pixels/s^2 respectively. Velocity and acceleration are shown for various temporal smoothing windows. Frame 0 is the frame shown in fig. A.22 and fig. A.21

Appendix B. VFM worked example further calculations

The displacement field at time t will be given by the following equation, valid when 2 ms $< t <$ 5 ms:

$$u_Y(X,t) = \begin{cases} 0 & \text{if } X < 2t - 4 \\ A(\cos(500\pi(2t - X)) - 1) & \text{if } 2t - 4 < X < 2t \\ 0 & \text{if } X > 2t \end{cases} \tag{B.1}$$

The acceleration and strain in the dynamic section will be given by:

$$\ddot{u}_Y(X,t) = -10^6\pi^2 A\cos(500\pi(2t - X)) \tag{B.2}$$

$$\frac{\partial u_Y(X,t)}{\partial X} = -500\pi A\sin(500\pi(2t - X)) \tag{B.3}$$

Plots of the acceleration, velocity, displacement, strain, strain gradient term, and inertial term for time $t = 3.5$ ms are shown in fig. B.24.

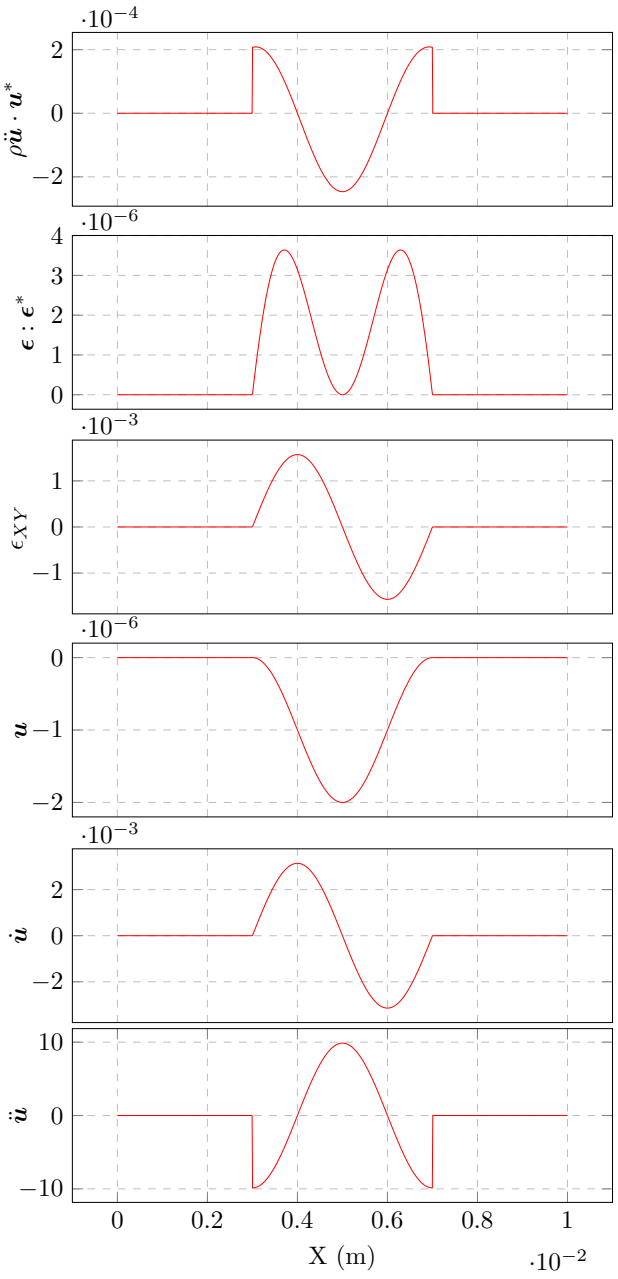


Figure B.24: Acceleration, velocity, displacement, strain, strain gradient term, and inertial term for time $t = 3.5$ ms

Appendix C. Testable frequencies vs camera/experimental settings

Consider a linear-elastic[10] specimen with a density of 1000 kg/m^3, an elastic shear modulus of 100 kPa, and a shear wave-speed c_s of 10 m/s. If the region of interest is fixed at 10 mm in length, and the specimen is to be tested at a variety of frequencies, there is clearly a limit to the possible frequencies at which tests can be conducted. If the base of the specimen is oscillated at a frequency of f Hz and an amplitude of A m, the displacement field in the specimen will take the following form:

$$u_Y(X,t) = A\sin\left(2\pi\left(ft - \frac{fX}{c_s}\right)\right) \qquad \text{(C.1)}$$

and the shear strain field will take the following form:

$$\epsilon_{XY} = \frac{\partial u_Y}{\partial X} = \frac{2\pi f A}{c_s}\cos\left(2\pi\left(ft - \frac{fX}{c_s}\right)\right) \qquad \text{(C.2)}$$

Displacement amplitude vs frequency

here, the magnitude of the strain field is clearly proportional to the driving frequency, given a fixed displacement amplitude (A) and shear wave-speed, c_s. DMA and other linear visco-elastic test methodologies rely on the specimen strain being small however, so a sensible test regime would vary the displacement amplitude with frequency so as to keep the strain magnitude constant. If the sample described in this section is to be tested at a shear strain magnitude of 1%, the surface displacement amplitude will be inversely proportional to the driving frequency:

$$A(f) = \frac{1}{20\pi f}\text{ m} \quad \approx \quad \frac{100}{2\pi f}\text{ mm} \qquad \text{(C.3)}$$

Spatial resolution vs frequency

Assuming that the setup is the same as in this set of experiments, the displacement resolution will be approximately 0.0084 pixels; if the region of interest is 10 mm high and the sensor resolution is 1024 pixels, this translates to a displacement resolution of approximately $\frac{0.0084\times 0.01}{1024} = 0.082$ μm. One should be aware that the strain resolution will generally be lower than the displacement resolution, and that both strain and displacement resolution decrease as the magnitude of the strain gradients increases; this is discussed in Appendix A. As a result, the resolution estimate of 0.082 μm will be an underestimate at higher spatial deformation frequencies; this effect is not taken into account here, as this discussion aims to produce a qualitative design tool rather than a definitive quantitative guide.

Once the imaging frame-rate goes above a threshold value, the available imaging resolution will drop due to camera limitations. When this occurs, a decrease in spatial resolution will take place due to each pixel representing a larger area of the specimen. Some cameras (such as the Shimadzu HPV-X) can image at full resolution independently of the frame-rate, however they tend to have higher levels of pixel noise and lower maximum resolutions (400×250 px for the Shimadzu HPV-X for example). The reader is referred to `http://photodyn.org/tools/ultra-high-speed-camera` for a brief overview of high speed camera technologies and their limitations.

Range of testable frequencies

Assuming that the imaging frame-rate must be a minimum of 20 times the primary loading frequency in order to allow for the FFT to achieve sufficiently narrow frequency bands, fig. C.25 shows the nominal displacement amplitude and DIC displacement resolution vs loading frequency for the setup described using two representative cameras. Of particular interest are 2 points:

- At a loading frequency of approximately 16 kHz, the Photron and Shimadzu cameras have equal spatial resolution; at frequencies below this, the Photron gives superior results, whereas the Shimadzu's fixed resolution dominates after this point.
- At a loading frequency of approximately 27 kHz, the displacement amplitude in the specimen is equal to the displacement resolution of the Photron camera. This implies a Signal to Noise Ratio (SNR) of 1, which is clearly likely to lead to inaccurate material characterisation.

This is not to say that testing at higher frequencies is not possible. Assuming that the speckle pattern, lighting, and DIC settings are already optimal, there are three primary ways that one can improve the SNR:

- Reduce the size of the ROI
- Increase the displacement amplitude
- Test a stiffer material

Reducing the size of the region of interest will have the effect of reducing the magnitude of the displacement resolution, however there are limits to this; as the lens zoom ratio increases, it becomes increasingly difficult to obtain sufficient light.

Increasing the displacement amplitude will increase the magnitude of the signal, however this risks damaging the specimen and/or moving the stress state out of the linear regime. Depending on the material, the linear strain regime may be small.

Increasing the shear modulus of the material will increase the wave-speed, allowing for a corresponding increase in displacement amplitude for the same strain amplitude (see eq. (C.2)). This may not be possible for some materials (such as brain tissue), however many polymers

[10] In reality, there would be little point in testing a linear elastic material over a range of frequencies. In this section, the specimen is treated as linear-elastic in order to simplify the example

stiffen when their temperature decreases. This would have the benefit of not only improving the SNR, but also allowing for the use of TTS to extrapolate behaviour at even higher frequencies.

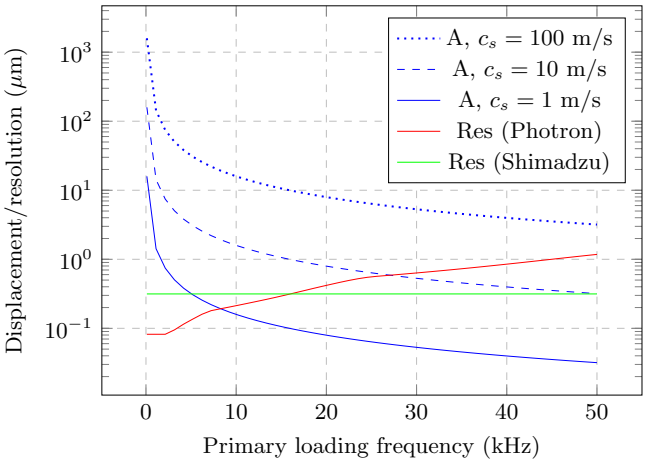


Figure C.25: Specimen displacement amplitude (A) and DIC displacement resolution (Res) vs loading frequency for example problem considering specimens with three different shear wave speeds. Cameras shown are approximately representative of Photron FASTCAM SA-X2 1080K-M4 and Shimadzu HPV-X

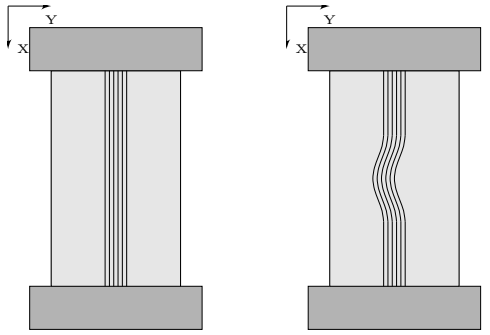
Caveats

The curves shown in fig. C.25 are broadly representative, but are meant as a qualitative guide rather than a quantitative specification. In reality, the shear modulus of a visco-elastic material would increase with frequency, causing an increase in shear wavespeed and a corresponding increase in the required displacement amplitude. Additionally, the displacement and shear resolution of DIC drop off rapidly as the magnitude of the strain gradients increase (see Appendix A for an example). This exercise is useful as a guide to camera selection, however, as well as for providing an initial estimate of the feasibility of a proposed experimental setup.

Appendix D. Quasi-1D nature of the problem

The primary requirements for the following model is that the displacements are small, and the material response is linear. This results in a simple planar stress state in the specimen, allowing for the use of the 2D VFM. Crucially, there are no tractions normal to the radial face of the cylinder. In addition to the calculations shown below, multiple FEA simulations have confirmed the validity of the assumptions and simplifications below.

Consider the cylinder shown in fig. 1 reproduced in fig. D.26, using polar co-ordinates instead of Cartesian co-ordinates. The rotation angle θ is a function of H and



(a) $t = 0$ ms (b) $t = 3.5$ ms

Figure D.26: Copy of fig. 1, replicated here for reader convenience

time alone, such that $\theta = \theta(H, t)$. Provided that θ remains small and that the material response remains linear, the displacement in polar co-ordinates (R, Θ, H) will simply be given by:

$$\boldsymbol{u}(R, \Theta, H, t) = (0, \theta R, 0) \tag{D.1}$$

Calculating the infinitesimal strain tensor in polar co-ordinates:

$$\boldsymbol{\epsilon} = \begin{bmatrix} 0 & 0 & 0 \\ 0 & 0 & \frac{\partial \theta}{\partial H}\frac{R}{2} \\ 0 & \frac{\partial \theta}{\partial H}\frac{R}{2} & 0 \end{bmatrix} \tag{D.2}$$

This shows that the stress state is 2 dimensional, with no stresses on the R face of the material. This gives a plane stress state as required by the 2D VFM (in much the same way as a thin walled cylinder specimen would).

The above cylindrical co-ordinates relate to the Cartesian co-ordinate system used throughout the paper as follows[11]:

$$(X, Y, Z) = (H, Rcos(\Theta), Rsin(\Theta)) \tag{D.3}$$

In Cartesian co-ordinates, at the surface of the cylinder where $Y = 0$, and $R = R_0$ (the ROI shown in fig. 1):

$$\boldsymbol{u} = (0, \theta R_0, 0) \tag{D.4}$$

and the strain will be:

$$\boldsymbol{\epsilon} = \begin{bmatrix} 0 & \frac{\partial \theta}{\partial X}\frac{R_0}{2} & 0 \\ \frac{\partial \theta}{\partial X}\frac{R_0}{2} & 0 & 0 \\ 0 & 0 & 0 \end{bmatrix} \tag{D.5}$$

Integrating the VFM along the narrow central strip shown in fig. 1 is technically a 2D problem, however the rotational symmetry of the problem and the narrowness of the measured strip means that the stress and acceleration distribution does not vary with Y. As a result, the problem is *de facto* 1D, with simple thickness terms in both the Y and the Z direction.

Centripetal forces

The above analysis assumes that dynamic displacements involve small displacements, and that centripetal forces remain negligible. In this set of experiments they are (something that was confirmed by the simulations), however even substantial centripetal forces will not have a significant effect on the above analysis. The stresses due to the centripetal forces will act in the zz (outward radial) direction, and as such will have no effect on the lateral acceleration of the material or the calculation of the shear VFM.

[11] The somewhat strange conversion from cylindrical to cartesian co-ordinates is a result of the co-ordinate system used in this paper, where the X axis aligns with the axis of the cylinder, rather than the more conventional system where the Z axis would align with the Z axis of the cylinder

Statement of Authorship for joint/multi-authored papers for PGR thesis

To appear at the end of each thesis chapter submitted as an article/paper

The statement shall describe the candidate's and co-authors' independent research contributions in the thesis publications. For each publication there should exist a complete statement that is to be filled out and signed by the candidate and supervisor **(only required where there isn't already a statement of contribution within the paper itself).**

Title of Paper	Characterising the frequency-response of ultra-soft polymers with the Virtual Fields Method
Publication Status	■ Published □ Accepted for Publication □Submitted for Publication □Unpublished and unsubmitted work written in a manuscript style
Publication Details	Graham, A. and Siviour, C., 2021. Characterising the frequency-response of ultra-soft polymers with the Virtual Fields Method. Strain, 57(5), p.e12386.

Student Confirmation

Student Name:	Aaron Graham		
Contribution to the Paper	Performed apparatus and analysis design, built apparatus, conducted experiments and analysis on samples, interpreted data, wrote manuscript		
Signature		Date	5-04-2024

Supervisor Confirmation

By signing the Statement of Authorship, you are certifying that the candidate made a substantial contribution to the publication, and that the description described above is accurate.

Supervisor name and title: Professor Clive Siviour		
Supervisor comments The statement above is correct.		
Signature 	Date	06/03/2024

This completed form should be included in the thesis, at the end of the relevant chapter.

5

Mechanical Properties of Sylgard184 over a wide range of frequencies, temperatures, and crosslinker ratios

In this chapter the techniques developed in chapter 4 are used to characterise the mechanical properties of a commercial PDMS elastomer over a wide range of frequencies, temperatures, and amounts of crosslinking.

In addition to characterising this material over a range of conditions that would be difficult or impossible using traditional engineering test techniques, this work showed that the curing dynamics of this material are substantially different from those on the manufacturer's datasheet. This likely explains some of the variance in reported properties for this material in the literature.

Mechanical properties of Sylgard 184 over a wide range of frequencies, temperatures, and crosslinker ratios

Aaron Graham*, Jasper Threadingham, Clive Siviour
Department of Engineering Science, University of Oxford, UK

Abstract

Silicone elastomers are often used as potting compounds for electronic devices. Effective use of these materials requires an understanding of the mechanical response at a wide range of frequencies; however, reliable data on this response are difficult to find. This paper reports data on the mechnaical response of Sylgard 184 with different amounts of cross-linker showing how the cross-linker can be used to contril the properties, and providing an important dataset. Experiments were performed at frequencies from 0.01 to 10 Hz, and different temperatures, allowing the frequency range to be expanded using Time Temperature Superposition. Further, a novel experimental method was used to expand the frequency range to 2000 Hz for two of the materials. In addition to providing important data, this paper demonstrates that TTS on silicone elastomers must account for the temperature dependence of the long-term modulus, and also the importance of ensuring that the material is fully cured before characterisation. The latter may explain discrepancies in data obtained form the literature.

Keywords: PolyDimethylSiloxane, High Rate, Frequency Response, DIC

1. Introduction

Polydimethylsiloxane (PDMS) is a popular material used in a variety of applications[1], ranging from micro-optic systems[2, 3] and micromechanical sensors, to micro-fluidic devices to biological substrates[4] to tissue simulants.Furthermore, PDMS is commonly used as a potting compound for electronics, due to the easily tunable modulus thermal and mechanical stability. Finally, PDMS has seen use as a phantom for development of imaging techniques [5]. For all of these varied applications, accurate knowledge of the mechanical properties over a range of timescales is important if the design is to be successful.For example, the elastic modulus of the tissue substrate has been shown to be an important component in the regulation of cell mechanobiology [6, 7], whilst the need to understand mechanical properties of potting compounds is particularly important if we are to provide adequate protection for electronic devices that must have both a long lifetime and resistance to rapid accelerations that may occur during use, or accidentally, for example if dropped.

A particular advantage of PDMS in many of these applications is its thermal, biological, and temporal stability, as well as the wide range of achievable mechanical properties. In particular, Sylgard 184 has been widely used due to the low cost and ease of with which the mechanical properties can be tailored via adjustment of the crosslink density.

Unfortunately, there is a lack of high quality data on the mechanical properties of Sylgard 184. Figure 1 for instance, shows a selection of modulus vs crosslinker data taken from the literature. There is a large spread in the reported values, even for the nominally fully crosslinked material

*Corresponding author
Email address: Aaron.Graham@eng.ox.ac.uk (Aaron Graham)

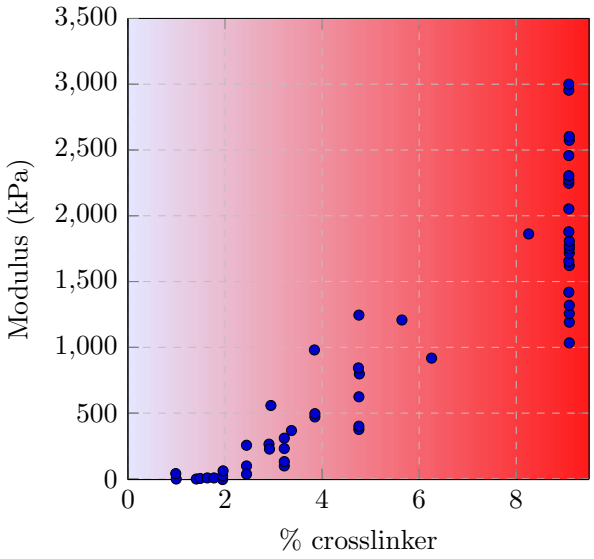


Figure 1: Reported Elastic Modulus vs crosslinking ratio for Sylgard 184, taken from Glover *et al.* Note that for an incompressible material, the Young's modulus (reported here) is approximately 3 times the shear modulus (reported in the rest of this paper)

which is fairly stiff and relatively easy to characterise. The spread in these data is even worse for the partially crosslinked material, likely in part due to the challenges inherent in mechanical testing of soft materials.

This paper addresses two gaps in the literature of significance to the use of these materials in electronics applications: accurately characterising the properties of Sylgard 184 over a large range of frequencies for a range of levels of cross-linker, including frequencies that have previously been unobtainable, and modifying the traditional TTS method to allow for better prediction of properties at high frequencies from experiments at low temperatures.

2. Experimental design

2.1. Specimen preparation

Sylgard 184 was obtained from Farnell Chemicals, and prepared according to the manufacturer's instructions. In order to investigate the effect of crosslink density on the mechanical properties, the material was mixed in a variety of ratios ranging from the manufacturer recommended 1:10 crosslinker to base ratio down to a 1:100 crosslinker to base ratio as shown in section 2.1. Representative data for the moduli of these resin ratios are shown for context.

Resin:crosslinker ratio	**Shear mod (kPa)**	
10:1 ("100%")	654	871
20:1 ("50%")	184	255
40:1 ("25%")	11.7	23.9
50:1 ("20%")	4.67	12.6
66.7:1 ("15%")	0.423	4.02
100:1 ("10%")	0.027	1.34

Table 1: Modulus vs crosslinker ratio for Sylgard 184 at 0.1 Hz and 10 Hz at 20° C. Data from experiments conducted by author.

The uncured material was mixed vigorously with a polymer stir rod, taking care to scrape material from the walls and base of the beaker when stirring. The thoroughly stirred mixture was then vacuum degassed for approximately 5 minutes at 5 kPa (absolute). Specimens were cured for 3 hours at 80 °C, in order to ensure that specimens were fully cured before testing. This is substantially longer than the curing time nominally required; however, it was necessary in order to ensure fully cured material, Appendix A.

2.2. Experimental procedure

2.3. Low frequency experiments

Low frequency experiments were performed on an Anton Paar MCR Physica 301 rheometer using isothermal frequency sweeps from -30 °C up to 80 °C in steps of 10 °C. The samples were loaded in sinusoidal oscillation at frequencies from 0.01 Hz up to 10 Hz with five measurement points per decade of frequency and a strain amplitude of 0.2%. Specimens were cured *in situ* on the rheometer, in order to avoid damage to the material when moving specimens from a mould to the test apparatus.

In order to cure the material on the Rheometer, a large brass ring with an internal diameter of approximately 50 mm was placed onto the bottom

platen, and then a calculated[1] amount of uncured material was poured into it. An insulating shroud was then placed over the lower platen in order to reduce thermal gradients, and the rheometer bottom platten was set to the desired curing temperature. Once curing was complete, the rheometer head could be brought down in contact with the cured specimen, and any excess could be trimmed if necessary. This *in situ* cure was particularly useful for the very soft specimens. fig. 7 was taken post-testing of a very soft sample in order to document the extreme stickiness and low modulus, however the brass ring used to contain the sample during curing can also be seen in this image.

Curing the material *ex situ* was not feasible for the softer specimens, owing to the low modulus and strength and high stickiness. This experimental methodology greatly increased the time taken per test, but ensured that each tested specimen was pristine and undamaged.

In order to ensure that the specimen was fully cured, the set of isotherms was run twice – once from -30 °C up to 80 °C and then back down to -30 °C. If the results of the second set of isotherms were different from the first, that would imply that additional curing took place during the experiment and that the material was not fully cured prior to testing.

After each set of isothermal frequency sweep curves had been generated, TTS analysis was run in order to generate a mastercurve for each material. It should be noted that traditional TTS analysis was not possible on this material; this is further discussed in section 3 and section 4.2

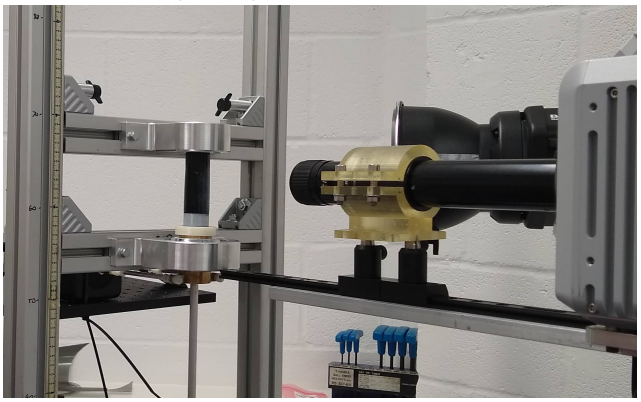
[1] Calculated based on the desired thickness, taking the diameter into account

2.4. High rate tests

Each material was characterised at high frequencies using the methodology developed in [8]. The material preparation was identical to the low rate specimens, however the specimen geometry was different. For these tests, each specimen was a 30 mm diameter cylinder, loaded in dynamic torsion, with Digital Image Correlation (DIC) used to track the full-field deformation and the Virtual Fields Method (VFM) used to extract the mechanical properties for each test. Figure 2 shows a specimen being cast, and an image of the high rate apparatus. For more detail on the methodology, apparatus, and analysis, the reader is referred to [8].



(a) Specimen for high rate test during casting



(b) Experimental apparatus for high rate testing

Figure 2: Specimen for high rate testing being tested

3. Low rate data

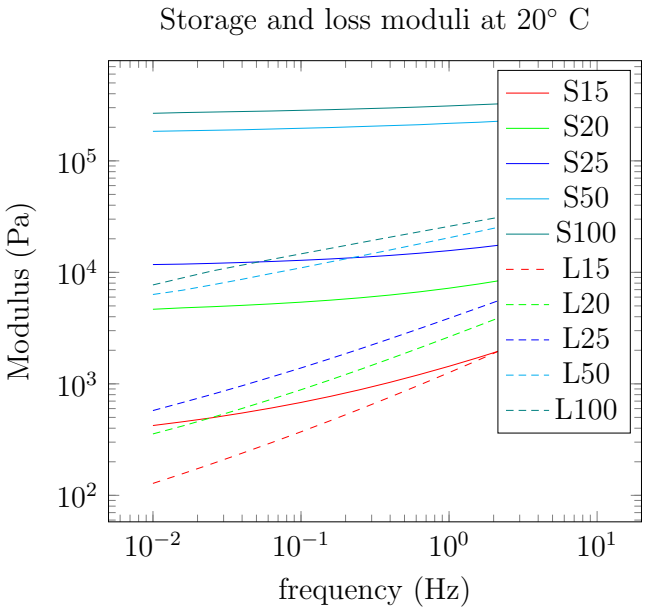


Figure 3: Storage (S) and loss (L) modulus vs frequency at 20°C for Sylgard 184 for a range of crosslinker concentrations ranging from 15% of the recommended amount up to 100% of the recommended amount. Storage moduli shown with solid lines, and corresponding loss moduli shown with dashed lines of the same colour

Figure 3 shows a subset of the low rate results at 20 °C, with the storage moduli shown by solid lines and the loss moduli by dashed lines. Note the wide range of moduli achieved simply by varying the level of cross-linking. Figure 4 shows the storage moduli at 20 °C and 0.1 and 10 Hz for a range of crosslinker ratios, giving an indication of the rance of moduli obtainable. See Appendix C for additional plots, showing the full range of low rate results, such as tests at different temperatures.

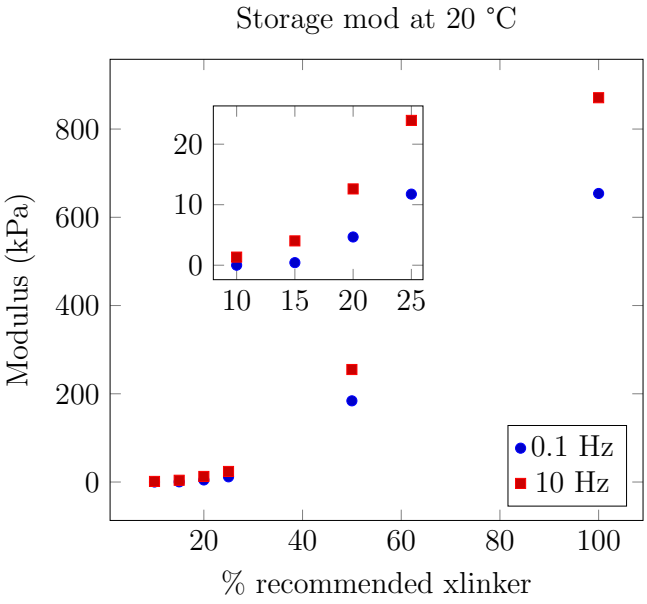


Figure 4: Measured shear storage modulus vs % recommended crosslinker at 0.1 and 10 Hz and 20° C

As can be seen from fig. 5, the isothermal frequency sweeps exhibit substantial overlap. This prevents TTS via just lateral shifting of isotherms, as the lines already overlap. As a result, conducting traditional TTS analysis on this data is not meaningful, and a new methodology is required. Appendix C shows further plots of the isothermal frequency sweep results for all polymers tested.

It should be noted that some TTS methods can generate a smooth curve from these data via the application of both vertical and horizontal shifting. Whilst vertical shifting in order to compen-

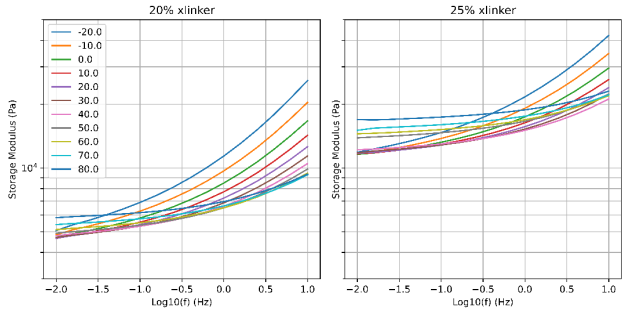


Figure 5: Isothermal frequency sweeps on Sylgard 184 with 20 and 25% of the recommended crosslinker. Note the overlap of the curves at lower frequencies. Data for other materials is shown in Appendix C

sate for volume changes caused by thermal expansion/contraction is valid, some TTS methods shift vertically in order to generate a "good" curve rather than to compensate for volume changes. This results in a superficially good TTS fit, but, as shown later, can lead to invalid results.

4. TTS shifting and high rate data

4.1. TTS

As shown in fig. 5, meaningful TTS analysis using traditional methods is not feasible. Instead, a modified version of TTS was conducted under the assumption that the long term modulus increased with temperature[2], whilst the viscous branches of the polymer behaved as expected, softening with temperature. This effect is supported by fig. B.10, which shows the extracted elastic modulus vs temperature for the fully crosslinked material.

Under this assumption, the following method was used for TTS shifting:

1. Subtract the long term modulus from the isotherm, splitting it into two portions – the viscoelastic branches and the purely elastic branch
2. Conduct TTS shifting on the viscoelastic branches using standard TTS methods
3. Add TTS mastercurve for the viscouscoelastic branches to the relevant long term modulus for each temperature

Two methods were attempted for extracting the long term modulus:

- For each isothermal frequency sweep, gather a single additional datapoint, at a very low frequency.
- Fit a Prony series to the isotherm, overfitting is fine (as the purpose is to best predict the long-term modulus rather than do any efficient modelling). Then extract the long term modulus from the fitted Prony Series

[2]This is predicted by thermodynamics if one assumes the elastic stretching of a material to be isentropic; in order to preserve entropy, the modulus must increase with increasing temperature. This phenomena has been predicted by Kelvin [9] and Joule [10] as early as the 1800s

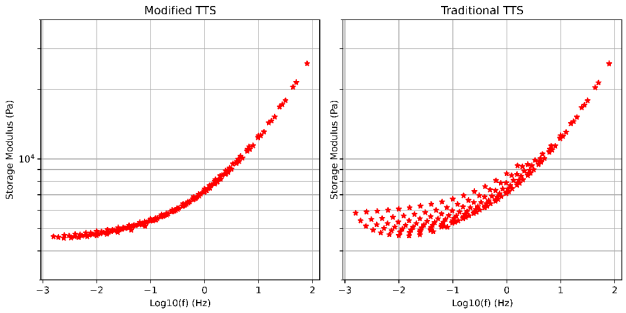


Figure 6: Example of modified TTS vs traditional TTS

Both methods have their limitations. The first has the advantage of providing "real" data and not simply an extrapolation, however it is not practical to test the material at very low frequencies. In practice, these data were sampled a decade below the lowest frequency used for the isothermal frequency sweep described earlier; this still took a very long time to acquire, and whilst the sample is expected to be closer to the elastic modulus, it will still include contributions from the viscous branches.

The second method has the advantage of being fast and efficient to conduct, and can theoretically get a closer approximation of the elastic branch, but is likely to be less accurate, as it is an extrapolation rather than a measurement.

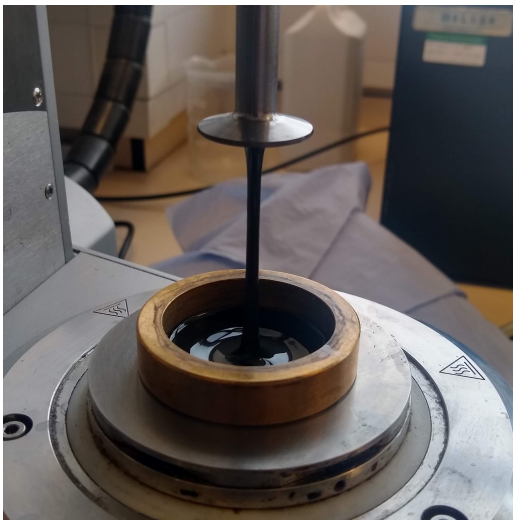


Figure 7: 10 % crosslinked specimen sticking to rheometer head after testing.

In practice, both have their limitations, but both are significant improvements on traditional TTS. This can be seen in fig. 6, where traditional TTS is not capable of generating a reliable mastercurve. It is only for the 10% and 15% crosslinked material that this modified TTS method is not required; however, that is due to the fact that the elastic branch of these materials is negligible in comparison to the viscous branches. The minimal contribution of the elastic branch can be seen in section 2.1, where the material with less crosslinker is more sensitive to frequency. Figure 7 shows an image of a sample of 10 % crosslinked Sylgard sticking to the rheometer head after testing is complete – note the strong adhesion to the rheometer head, and large deformation; at low levels of crosslinker, Sylgard behaves more as a fluid than a solid, with little detectable long term modulus.

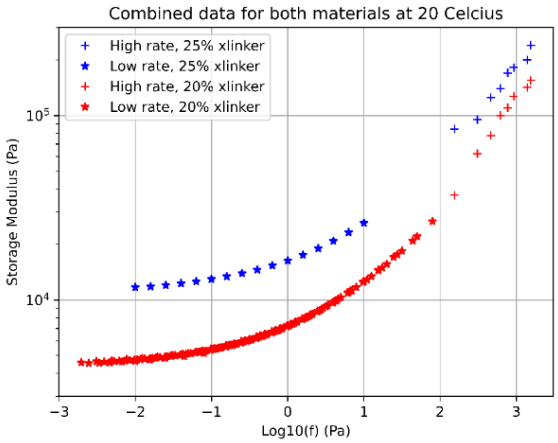


Figure 8: Combined high and low rate data, making use of the modified TTS for the low rate data

4.2. Combined high and low rate results

As shown in fig. 6, the modified TTS method works significantly better than traditional TTS. However, it is still of significant value to have direct measurements of the high frequency response, whether as a means to provide additional data or to benchmark values derived from TTS.

Figure 8 shows a full curve of modulus vs frequency data, combining the TTS output with the directly measured high rate response for 20 and 25% crosslinked material. The apparent consistency between the high rate measurements and the TTS curve appears to validate the modified TTS method.

5. Discussion and conclusion

As shown in fig. 1, there is a large spread in the properties for S184 that are quoted in the literature. This is likely due to insufficiently cured specimens being tested, as this research has shown that specimens need to be cured for substantially longer than the manufacturer recommends. Importantly, this need for additional curing is true for both the fully cross-linked and the partially cross-linked material. This does not explain all of the variance however – the data found in these experiments are at the upper end of those quoted in the literature, even if not the highest. The large spread in data for partially cross-linked material is likely to additionally be due to the challenges inherent to testing very soft materials, but this does not explain the large variance in measured properties for the nominally fully cured material.

Importantly, the long term modulus of the material increases with increasing temperature, behaving differently from the viscous branches of the material. If this is not taken into account when performing TTS, the end results of the TTS analysis are likely to be incorrect. This is particularly important as TTS is often effectively unfalsifiable, as the predicted moduli at at frequencies that are extremely challenging to test using conventional test methodology

The modified TTS conducted in this set of experiments generates a methodology of extending the range of predicted behaviours in a way that traditional TTS cannot. Whilst traditional TTS methods utilising both horizontal and vertical shifts can result in a curve that looks reasonable at first glance, this curve will incorrectly predict behaviour at frequencies outside of the testing parameters – this has been shown with the very low frequency tests performed on this material.

References

[1] V. Placet, P. Delobelle, Mechanical properties of bulk polydimethylsiloxane for microfluidics over a large range of frequencies and aging times, Journal of Micromechanics and Microengineering 25 (2015).

[2] F. Schneider, J. Draheim, R. Kamberger, U. Wallrabe, Process and material properties of polydimethylsiloxane (pdms) for optical mems, Sensors and Actuators, A: Physical 151 (2009) 95–99.

[3] F. Schneider, T. Fellner, J. Wilde, U. Wallrabe, Mechanical properties of silicones for mems, Journal of Micromechanics and Microengineering 18 (2008).

[4] J. N. Lee, X. Jiang, D. Ryan, G. M. Whitesides, Compatibility of mammalian cells on surfaces of poly(dimethylsiloxane), Langmuir 20 (2004) 11684–11691.

[5] G. Lamouche, B. F. Kennedy, K. M. Kennedy, C.-E. Bisaillon, A. Curatolo, G. Campbell, V. Pazos, D. D. Sampson, Review of tissue simulating phantoms with controllable optical, mechanical and structural properties for use in optical coherence tomography., Biomedical optics express 3 (2012) 1381–98.

[6] R. N. Palchesko, L. Zhang, Y. Sun, A. W. Feinberg, Development of polydimethylsiloxane substrates with tunable elastic modulus to study cell mechanobiology in muscle and nerve, PLoS ONE 7 (2012).

[7] C. Kayal, E. Moeendarbary, R. J. Shipley, J. B. Phillips, Mechanical response of neural cells to physiologically relevant stiffness gradients, Advanced Healthcare Materials 9 (2020).

[8] A. Graham, C. Siviour, Characterising the frequency-response of ultra-soft polymers with the virtual fields method, Strain 57 (2021) e12386.

[9] L. Kelvin, The rubber elastic state, Quarterly Journal Math (1857).

[10] J. P. Joule, On some thermo-dynamic properties of solids, Philosophical Transactions (1859).

[11] M. T. Elsmore, D. S. De Focatiis, Combined roles of temperature and humidity on cure of a silicone elastomer, Polymer Testing 93 (2021) 106967.

[12] P. J. Scott, V. Meenakshisundaram, N. A. Chartrain, J. M. Sirrine, C. B. Williams, T. E. Long, Additive manufacturing of hydrocarbon elastomers via simultaneous chain extension and cross-linking of hydrogenated polybutadiene, ACS Applied Polymer Materials 1 (2019) 684–690.

Appendix A. Curing

The manufacturer recommended curing times are as follows[3]:

Temp °C	Cure time
25	48 hours
100	35 mins
125	20 mins
150	10 mins

Table A.2: Cure time vs temperature for Sylgard 184

Fitting the following exponential to the data in table A.2 results in the following expression for cure time vs temperatre, with an R^2 value of 99.94:

$$t = 1.169E6T^{-3.139} \quad \text{(A.1)}$$

where t represents the cure time in hours, and T represents the temperature in degrees Celcius.

Fitting an exponential curve to the data in table A.2 implied a cure time of 75 minutes when curing at 80° C. The samples for this paper were cured at 80° C for 3 hours before testing, resulting in a cure time of approximately 2.4 times that recommended. In reality the cure time was slightly longer, as the samples were given time to equilibrate before the 3 hour cure was considered to have started.

In order to evaluate the veracity of the manufacturer recommended cure time at room temperature, a simple test was conducted where a sample was cured *in situ* on the rheometer, with stiffness measurements taken intermittently during the curing process. This test showed that the material had not fully cured after 48 hrs. Given that the modulus at 0.1 Hz and 25° C stabilised at approximately 11.7 kPa for this material (see section 2.1), it is likely that the material was almost cured after approximately 70-80 hours. This further supports the decision to cure the material for substantially longer than the recommended cure time.

[3] https://www.dow.com/en-us/document-viewer.html?docPath=/content/dam/dcc/documents/11/11-3184-01-sylgard-184-elastomer.pdf

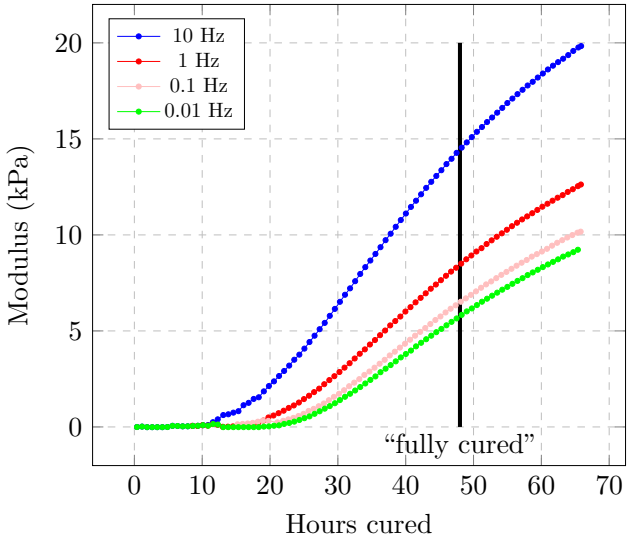


Figure A.9: Modulus vs cure time. Note that 48 hours is nominally fully cured

Fitting a curing model such as the Hsich model (see [11]) was considered, however the Hsich model did not fit particularly well, with the initial gradient being too steep. These curves look a lot more like sigmoid fits, particularly given the zero initial gradient. The inflection point occurs between the hours of 30 and 40, further suggesting that curing will be largely complete by hour 70-80.

Appendix B. Long term modulus vs temperature

In general, it is expected that the Modulus of a cross-linked elastomer will be given by[12]:

$$G_0 = \frac{3\rho RT}{\bar{M}_e} \tag{B.1}$$

where G_0 is the long term shear storage modulus, ρ is the density, R is the ideal gas constant, T is the temperature, and $\bar{M}_e$ is the molecular weight between crosslinks. As the polymer cures and the crosslink density increases, the molecular weight between crosslinks $\bar{M}_c$ decreases, resulting in an increase in the long term modulus.

For a fully cured crosslinked elastomer (i.e. $\bar{M}_e$ constant), the long term modulus is predicted to be linearly dependant on temperature. This effect appears to be shown in fig. B.10, where the modulus is (almost) linearly dependant on temperature.

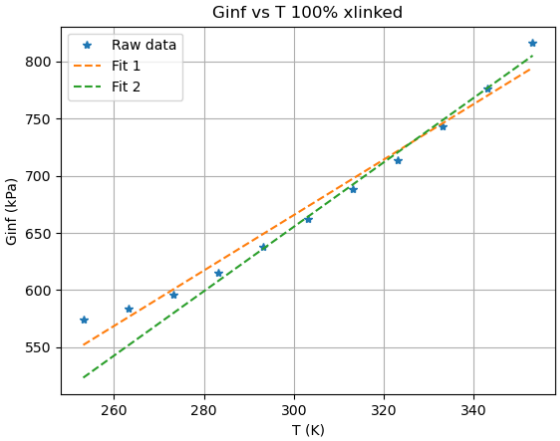


Figure B.10: Long term shear modulus vs temperature for fully cured Sylgard 184. Note the linearity, suggesting (partial) adherence to the statistical thermodynamic theory of rubber elasticity.

Appendix C. Supplemental plots

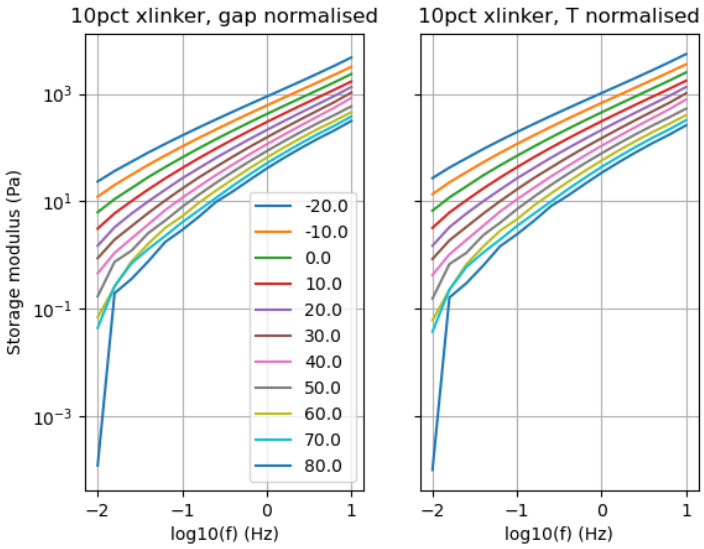


Figure C.11: Isothermal frequency sweeps for Sylgard 184 with 10% of the recommended xlinker

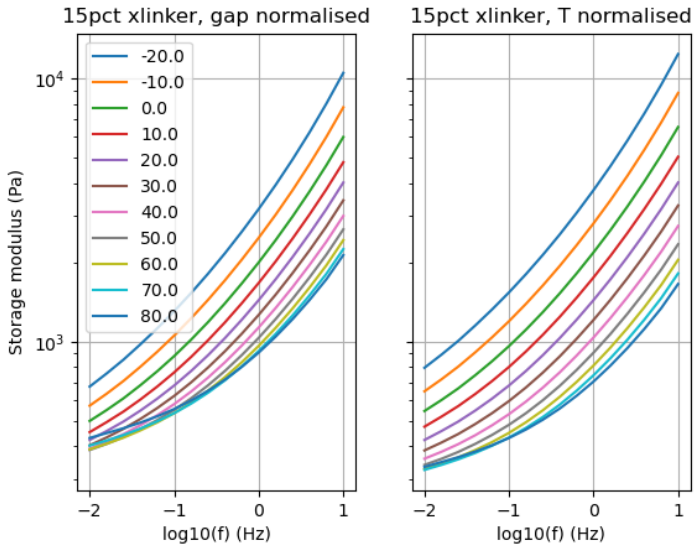


Figure C.12: Isothermal frequency sweeps for Sylgard 184 with 15% of the recommended xlinker

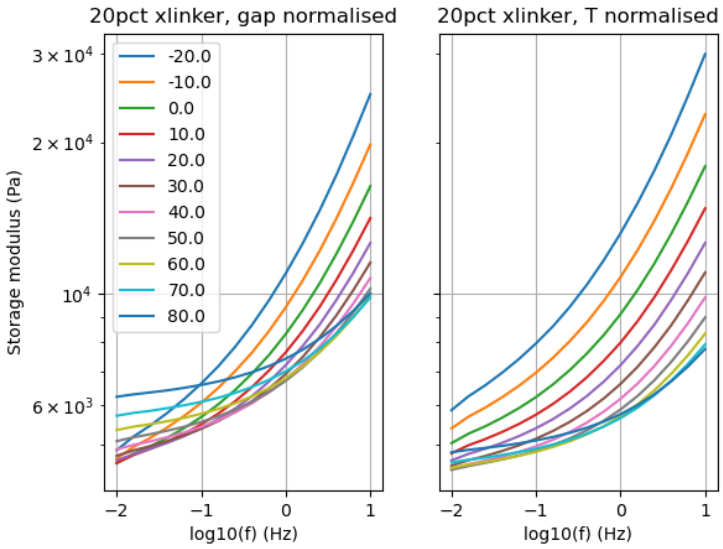


Figure C.13: Isothermal frequency sweeps for Sylgard 184 with 20% of the recommended xlinker

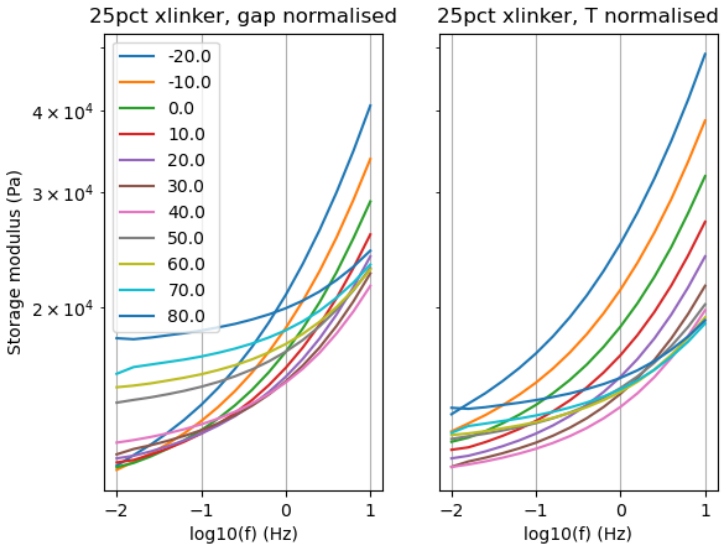


Figure C.14: Isothermal frequency sweeps for Sylgard 184 with 25% of the recommended xlinker

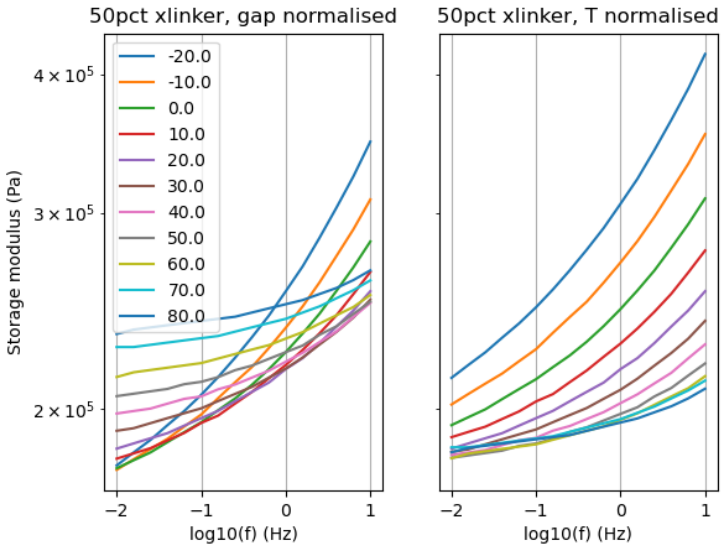


Figure C.15: Isothermal frequency sweeps for Sylgard 184 with 50% of the recommended xlinker

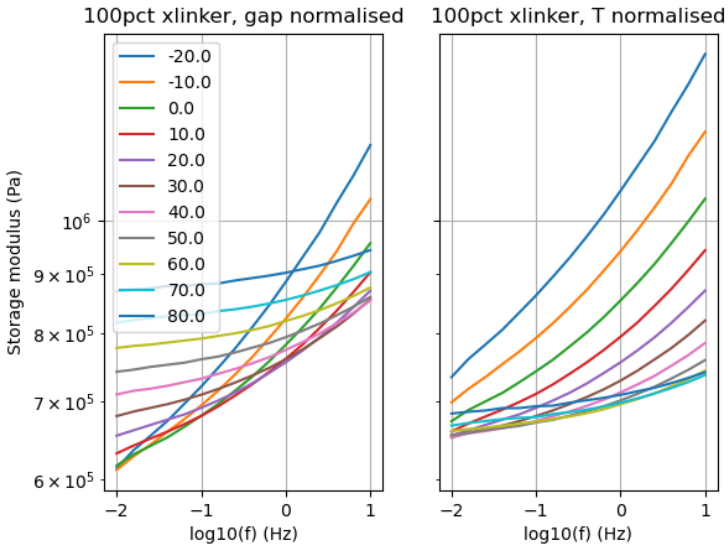


Figure C.16: Isothermal frequency sweeps for Sylgard 184 with 100% of the recommended xlinker

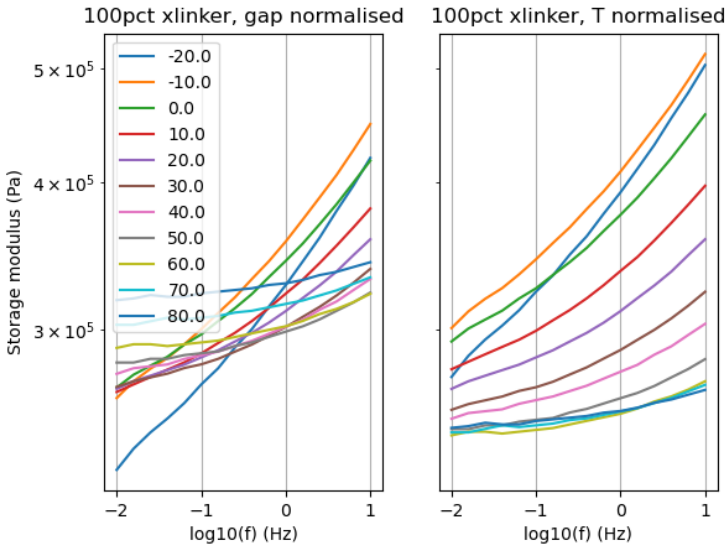


Figure C.17: Isothermal frequency sweeps for Sylgard 184 with 100+% of the recommended xlinker, after curing it for only the manufacturer recommended duration

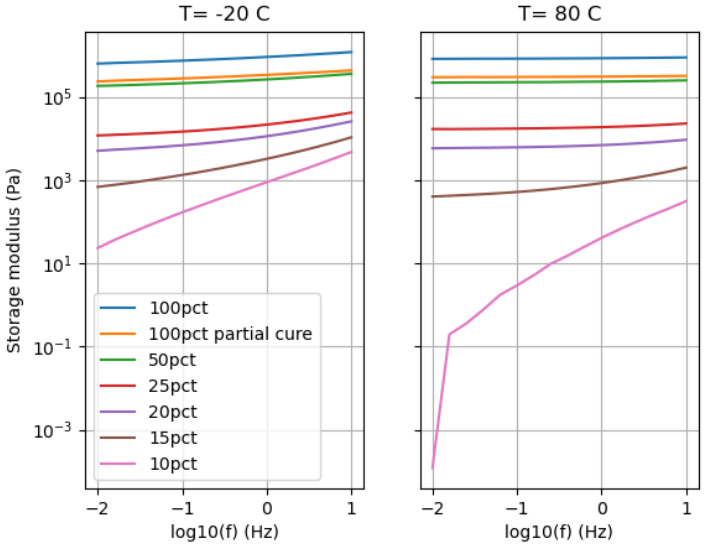


Figure C.18: Isothermal frequency sweeps for Sylgard 184 with varying amounts of crosslinker. Note that the data includes a test on Sylgard cured after the manufacturer recommended curing time

Statement of Authorship for joint/multi-authored papers for PGR thesis

To appear at the end of each thesis chapter submitted as an article/paper

The statement shall describe the candidate's and co-authors' independent research contributions in the thesis publications. For each publication there should exist a complete statement that is to be filled out and signed by the candidate and supervisor **(only required where there isn't already a statement of contribution within the paper itself).**

Title of Paper	Mechanical properties of Sylgard 184 over a wide range of frequencies, temperatures, and crosslinker ratios
Publication Status	□Published □ Accepted for Publication □Submitted for Publication ■Unpublished and unsubmitted work written in a manuscript style
Publication Details	

Student Confirmation

Student Name:	Aaron Graham		
Contribution to the Paper	Prepared samples, performed experiments and analysis on samples, interpreted data, wrote manuscript. Approximately half of low-rate (rheometry) experiments were conducted alongside a 4th year student whom I was supervising.		
Signature		Date	05-04-2024

Supervisor Confirmation

By signing the Statement of Authorship, you are certifying that the candidate made a substantial contribution to the publication, and that the description described above is accurate.

Supervisor name and title: Professor Clive Siviour		
Supervisor comments The statement above is correct.		
Signature 	Date	06/03/2024

This completed form should be included in the thesis, at the end of the relevant chapter.

6

Tests on Brain tissue and Agarose

This chapter reports on the testing of porcine brain tissue over a range of frequencies and temperatures, as well as the testing of agarose gel at a range of frequencies, temperatures, and concentrations.

In addition to obtaining results at frequencies that would not be obtainable using traditional test methodologies, these tests were able to largely avoid issues of inter-specimen variability due to the non-destructive nature of the tests, in spite of the tests being conducted at high rates.

Dynamic response of brain tissue and agarose gel

Aaron Graham*, Clive R Siviour

Department of Engineering Science, University of Oxford, UK

Abstract

The ability to produce representative models of biological systems under high strain rate and impact loading is of increasing importance in design of systems to protect from injury. However, making accurate measurements of the mechanical response of soft biological tissues is challenging. Moreover, the limited availability of these materials means that appropriate 'phantoms' are often required. This paper presents data on the frequency dependant complex modulus of brain tissue and an agarose gel phantom, the latter at various concentrations . Low frequency testing is conducted on a traditional rheometer, whilst high frequency characterisation is performed using a novel apparatus and analysis method previously developed by the authors. This novel methodology uses a combination of Digital Image Correlation (DIC) and the Virtual Fields Method (VFM) for non-contact stress and strain measurements, allowing accurate full-field anaysis to be performed that enables material properties to be extracted at frequencies that would be difficult or impossible to achieve using traditional engineering test methodologies.

1. Introduction

Agarose is a natural polymer with excellent biocompatibility and easily tuned mechanical and chemical properties. It has strong structural similarity to the extra-cellular matrix, and is commonly used as a substrate to support cell growth. Like agarose, brain tissue is a natural material. Unlike agarose, brain tissue is one of the most important and least understood tissues in the human body[1, 2, 3, 4]. It is the softest biological tissue by orders of magnitude, and is highly sensitive to boundary conditions[5].

Whilst there is a wealth of data on the mechanical properties of agarose gel and brain tissue at low strain rates, there is a paucity at high rates, or, equivalently, high frequencies[6]. If brain tissue is to be modelled at high rates, or if agarose is to be used as a tissue phantom, particularly for events that incorporate high rate deformation or impact loading, it is important that there is high quality data on the high rate mechanical properties. This is addressed in the current work.

1.1. Brain tissue

When loaded in shear, brain tissue is the softest human tissue, with a shear modulus of around 1 kPa [7]. In contrast, the bulk modulus of brain tissue is approximately 2 GPa, making it almost incompressible [8]. This makes it particularly important that the deviatoric and dilatational response be separated when testing at high rates, in order to avoid inertial effects. The extreme softness and sensitivity to accurately measured boundary conditions makes brain tissue challenging to accurately characterise. This apparatus and methodology mitigates these issues via the use of the VFM, allowing for non-contact stress and strain measurements, as well as the removal of boundary stresses from the calculations.

*Corresponding author

Email address: Aaron.Graham@eng.ox.ac.uk (Aaron Graham)

1.2. Agarose and bio-polymers/gels

Agarose gel is widely used as a cell growth substrate in petri dishes, as a medium in electrophoresis, in food products, and in a host of other applications including as a phantom material for biological tissues [9, 10, 11, 12, 13, 14]. In this last application, characterisation and control of the mechanical properties is crucial [14], particularly concerning frequency dependence. This can also be important in other, and perhaps unexpected, contexts; for example, it has been shown that the mechanical properties of a tissue substrate can have a strong influence on the behaviour of the cells grown on said substrate [9].

1.3. DIC and the VFM

Digital Image Correlation (DIC) is a non-contact full-field optical metrology method capable of measuring surface displacement fields with a resolution of 0.01 pixels or better [15]. This is achieved by tracking the deformation of an image via cross-correlation with a reference (undeformed) image [16]. The image is required to have a high information content, which is often achieved by marking the surface of interest with speckles. These speckles are ideally randomly distributed, make up approximately half the surface area of the specimen, and have a size of 3-5 pixels. It should be noted that whilst DIC is often described as a "non-contact" measurement method, the paint itself is in contact with the specimen. This is not important when testing rigid materials like metals, but is important when testing very soft specimens – standard paints are orders of magnitude stiffer than agarose gels.

1.3.1. Speckling biological tissue and bio-polymers

The creation of speckle patterns on biological tissues and soft biopolymers can be particularly challenging [17]. Not only is stiffness a concern, surface preparation must be performed in such a way that the specimen does not experience dehydration, must not alter the behaviour of the specimen, and must allow the speckles to withstand large deformations without losing contact with the underlying surface. The use of dyes such as methylene blue has previously alowed successful creation of a dark background for DIC speckles on porcine ligament tissue [17], with the dye staining the underlying tissue; however standard white paint was still used for the speckles themselves. Other methods used include the sprinkling of spherical granules with a controlled particle size such that each speckle is a single particle, however this method suffers from challenges in ensuring adhesion between the particles and the substrate [18]. If using standard paint to generate the speckle pattern, the issue of excessive paint stiffness has also been avoided by testing the specimen while the paint is still wet.

1.3.2. VFM

The Virtual Fields Method (VFM) makes use of the principle of virtual work in order to extract constitutive properties from an experiment, exploiting the rich full-field data made available by DIC. The VFM used in this set of experiments is described in [19]; for a detailed overview the reader is directed to that paper. For a more general and comprehensive overview of the VFM, the reader is directed to [15]. As reported in [19], the application of DIC and the VFM in the experiments described in the current papers enabled calculation of full-field storage and loss moduli at a range of frequencies.

A particular advantage of the dynamic VFM is that it is not required to measure the tractions at the edges of the specimen [16]. This is an advantage for high rate tests where accurate measurement of the surface tractions can be challenging, but it is additionally advantageous when measuring soft materials. Small changes in boundary conditions have been shown to have large effects on the properties obtained from tests on low modulus materials such as agarose and brain tissue [1, 20, 6], necessitating very careful control of boundary tractions. An advantage of the VFM is the removal of the effect of the boundary tractions on the experiment, improving the repeatability and quality of the experiment.

For these reasons, in the current research the VFM was used to characterise the full-field me-

chanical behaviour of agorose gel with controlled mechanical properties. This methodology has previously been used to obtain data on the high frequency properties of ultra-soft silicones that would otherwise be difficult or impossible to obtain. This methodology is even more suited to the characterisation of biological tissues and hydrogels, given that it obviates some of the issues common to testing these materials (such as extreme sensitivity to boundary conditions, and specimen heterogeneity).

2. Experimental design

2.1. Specimen preparation

2.1.1. Brain tissue

Brain tissue was acquired from the local abattoir, within 48 hours post-mortem. The brains were obtained in the form of full pig's heads, and were only extracted shortly before experimenting in order to minimise damage and disturbance to the material.

Samples of brain tissue were taken from the corpus callosum, maximising the amount of white matter in the samples. The section of interest was first cut into a flat sheet using a sharp scalpel, and then a cylindrical specimen extracted for testing on either the rheometer or the high rate apparatus. It was found that cutting the brain tissue at approximately 5° C allowed for optimal control of specimen geometry, as the brain tissue was stiffer and less ductile. Figure 1 shows a portion of porcine brain after being extracted from the skull and halved along the centre, but before samples are taken. Note the visible corpus callosum, where samples were extracted from.

For the high rate tests, once the samples of brain tissue were cut to the correct size and judged to be of sufficient dimensional accuracy[1], they were attached to the same 3d printed grip used for the agarose. It was found that attaching the tissue sample to a piece of tape which was then attached to the 3d printed grip was optimal, as it allowed for the sample location to be easily adjusted by moving the tape. The sample was attached to the tape via cyanoacrylate adhesive – this method securely attached the tissue sample without the risk of any slipping. It should be noted that this method would be substantially less valid without the use of the VFM for analysis, as the VFM can simply not consider the bottom mm of the sample in a way that traditional test methods cannot. Figure 2 shows a brain sample after gluing and prior to speckling. Note that while the specimen is predominantly white matter, it is not homogeneous.



Figure 1: Half of a porcine brain, before sample extraction. Corpus callosum is visible near the centre-right of the image, and is primarily white matter.

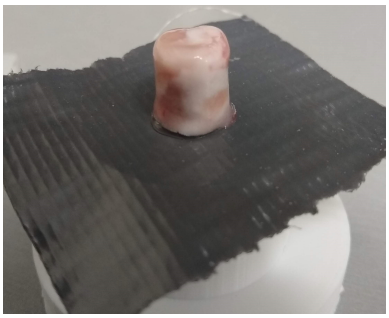


Figure 2: Cylindrical brain tissue specimen, prior to speckling. Specimen is attached to a layer of tape using cyanoacrylate adhesive, and the tape is then attached to the strain relief grip.

[1] Given the inhomogeneity of biological tissue in general and brain tissue specifically, several nominally identically prepared samples can often be of varying dimensional accuracy. The exact diameter of the samples is not important, but the axial symmetry is. This judged by slowly rotating the specimen against a reference background, giving an indication of axial symmetry.

2.1.2. Agarose gel

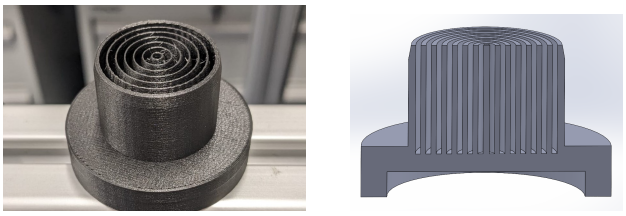
Granulated agarose was mixed with a saline solution prepared using de-ionised water and NaCl such that the salt concentration was 1 mg/ml. The agarose powder was added by weight, followed by a small quantity of carbon black in the form of lampblack. The lampblack was used purely to increase the opacity of the specimen in order to provide a dark background for the speckle pattern. For more details about the addition of the lampblack, see section 2.1.5. The solution was then heated in a beaker using a magnetic stir-bar until the temperature was 87-89 °C. Throughout the heating process the solution was intermittently vigorously agitated in order to ensure full homogenisation and mixing of the lampblack addition. Once the correct temperature was reached, the solution was re-weighed and topped up with hot de-ionised water such that the evaporated water was replaced and the correct mass ratios were maintained. The solution was then vigorously agitated, degassed at -500 kPa, and poured into the moulds.

2.1.3. Agarose concentrations

Agarose concentrations of 1.2, 2, and 4 wt% were chosen in order to cover a range of biologically relevant stiffnesses. Lower concentrations than this can be challenging to prepare due to a low propensity to gel, and very low stiffnesses. Concentrations above 4 wt% can be difficult to prepare due to difficulties involved in homogeneously dissolving the agarose powder at such high concentrations.

2.1.4. Specimen geometry

Specimens for low rate testing were prepared as flat sheets with a thickness of 1 mm, cast directly onto the lower platen of the rheometer. Once the specimen had cured, the upper platen was lowered until it was in contact, and the excess material was then cut off and removed. Casting *in situ* avoided straining or otherwise damaging the specimen, especially as the agarose was fragile at low concentrations. Casting the specimens separately and then placing them onto the rheometer plattern increases the throughput of the test



(a) Example of grip 3D printed from carbon fibre reinforced PETG

(b) Section view of mould grip

Figure 3: 3D printed mould grip. Specimen is cast into the upper portion, with the concentric rings providing bonding/strain relief between the specimen and the grip. The bottom portion of the grip then interfaces with the loading apparatus via an interference fit.

methodology, but at the cost of potentially lower quality experimental results.

Specimens for high rate tests were cast directly into the 3D printed grip mould as described in [19]. In order to ensure that the gel came into full contact with the strain relief, immediately after pouring the solution into the mould the mould was placed in a vacuum chamber and cycled to a vacuum pressure of -500 kPa, drawing out any air bubbles and ensuring that full contact with the strain relief occurred. The specimen was then cooled in a humidity controlled environment at 5 °C, and allowed to gel fully before extraction from the mould. This resulted in a cylindrical specimen with a diameter of 30 mm, with the bottom bonded securely to a 3D printed strain relief grip. This grip was then used to load the specimen, attached directly to the load apparatus. Unlike previous tests using this apparatus, the 3D printed grips had to be printed from Nylon or glass fiber reinforced PETG rather than PLA, as the PLA would not withstand the temperature of the agarose gel when it was initially poured into the mould. When not in use, these specimens were stored in a humidity controlled environment at 5 °C and 100% RH.

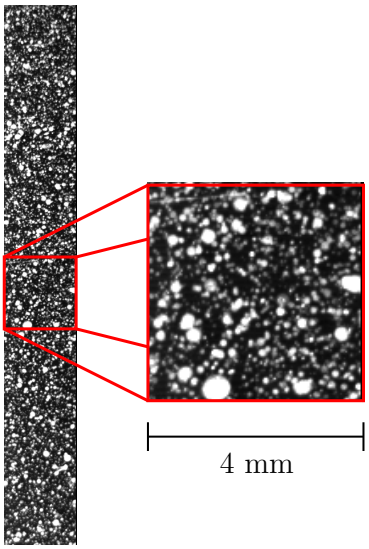
2.1.5. Speckling

The "paint" used to speckle the agarose samples was a suspension of titanium dioxide powder in distilled water, deposited on the surface of the specimen using an airbrush. This paint had the advantage of having almost no mechanical stiff-

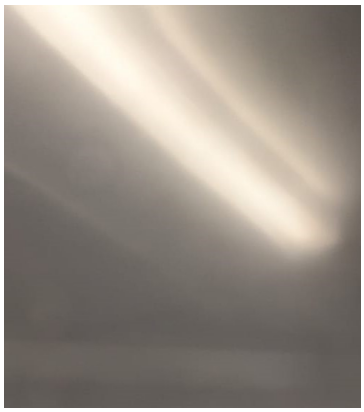
ness[2], following the deformation of the underlying surface without affecting its behaviour. The lack of a binding agent made application of the paint more difficult, but greatly reduced the chances of the paint influencing the underlying specimen either mechanically or chemically. A downside to this paint is that it is not bonded to the surface, and touching the speckled surface results in the removal or damage of the pattern. On the other hand, replacing a poor quality speckle pattern is easy, as the previous pattern can simply be rinsed off with cold water. This is not expected to affect the specimen, as the temperature was well below the gelling temperature of agarose, and the duration of the cold water rinse was limited (on the order of several seconds). It was found that while the direct application of dry powder was also a feasible speckle method, it was harder to control than when deposited as a suspension.

In order to obtain a good image contrast for DIC, the white speckles required a black background, rather than the transparent agarose gel. In order to do this, 0.1 wt% lampblack was added to the agarose gel during mixing. This lampblack was obtained from Inoxia Ltd[3] and took the form of carbon particles with a maximum size of 30 µm and average particle size of 25 nm. The manufacturer recommended the addition of a small quantity of isopropanol in order to break the surface tension on the carbon black and allow it to fully mix. Instead, a small amount of distilled water was added to the agarose and lampblack, this was vigorously stirred until homogenised, and then the rest of the water was added and heat was applied. This method resulted in significantly greater shear forces when mixing, and allowed the lampblack to be evenly distributed.

Adding this small amount of lampblack did not make the specimen opaque, but did increase light absorption sufficiently to allow for good DIC images to be taken. This can be seen in fig. 4b, where a 1 mm thick agarose sheet on a PMMA



(a) Image of speckled surface. Note relative inhomogeneity of the speckle size, which could be improved. Image cutout is approximately 3 mm x 3 mm in size



(b) Image of 1 mm thick agarose sheet, held against fluorescent ceiling light. Note substantial light transmission due to relatively low loading of carbon black particles. Apparent blurriness is due to light scattering in the agarose sheet, rather than camera focus

Figure 4: Specimen with speckle pattern applied (a) and image showing translucency of specimen (b). Note that both images are of the same material, but fig. 4a appears to have a black background due to the thickness of the specimen and lack of backlighting

[2]As a liquid, the only real mechanical stiffness of the paint was due to viscosity, however this viscosity had to be low simply due to the paint having to pass through the airbrush and atomise efficiently

[3]https://www.inoxia.co.uk/products/chemicals/elements/lampblack

substrate is held up to a fluorescent ceiling light. In spite of this relatively low light absorption, the background appeared fully black when imaging, as can be seen in fig. 4a.

Low rate tests were performed on specimens with and without the carbon black addition, and no detectable difference in the mechanical properties was measured. It is speculated that such small concentrations of filler have no significant effect on the mechanical properties of the specimens. It is unlikely that the carbon particles undergo any chemical reactions with any of the other ingredients, and the rule of mixtures implies that the addition of the carbon black will increase the modulus of the matrix by approximately 0.06%. Whilst the addition of lampblack was only necessary for the high rate tests, the low rate specimens were prepared with the same amount of lampblack for consistency.

2.2. Apparatus and experimental procedure

2.2.1. Low rate Rheometry

The low rate tests were conducted on an Anton Paar MCR Physica 301 Rheometer, with 25 mm diameter platens. Each platen had 2000 grit sandpaper bonded to the surface, in order to delay the onset of slippage. At high frequencies slippage still occurred, but this was obvious from the shape of the modulus plot[4].

Each agarose specimen was tested at 5 and 20 °C, at frequencies from 1 to 100 Hz and at strain amplitudes from 0.1 to 1%. Modulus measurements at the top end of the frequency range were not expected to be reliable (particularly at larger strain amplitudes) due to slipping, however this not an issue as the unreliable data-points were obvious from the modulus vs frequency plot.

[4]A rapid drop in storage modulus with increasing frequency combined with an increase in measured tangent modulus is often indicative of slippage. Repeating the test with a smaller strain amplitude and/or a larger normal force should cause the apparent slipping to occur at a higher frequency – if this is the case, then the phenomenon likely is slipping of the rheometer head rather than any fundamental material property

2.2.2. High rate testing

High rate tests were conducted on the custom apparatus as described in [19]. Specimens were prepared individually, cured, and then speckled before being tested.

Loading was conducted via the use of a novel apparatus as described in [19], with the sinusoidal torsional loading transmitted into the 3D printed strain relief, which then transmitted up into the specimen. Loading was conducted at discrete frequencies, and was conducted for a period of time before data were acquired in order to ensure that the loading was closer to that of a pure frequency, with the transient frequency components due to the sudden imposition of the loading given time (approximately 30-60 seconds) to decay fully.

Imaging was conducted using a Photron FASTCAM SA-X2 1080K-M4 high speed camera with a 200 mm lens. Light was provided by 4 custom LED lights in order to obtain sufficient light for high rate imaging. In order to avoid specular reflections from the smooth surface of the specimen, the lights were polarised at 90°, with a polarising filter at 0° on the camera lens. This filtered specular reflections (which preserve polarisation), but allowed half of the diffuse reflections through, as diffuse reflections randomise polarisation.

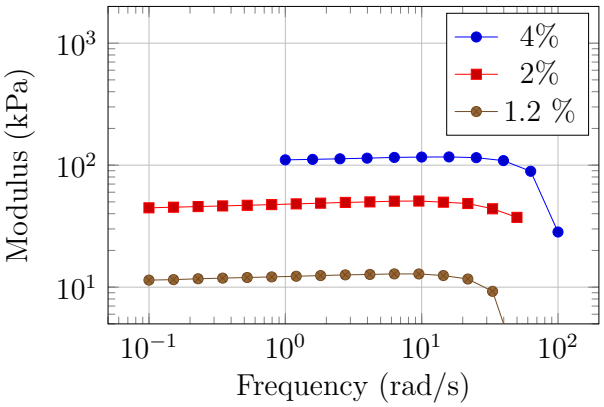
In order to avoid heating of the specimen from the high power lights, the lights were only turned on for periods of approximately 5 seconds during each test. It is unlikely that the specimen heating due to the lights was significant, given the high heat capacity of agarose gel and brain tissue, relatively large volume of the specimen, and the limited duration of the lighting.

2.3. Analysis

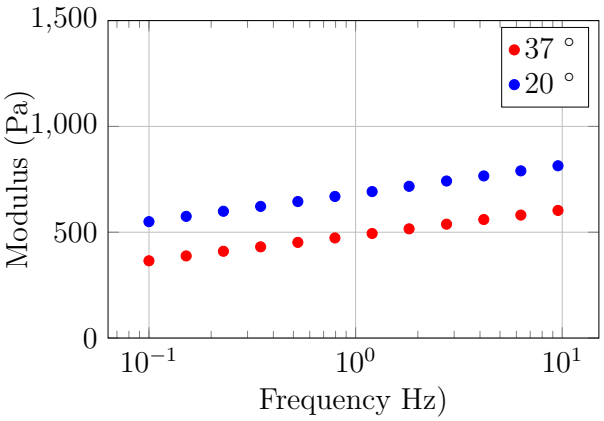
MatchID DIC software was used to convert the images to full-field spatial data. The strain and displacement fields for each image were extracted directly from the DIC software, and post-processed using custom Python code. This data was then transformed into the frequency domain, and the acceleration terms calculated. From this the VFM could be used to calculate the viscoelastic modulus at each spatial point, resulting

in a full-field map of the modulus at a given frequency. For further detail the reader is referred to [19], where the procedure is described in greater detail.

Due to the presence of harmonics, it was often possible to extract data for multiple frequencies from a single experiment – for example, when loading the specimen at 100 Hz, harmonics at 200 and 300 Hz were present. This was only possible for some experiments, as the magnitude of the harmonics was low, and sometimes at the limits of the available strain and/or acceleration resolution.



(a) Complex shear modulus of agarose gel at low rates, for varying concentrations.



(b) Complex shear modulus of porcine brain at low rates, at 20 °and 37 °C

Figure 5: Low rate complex modulus for agarose gel at varying concentrations, and brain tissue at varying temperature. Note the spurious apparent drop in modulus at high frequencies, when slipping occurs. Slipping is delayed for stiffer samples, as the contact forces are higher.

3. Results

3.1. Low rate

Low rate tests results for both agarose and brain tissue are shown in fig. 5. Figure 5a shows the complex modulus vs frequency for agarose gel of varying concentrations, and fig. 5b shows the same but for brain tissue at 20 and 37 °C. Note that frequencies up to 100 Hz are shown for the agarose gel, however slipping occurs before that point and is obvious from the spurious drop in complex modulus.

These data are in agreement with the low rate shear data shown in the literature, indicating that the experimental methodology is valid and that

the test specimens are representative of typical porcine brain tissue.

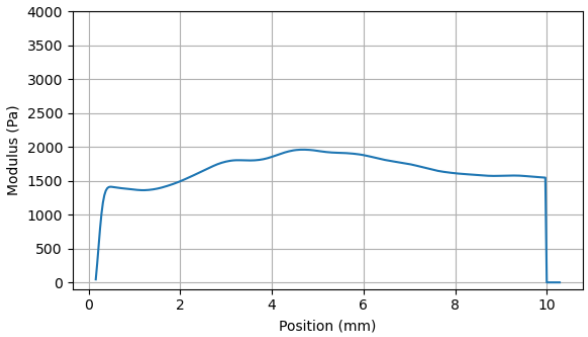


Figure 6: Full field complex modulus for brain tissue at 600 Hz

3.2. High rate

3.2.1. Brain tissue

High rate testing was conducted on brain tissue, with the specimen preparation and experimental method as described in section 2. Figure 6 shows an example of the measured full-field complex modulus of brain tissue at an excitation frequency of 600 Hz. Note that the modulus is not constant, likely due to the inherent inhomogeneity of the sample – see fig. 2 for an example of a specimen with clear minor inhomogeneity. Each specimen contains both grey and white matter, so it is expected that the modulus in the sections consisting primarily of white matter will be higher. This data was then spatially averaged to provide a single complex modulus value for each test, and combined with the low rate data into a single plot to provide a frequency dependant complex modulus over a large range of frequencies as shown in fig. 7. It should be noted that the temperature dependance of the modulus appears to be stronger for low rate data than for high rate data. It is not clear why this is the case, and further testing is needed before the cause can be assigned to either a real effect or an experimental artefact.

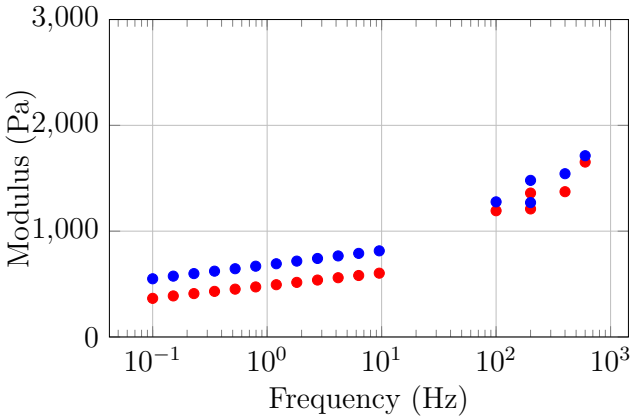


Figure 7: Complex modulus vs freq for porcine brain over a range of frequencies at 20 and 37 °C

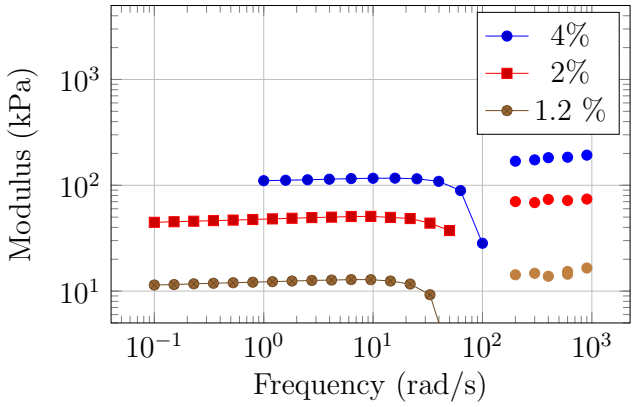


Figure 8: Modulus vs freq for various agarose concentrations at low and high rates

3.2.2. Agarose gel

High rate shear testing was conducted on agarose gel specimens, and each resulting full-field complex modulus spatially averaged in order to give a single datapoint. These datapoints were then combined with the low rate data to generate an extended plot of the frequency dependant complex modulus, shown in fig. 8. These data line up with the low rate data obtained from rheometry, with the exception of the data for 1.2wt% agarose, which appears to be slightly stiffer than expected. This is likely due to the high rate testing having a slightly higher strain amplitude than the low rate testing – softer materials would be more susceptible to this, as the high rate apparatus is displacement controlled rather than strain controlled; strain amplitude is controlled indirectly, and is a result of wave-speed, modulus, and displacement amplitude.

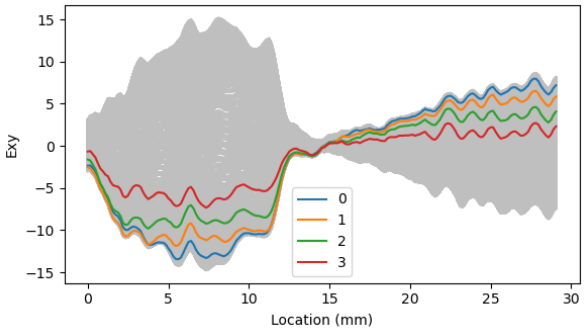


Figure 9: Spatial distribution of strain for all timesteps (plotted as grey lines) and 4 individual timesteps each 5 frames apart. Strains in millistrain. Note the clear and obvious transition between the two concentrations of agarose. When taking the temporal Fourier transform of this data, the distribution shown in fig. 11 is the result.

3.2.3. Deliberately heterogeneous sample

In order to fully validate the ability of the methodology to obtain full-field data on heterogeneous specimens, a deliberately heterogeneous specimen was cast. The mould was only half-filled with high concentration agarose, this agarose was allowed to fully gel and cool, and then the rest of the mould was filled with low concentration agarose. This specimen was then tested the same way as any other specimen, however the measured modulus clearly showed the change in stiffness. In addition to the measured moduli for a deliberately heterogeneous specimen, this section shows the full-field displacement and strain fields in both the temporal and frequency domain in order to give the reader a better understanding of the underlying data.

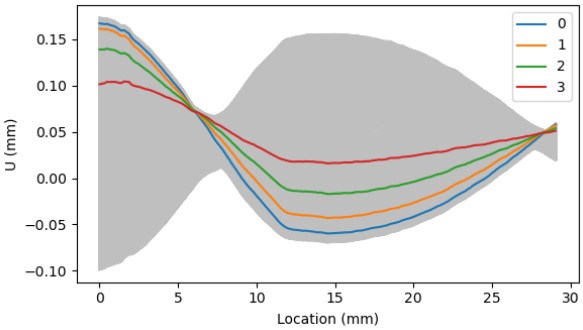


Figure 10: Displacement vs location for all timesteps (plotted as grey lines) and 4 individual timesteps each 5 frames apart. Taking the temporal FFT this data and multiplying by the square of the frequency gives the acceleration data shown in fig. 11

Figures 9 and 10 show the full field spatial distribution of the strain and displacement in the temporal domain. This same data is then shown in the frequency domain in fig. 11. The change in material is obvious even at first glance, where the fields experience a dramatic change at approximately 12 mm. Note the presence of substantial harmonics, in spite of the loading nominally being at a single frequency. Due to the short specimens and relatively low viscosity of the material, there are clearly substantial wave reflections occurring. This does not affect the quality of the analysis, but does make the acceleration and strain fields slightly less intuitive to look at. It should be noted that the 0 mm position is in image co-ordinates, and refers to the top of the image. In reality, the specimen extends slightly past this, as can be inferred by the non-zero strain components at $x = 0$ mm in fig. 11. The full-field complex modulus for a deliberately heterogeneous specimen is shown in fig. 12, where the change in modulus is obvious.

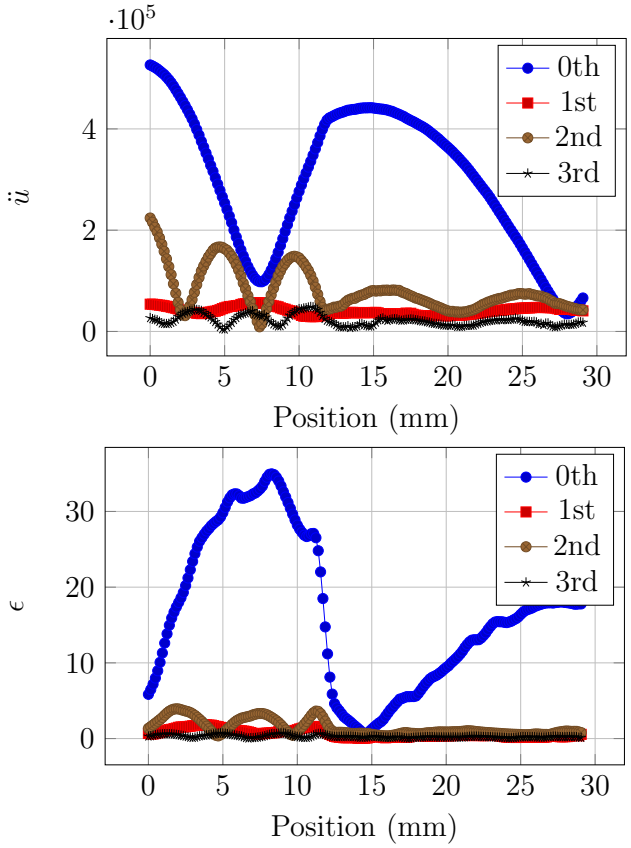


Figure 11: Example of acceleration (top image) and strain (bottom image) harmonics in a specimen. Data is from the same test as shown in figs. 9 and 10. The FFT was not normalised, so only the relative magnitudes matter, not the absolute magnitudes/units. Note the obvious change in modulus at approximately 12 mm. In reality the strain gradient is likely to be steeper than shown, as DIC acts as a low-pass spatial filter.

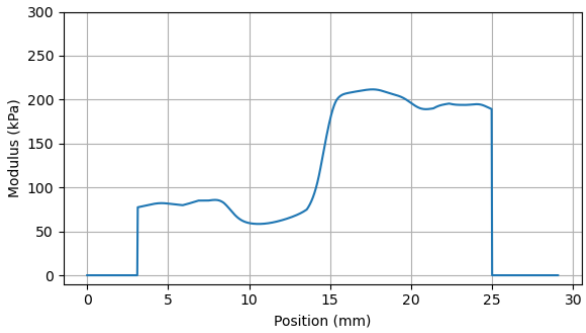


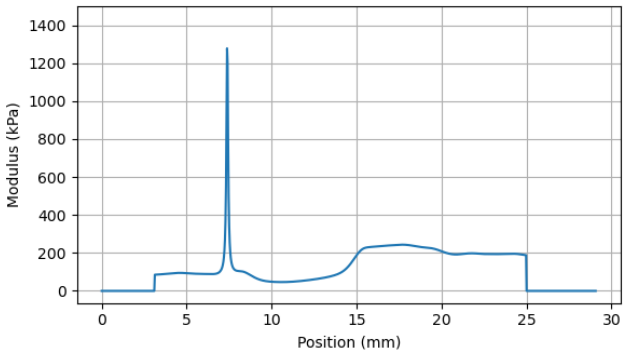
Figure 12: Full-Field complex modulus for 2-part agarose specimen

3.2.4. Damaged specimen

Section 3.2.4 shows and example of a specimen with surface damage to it. This damage clearly causes localised reduction in the quality of the speckle pattern, and possible localised changes in modulus. A further advantage of full-field characterisation is that the damage is clearly visible in the resulting full-field moduli. Unlike in traditional tests which require avearging of the material properties and assumption of homogeneity, here the damage is obvious and the experimentalist can then decide whether to repeat the experiment or even whether to simply exclude the damaged section from the analysis.



(a) Image of damaged speckled specimen. Polariser removed in order to make surface damage more visible



(b) Measured full-field complex modulus vs location for damaged agarose specimen shown in fig. 13a.

Figure 13: Damaged specimen (fig. 13a), and measured full-field modulus (fig. 13b). Note the spurious but obvious spike in modulus at approximately 8mm, corresponding with the location of the damaged speckle pattern (approximately 25% from the top of the specimen image)

4. Conclusions

This set of experiments obtained high rate data on agarose gel and brain tissue that would otherwise be difficult or impossible to obtain. In particular, the use of imaging, a non-contact method for calculating stress, and oscillatory loading overcomes issues associated with the low strength and sound sound speed in these materials. Unlike ultrasonic loading or similar, this set of experiments loaded the material under purely deviatoric deformation, avoiding the confounding effects of inertial loading at high rates. This data on the tunable high rate visco-elastic behaviour of agarose gel is particularly valuable if one is to use agarose gel as a tissue phantom in an application likely to undergo high rate deformation.

The use of full-field characterisation has particular advantages when characterising inhomogeneous materials such as biological tissue. Another advantage of full-field characterisation is the increased robustness of the analysis and measurement, with portions of material damage being isolatable.

References

[1] S. Chatelin, A. Constantinesco, R. Willinger, Fifty years of brain tissue mechanical testing: from in vitro to in vivo investigations., Biorheology 47 (5-6) (2010) 255–76. doi:10.3233/BIR-2010-0576.

[2] S. Chatelin, J. Vappou, S. Roth, J. Raul, R. Willinger, Towards child versus adult brain mechanical properties, Journal of the Mechanical Behavior of Biomedical Materials 6 (2012) 166–173. doi:10.1016/J.JMBBM.2011.09.013.

[3] G. Franceschini, D. Bigoni, P. Regitnig, G. Holzapfel, Brain tissue deforms similarly to filled elastomers and follows consolidation theory, Journal of the Mechanics and Physics of Solids 54 (12) (2006) 2592–2620. doi:10.1016/J.JMPS.2006.05.004.

[4] S. Budday, G. Sommer, C. Birkl, C. Langkammer, J. Haybaeck, J. Kohnert, M. Bauer, F. Paulsen, P. Steinmann, E. Kuhl, G. Holzapfel, Mechanical characterization of human brain tissue, Acta Biomaterialia 48 (2017) 319–340. doi:10.1016/J.ACTBIO.2016.10.036.

[5] S. Budday, R. Nay, R. de Rooij, P. Steinmann, T. Wyrobek, T. C. Ovaert, E. Kuhl, Mechanical properties of gray and white matter brain tissue by indentation, Journal of the Mechanical Behavior of Biomedical Materials 46 (2015) 318–330. doi:10.1016/J.JMBBM.2015.02.024.

[6] S. Budday, T. C. Ovaert, G. A. Holzapfel, P. Steinmann, E. Kuhl, Fifty Shades of Brain: A Review on the Mechanical Testing and Modeling of Brain Tissue, Archives of Computational Methods in Engineering (2019) 1–44doi:10.1007/s11831-019-09352-w.

[7] L. A. Mihai, L. Chin, P. A. Janmey, A. Goriely, A comparison of hyperelastic constitutive models applicable to brain and fat tissues, Journal of The Royal Society Interface 12 (110) (2015) 20150486. doi:10.1098/rsif.2015.0486.

[8] D. F. Moore, A. Jérusalem, M. Nyein, L. Noels, M. S. Jaffee, R. A. Radovitzky, Computational biology — Modeling of primary blast effects on the central nervous system, NeuroImage 47 (2009) T10–T20. doi:10.1016/J.NEUROIMAGE.2009.02.019.

[9] C. Kayal, E. Moeendarbary, R. J. Shipley, J. B. Phillips, Mechanical Response of Neural Cells to Physiologically Relevant Stiffness Gradients, Advanced Healthcare Materials 9 (8) (2020). doi:10.1002/adhm.201901036.

[10] A. E. Forte, Brain Tissue Biomechanics : New Tissue Phantoms , Mechanical Characterisation and Modelling Strategies for Enhanced Surgical (November) (2015).

[11] L. M. Solamen, S. W. Gordon-Wylie, M. D. McGarry, J. B. Weaver, K. D. Paulsen, Phantom evaluations of low frequency MR elastography, Physics in Medicine and Biology 64 (6) (2019). doi:10.1088/1361-6560/ab0290.

[12] M. A. Kandadai, J. L. Raymond, G. J. Shaw, Comparison of electrical conductivities of various brain phantom gels: Developing a 'brain gel model', Materials Science and Engineering: C 32 (8) (2012) 2664–2667. doi:10.1016/J.MSEC.2012.07.024.

[13] Q. Chen, G. A. Thouas, Metallic implant biomaterials, Materials Science and Engineering: R: Reports 87 (2015) 1–57. doi:10.1016/J.MSER.2014.10.001.

[14] P. Zarrintaj, S. Manouchehri, Z. Ahmadi, M. R. Saeb, A. M. Urbanska, D. L. Kaplan, M. Mozafari, Agarose-based biomaterials for tissue engineering, Carbohydrate Polymers 187 (December 2017) (2018) 66–84. doi:10.1016/j.carbpol.2018.01.060.

[15] F. Pierron, M. Grédiac, The Virtual Fields Method, Springer New York, New York, NY, 2012. doi:10.1007/978-1-4614-1824-5.

[16] S. Avril, M. Bonnet, A.-S. Bretelle, M. Grédiac, F. Hild, P. Ienny, F. Latourte, D. Lemosse, S. Pagano, E. Pagnacco, F. Pierron, Overview of Identification Methods of Mechanical Parameters Based on Full-field Measurements, Experimental Mechanics 48 (4) (2008) 381–402. doi:10.1007/s11340-008-9148-y.

[17] G. Lionello, C. Sirieix, M. Baleani, An effective procedure to create a speckle pattern on biological soft tissue for digital image correlation measurements, Journal of the Mechanical Behavior of Biomedical Materials 39 (2014) 1–8. doi:10.1016/j.jmbbm.2014.07.007.

[18] P. Zhou, Subpixel displacement and deformation gradient measurement using digital image/speckle correlation (DISC), Optical Engineering 40 (8) (2001) 1613. doi:10.1117/1.1387992.

[19] A. Graham, C. Siviour, Characterising the frequency-response of ultra-soft polymers with the virtual fields method, Strain 57 (5) (2021) e12386.

[20] A. Goriely, M. G. D. Geers, G. A. Holzapfel, J. Jayamohan, A. Jérusalem, S. Sivaloganathan, W. Squier, J. A. W. van Dommelen, S. Waters, E. Kuhl, Mechanics of the brain: perspectives, challenges, and opportunities, Biomechanics and Modeling in Mechanobiology 14 (5) (2015) 931–965. doi:10.1007/s10237-015-0662-4.

Statement of Authorship for joint/multi-authored papers for PGR thesis

To appear at the end of each thesis chapter submitted as an article/paper

The statement shall describe the candidate's and co-authors' independent research contributions in the thesis publications. For each publication there should exist a complete statement that is to be filled out and signed by the candidate and supervisor **(only required where there isn't already a statement of contribution within the paper itself).**

Title of Paper	Dynamic response of brain tissue and agarose gel
Publication Status	□Published □ Accepted for Publication □Submitted for Publication ■Unpublished and unsubmitted work written in a manuscript style
Publication Details	

Student Confirmation

Student Name:	Aaron Graham		
Contribution to the Paper	Design of experiments, specimen preparation and sourcing, conducted experiments and analysis on samples, interpreted data, wrote manuscript		
Signature		Date	05-04-2024

Supervisor Confirmation

By signing the Statement of Authorship, you are certifying that the candidate made a substantial contribution to the publication, and that the description described above is accurate.

Supervisor name and title: Professor Clive Siviour		
Supervisor comments The statement above is correct.		
Signature 	Date	06/03/2024

This completed form should be included in the thesis, at the end of the relevant chapter.

7

Application of the T-test and Virtual Fields Method to the Constitutive Response of Materials

This chapter reports on the use of the VFM for efficient parameter extraction for an engineering polymer. Unlike the rest of the experiments in this thesis, the tests in this chapter are conducted at quasi-static rates, on high modulus materials (polycarbonate and aluminium).

Using a non-standard test geometry optimised for the testing of ductile polymers, a wide range of stress states are tested in a single experiment. In combination with the VFM's ability to efficiently separate out geometric and material effects, this allowed for the efficient extraction of parameters. Using only a simple material model, the experimental results were matched to a high degree of accuracy with the fitted parameters.

Application of the T-test and Virtual Fields Method to the Constitutive Response of Materials

Aaron Graham[1*], Peihao Song[12], Clive R Siviour[1]

[1]*Department of Engineering Science, University of Oxford, UK*

[2]DPI, P.O. Box 902, 5600 AX Eindhoven, the Netherlands

Abstract

Conventional methods for characterising the constitutive response of materials, such as uniaxial tensile tests, allow simple experiments, but fail to take advantage of the rich information available from modern metrological methodologies such as digital image correlation (DIC). Additionally, they struggle to accurately characterise underlying material response when instabilities and geometric non-linearities such as necking are present in the experiment. The objective of this paper is to investigate the use of DIC and the Virtual Fields Method (VFM) in conjunction with a new specimen geometry to characterise material behaviour efficiently and accurately. Specimens are used with both a traditional tensile test geometry and the new T geometry, with the latter developing a heterogeneous stress field. Due to the ability to take the geometric and material response into account, complex experimental behaviour could be modelled using a simple bilinear material model, with only a small number of parameters. The T geometry allowed data to be obtained from a wide range of stress states in a single experiment. The experimental and analytical methods described in this paper are capable of efficiently obtaining results that would be difficult or impossible to obtain using traditional testing methodologies.

Keywords: Digital Image Correlation, Mechanical characterisation, Virtual Fields Method, Polymer testing

1. Introduction

Despite advances in experimental measurement methodologies that give full-field displacement information, most material characterisation exper-

*Corresponding author

Email address: Aaron.Graham@eng.ox.ac.uk

(Aaron Graham)

Preprint submitted to IJMS

iments currently make use of traditional testing and analysis techniques such as the (nominally) 1D tensile test [1, 2]. Whilst the use of these techniques makes for simple experiments, it wastes the wealth of information available and gives far fewer material parameters per test than needed for most contitutive models. Additionally, traditional measurement and analysis techniques consider only the total specimen response [3, 4]. In reality, this response is made up of a combination of the material properties and the geometric behaviour. Separating the two effects can be difficult, however. Geometric non-linearities and inhomogeneities are present in almost all tests, with necking being a good example: whilst the Cauchy stress in the necked section increases, the cross sectional area decreases, leading to an apparent softening of the material [5]. Additionally, the nominal strain rate in a tensile specimen is often far from homogeneous after the onset of necking, making it challenging to characterise the strain rate dependant material properties [5].

The use of full-field displacement measurements such as Digital Image Correlation (DIC) allow for the direct measurement of the surface strains, in turn allowing heterogeneous strain states to be taken into account [6].

Combining an experimental setup such as a traditional tensile test with DIC and advanced analysis such as the Virtual Fields Method (VFM) can lead to significantly improved analytical results [7]. Material characterisation can then be further improved by combining the VFM and DIC analysis method with a deliberately heterogeneous test geometry such that a wide range of stress states is generated [1]. This leads to more complex test setups that are harder to model and analyse, but provide significantly more information per test.

In this work standard tensile tests were conducted on two materials, with full field DIC and VFM measurement and analysis used to characterise the material response. Similar tests were then conducted on T shaped specimens, using the same analysis technique, allowing for a large variety of stress states to be characterised in a single test.

2. Experimental design

2.1. Material selection and preparation

Two materials were used: 1000 series Aluminium (Al) and Black Polycarbonate[1] (PC). Both the Al and the PC samples are nominally isotropic and homogeneous. At room temperature both materials exhibit significant post-yield ductility, and similar yield strengths, in spite of being

[1] see section 2.1.2 for more detail

fundamentally different materials. Both materials were obtained in the form of sheets, and specimens were cut from them using a CNC mill.

2.1.1. Aluminium

1000 series aluminium was obtained in the form of 3mm sheet, and used in the as supplied material condition with no heat treatment. This material was chosen as it exhibited significant ductility, but a low yield strength. Whilst the density and modulus are higher than that of the PC, yield strength and ductility are similar. This resulted in similar peak forces in the experiments, and allowed for the use of the same experimental apparatus and protocol for both materials.

The primary purpose of testing this material was to aid the validation and commissioning of the technique. Unlike PC, 1000 series aluminium is easy to test, exhibiting minimal temperature and rate dependence. Additionally, 1000 series aluminium is a well understood material, with large amounts of data available in the literature. As a result, the material parameters extracted from this set of tests can be usefully compared to results found in the literature.

2.1.2. Black Polycarbonate

This material (referred to as LEXAN™ copolymer EXL1414 by the manufacturer) consists of a polycarbonate containing 6 wt % polydimethylsiloxane (Mw = 23 kDa), resulting in a polycarbonate material with significant ductility and tolerance to low temperatures. The material was supplied by Sabic in 3 mm thick sheets. Each sheet was then annealed in order to ensure that all specimens had the same thermal history, and were free of residual stresses. Whilst this material is isotropic and homogeneous, it is highly rate and temperature sensitive, and appears to show complex plastic behaviour in tensile tests. It is not clear how much of that complexity is intrinsic to material effects and how much is due to geometric effects, however, making this material an ideal test case for the use of the virtual fields method in parameter determination.

2.2. DIC setup

The DIC setup was the same for both materials and for both the tensile and the T tests. The specimens were prepared by lightly sanding the surface with 2500 grit sandpaper by hand using the standard method, followed by thorough cleaning with soapy water. Next, a base coat of matte black paint was applied, followed by a matte white speckle pattern using an airbrush as in [7]. Matte paint was used in order to minimise spectral reflections. The light source was linearly polarised at 90°, and a linear polarising filter at 0° was placed on the camera lens. This greatly re-

duced specular reflections, improving the quality of the DIC measurements. Whilst the underlying PC was black, it was found that the application of a matte black paint layer improved the DIC image quality.

The camera and DIC parameters for the tests are shown in table 1.

Parameter	**Value**
Camera	Pointgrey GS3-U3-41C6M-C
Image Resolution	2048x2048, 16 bit
Frame Rate	5 fps
Lens	Nikon 60mm lens
Pixel to mm conversion	1px = 0.026 mm
Speckle size	3.8 px
DIC Software	MatchID v2021.2.2
prefiltering	Gaussian, 5x5 px
Subset size	25x25px
Step size	5px
Correlation criterion	ZNSSD
Subset shape function	Irregular quadrangle
Interpolation:	Bicubic spline
Strain Window:	13x13
Strain interpolation	Q8
Strain tensor	Green-Lagrange

Table 1: Table of DIC and imaging parameters

2.3. Tensile tests

Tensile test specimens were prepared according to the ASTM standard for tensile testing of polymers (ISO-527-Type1BA) and the ASTM standard for tensile testing of metals (ASTM E8) respectively. Tests were conducted over 3 decades of strain rate in order to obtain rate dependant quasi-static properties. Full-field strain measurements were conducted for each tensile test, using DIC and the Virtual Fields Method (VFM). Tensile tests have the advantage of being well understood, simple, and easy to conduct and analyse, however they have the disadvantage of providing data over a very small range of stress states and strain rates for each test.

2.4. Short bend test

In order to obtain data over a wider range of stress states in a single test, a modified 3pt bend experiment was conducted. Unlike a standard 3pt bend test, this geometry had a small aspect ratio. This allowed for significant heterogeneity in the stress states in the specimen. Uniaxial tension and compression were experienced in the bottom and top faces of the beam, whilst the neutral axis experienced pure shear. This results in a test that gives a significantly greater range of stress states than a uniaxial test, but without the need for complex geometries. Only one test was conducted on the black PC material, as the T tests superseded the utility of the short beam bend tests. The test setup is shown in fig. 1, along with specimen dimensions.

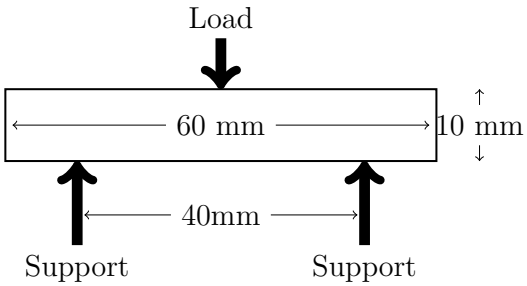


Figure 1: 1:1 scale schematic of the modified beam bend test. Beam thickness was 2mm, height was 10mm, total length was 60mm, and span was 40mm

2.5. T tests

The T test specimen geometry is set up as an inverted T section, with the ends of the arms clamped and the vertical section loaded in tension, fig. 2. As a result, it is possible to achieve a wide range of complex stress states from a single experiment. This is effectively a combination of a uniaxial tension test and the short beam bend test described above. The following plane stress states are achieved in the specimen, as well as various combinations thereof:

1. Uniaxial vertical tension
2. Biaxial tension
3. Uniaxial horizontal compression
4. Uniaxial horizontal tension
5. Pure shear
6. Pure (-ve) shear
7. Stress free

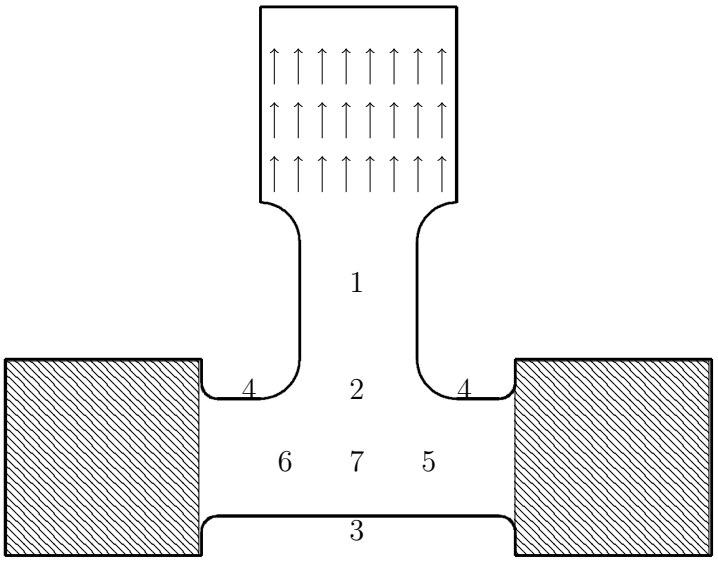


Figure 2: Scale diagram of the T specimen. Hatched lateral tabs are fixed in place using a custom grip, and so have a zero displacement boundary condition. The upper tab is displaced at a constant rate using the Instron apparatus, and the force is recorded. The analysed section of the specimen is away from the tabs, consisting only of an inverted T.

In reality, the stress state is a continuously variable quantity, smoothly changing from one region to the next. As a result of the above stress distribution, it is possible to characterise a material over a wide range of stress states in a single test, rather than the multiple tests that would be required by traditional methods. For full dimensions of the T specimen and associated clamp, please see Appendix A and Appendix B.

2.6. DIC vs VFM considerations

The VFM is capable of obtaining a large number of model parameters from a single experiment; however, in order to achieve this the the stress field should be highly heterogeneous, and as many

stress states as possible represented.

Whilst the VFM works well when the stress state is heterogeneous, DIC is effectively a low pass spatial filter that smooths steep strain gradients. This results in a set of seemingly contradictory requirements for the experimental design: maximising heterogeneity of the stress field, but at the same time minimising strain gradients. For example, a specimen with a large number of small holes and sharp corners would achieve a highly heterogeneous stress state, but it would have high strain gradients and would therefore be poorly suited to accurate measurement with DIC. In this work the T shape shown was found to have a good balance between the need to cover the full 2D stress space and minimisation of strain gradients. Several different T geometries were explored, and the geometry presented was found to have the best balance between ensuring plane stress behaviour and avoiding out-of-plane behaviour such as buckling[2]. The full range of plain stress states is obtained in the elastic region; however, once plasticity develops, tensile stress begins to dominate during the plastic region. This is difficult to avoid, as plane stress plasticity is challenging to obtain without the occurrence of buckling or other out-of-plane behaviours.

[2]The optimal geometry is likely to be different for different materials, and as such some experimentation may be needed before selecting the ideal geometry for testing a material with substantially different properties to the materials tested in this paper.

2.7. VFM analysis

For this set of experiments, a commercial DIC and VFM solver from MatchID was used. For more information on this software, see `https://www.matchid.eu/`.

The material model used was a bi-linear elasto-plastic model with hardening. This model has the advantage of being relatively simple, whilst fitting the behaviour of the material well. The elastic regime stress is given by simple 2d linear elasticity:

$$\begin{aligned}\sigma_{11} &= \frac{E}{(1-\nu^2)}\left(\epsilon_{11}+\nu\epsilon_{22}\right)\\ \sigma_{22} &= \frac{E}{(1-\nu^2)}\left(\epsilon_{22}+\nu\epsilon_{11}\right)\\ \sigma_{12} &= \frac{E}{(1+\nu)}\epsilon_{12}\end{aligned} \tag{1}$$

where E is the elastic modulus and ν is Poisson's ratio. The plastic regime stress is given by:

$$\sigma = Y_0 + H\epsilon_p \tag{2}$$

where Y_0 is the initial yield stress, H is the hardening index and ϵ_p is the plastic strain.

A key limitation of the VFM method as used in this paper is the assumption of plane stress in the specimen. When solving for the stress state, an

assumption of constant thickness[3] plane stress is made. For this reason it is important that tested specimens have a small out-of plane thickness, and that they do not undergo significant out-of-plane displacement or other deformations which would significantly deviate from the plane stress state.

2.8. Simulations

Whilst the tensile test results serve as validation for the technique, the use of FEA simulations can be a valuable tool for experimental design, as well as providing additional validation of the analysis method. To this end, the experimental setup was simulated using Abaqus© FEA software, the imaging was simulated using MatchID's FE-Def module, and the analysis was conducted using the MatchID DIC and VFM software, using the same settings as for the real experiments. This simulation procedure is described in fig. 3

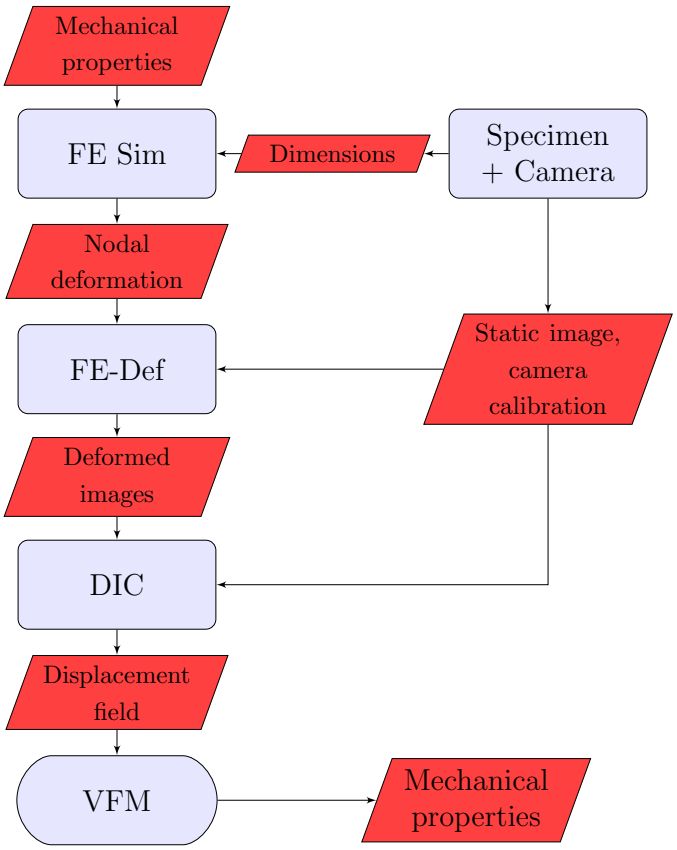


Figure 3: Flowchart showing simulation procedure for test method validation.

Representative mechanical properties used in the FEA simulation were obtained from previous mechanical tests on PC [8], and specimen dimensions and loading rates were the same as those in the experiments. For this set of simulations a linear elasto-plastic model was used, which is the same as will be fit to the experiments later in this paper. This results in force-displacement curves that are slightly different from those obtained in the experiments; however, this allows errors in the VFM methodology to be identified, as the results should otherwise match perfectly with the input model.

A photo of a representative specimen was taken using the same camera as used in the experiments, and the optical parameters such as focal length, field of view, and distance to specimen were characterised. This static image was then fed into the FE-Def module along with the nodal defor-

[3] i.e. that the specimen is of constant thickness at the start of the test

Parameter	Input val	Extracted val
Yield stress (MPa)	100	101.3
Hardening (MPa)	200	219.3

Table 2: Example of input vs output parameters for simulation of experiment

mations from the FE simulation, resulting in artificially deformed images of the experiment which take real-world effects such as lens geometry and camera noise into account. Image noise was then added; this was heteroscedatic, and obtained by comparing several nominally identical images of the specimen obtained using the same camera – any differences were assumed to be due to noise. Adding noise is important, as all cameras contain some inherent noise, which can impact the fidelity of the DIC measurements and hence the experimental results.

2.8.1. Simulation results

The simulation was first performed using representative properties in a bilinear elasto-plastic model. The input parameters are shown in table 2 along with the parameters output by the VFM analysis. For this analysis the initial guess for both the yield stress and the hardening index were chosen to be half of the values input to the simulation, in order to ensure that the analysis is robust to initial guesses that are far from the correct parameters.

The above result showed that the experimental

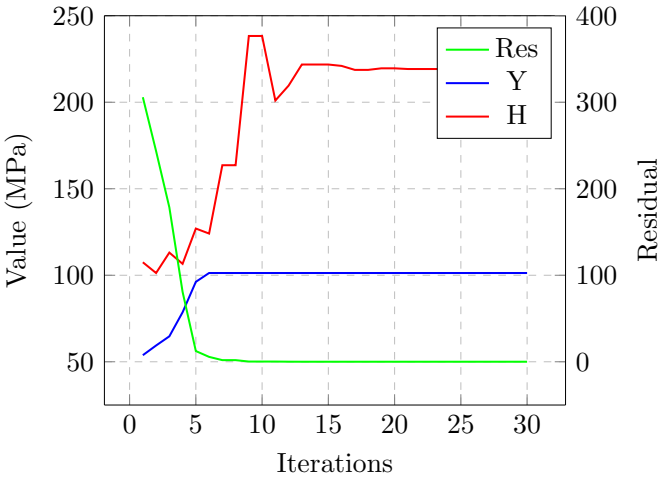


Figure 4: Evolution of the extracted Yield stress and Hardening modulus vs iteration step

method proposed in this paper is well suited to the extraction of properties from an elasto-plastic material. It is unsurprising that the error on the reconstructed yield stress is lower than that of the reconstructed hardening index, as the residual is far more sensitive to the yield stress than to the hardening index. This is shown in fig. 5, where the residual due to a 10% error in the yield stress or the hardening modulus is shown – the residual is significantly more sensitive to the effects of the yield stress.This could be seen from the fact that the yield stress converged within 5-6 steps, whereas the hardening index took a lot longer to converge.

This result is further shown in fig. 6, where a contour plot of the residual vs error in yield stress and hardening index is shown for a material where the strain is 20%. As the amount of strain de-

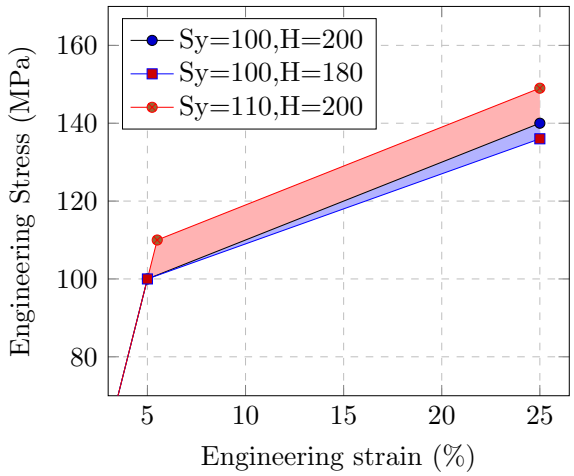
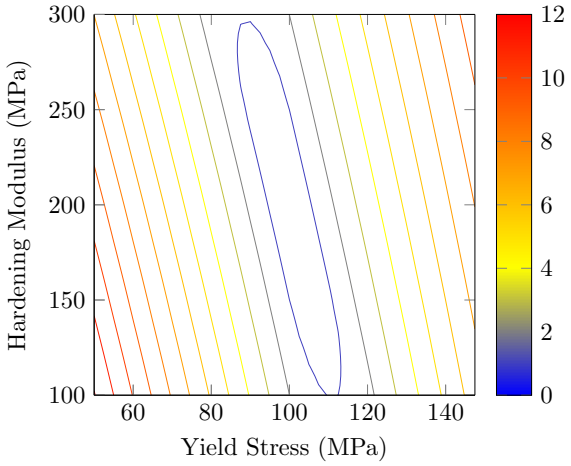


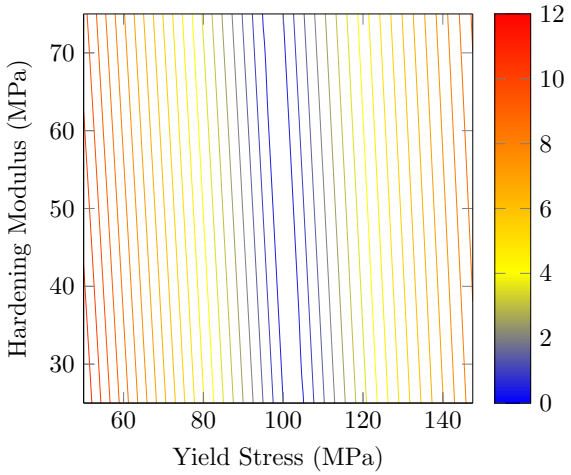
Figure 5: Engineering stress vs strain for a given elasto-plastic material model. Lines in red and blue represent the stress response for a 10% error in the yield stress and hardening modulus respectively. The red and blue areas represent the energy residual as a result of these errors

creases, the sensitivity of the residual to changes in the hardening modulus will further decrease. Note too how the contour plot in fig. 6a is significantly steeper in the direction of the hardening index than fig. 6b, indicating that the sensitivity of the residual to relative changes in the hardening index is significantly greater if the hardening index is already large.

In order to further explore this, the yield stress was kept at 100 MPa and the hardening index reduced to 10 MPa; the methodology struggled to accurately identify the hardening index at all. This is not surprising, as the specimen now displayed minimal ductility and hence very little sensitivity to hardening. Quite apart from the effect shown in fig. 6, a very low hardening modulus leads to a strong localisation of the yield, almost



(a) $S_y = 100$ MPa, $H = 200$ MPa, $\epsilon = 0.25$



(b) $S_y = 100$ MPa, $H = 50$ MPa, $\epsilon = 0.25$

Figure 6: Contour plot of the residual due to errors in the Yield stress and hardening modulus for a strain value of 25%. Note that the gradient of the lines would change as the total strain changes. This plot is for a single infinitesimal portion of material at a uniaxial strain of 25%, in reality an experiment will consist of multiple portions of material with different strain values and residuals

like a brittle failure. As a result of this, there is minimal material that undergoes plasticity, and hence little information from which to calculate the hardening index. This result reinforces that the test setup is best suited to ductile materials if post-yield behaviour is to be modelled.

Test configuration	Displacement rate (mm/min)	Temperature
Alu tensile	1, 10	25 ^{o}C
Alu T	1, 5	25 ^{o}C
PC tensile	1, 10, 100	25 ^{o}C
PC T	0.1, 1, 10, 100	25 ^{o}C

Table 3: Matrix of tests conducted

3. Results and Discussion

An Instron 5980 universal testing machine was used for all experiments. Standard tensile clamps were used for the tensile tests, whilst a simple apparatus was used for the bend test. For the T tests the upper (loaded) grip tab of the T was gripped with the same tensile clamp used for the tensile tests, while the lower (clamped/fixed) grip tabs of the T were gripped using a custom apparatus. The following tests were conducted, as shown in table 3:

3.1. Tensile tests

The force and crosshead displacement for each tensile test were measured using the Instron, and the full field displacement and strain fields were measured using DIC.

Figure 7 shows the engineering stress vs crosshead displacement for the room temperature experiments. Note that the Aluminium appears to show simple elasto-plastic ductile behaviour, whereas the polycarbonate exhibits more complex behaviour. Whilst the net material response of

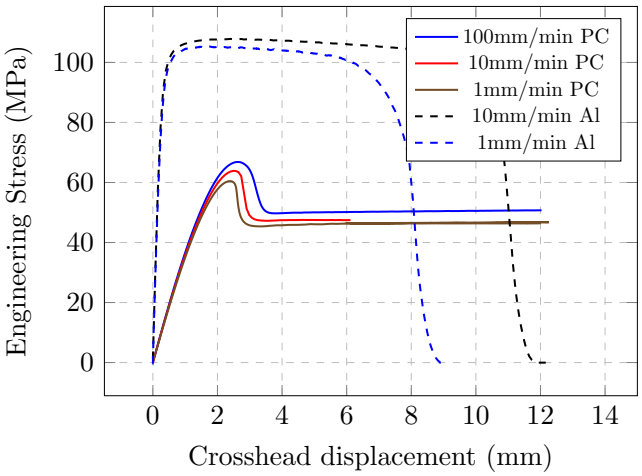


Figure 7: Engineering stress vs crosshead displacement for tests on Al (dashed) and PC (solid) over a range of strain rates at room temperature

the tensile tests was complex, this was largely due to geometric effects. The deformation of the specimen is only uniform until the onset of necking, after which it exhibits substantial heterogeneity. This is shown in fig. 8 for example, where the local tensile strain at a range of locations is plotted against crosshead displacement. Until the onset of necking the strain is clearly homogeneous across the specimen, however this homogeneity disappears at the onset of necking. The necked region experiences a very high strain rate (as seen by the gradient of the first blue line in fig. 8), and the rest of the specimen experiences negative strain rate as the force drops. This necked region then gradually moves along the specimen, as shown by each point experiencing successive necking. Figure 9 shows the full-field ϵ_{YY} strain components for for a selection of times before and

shortly after the initiation and then propagation of the neck in a tensile test of a PC specimen. Point 0 in fig. 8 is at the location of the initial neck shown in fig. 9, with each subsequent point evenly spaced below pt0.

This strain field heterogeneity clearly contributes to the complex behaviour of the tensile test, in particular the apparent strain softening. This reinforces that adequately characterising the material behaviour requires separation of the effects of material and geometric behaviour.

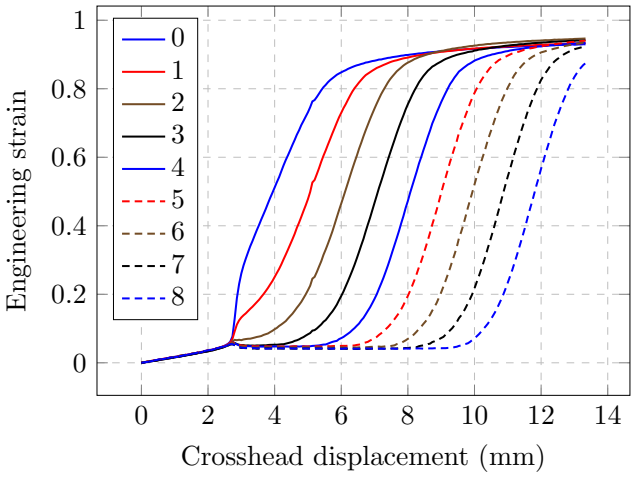


Figure 8: Engineering strain for discrete locations on a PC tensile sample vs crosshead displacement. Point 0 is located at the initial neck location, and each subsequent point is slightly further from the initial neck location. Figure 9 shows colourmaps of the YY strains over the entire specimen for a small portion of the plot shown here

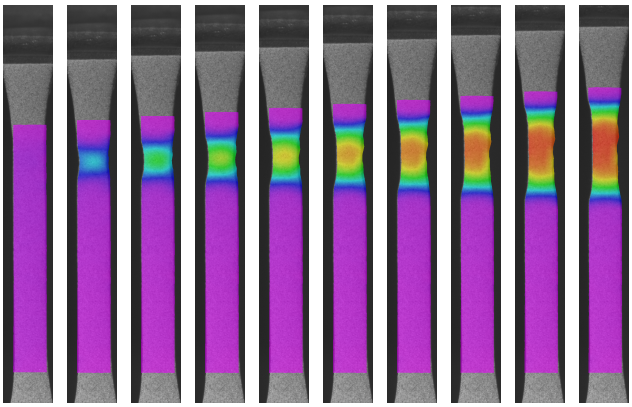


Figure 9: DIC images of the YY direction strain, showing the initiation of the neck followed by expansion of the neck downwards. Images are from the same experiment as the data in fig. 8

3.1.1. VFM fitting

A linear elasto-plastic model with linear hardening was fitted to each tensile test, as described in section 2.7. Needless to say, this material model is not expected to fully capture the complex behaviour of PC. The purpose of this model is instead to see how well a simple model like this can capture complex behaviour, if fitted sufficiently well.

The VFM was then used in MatchID to fit the material parameters to the crosshead force measurement and the full-field DIC strain measurements. This is accomplished by minimising the difference between the external and internal work (work done due to traction forces and internal deformation respectively). This difference is referred to as the residual, and is shown for each set of results alongside the extracted parameters (such as in table 5) An example of this is shown in fig. 10a. Note the surprisingly close match between the internal and external work despite of the use of a simple bilinear material model. The sharp change in the gradient of the internal virtual work at approximately 1.8 mm shows the point where the specimen starts to homogeneously yield, before necking occurs at approximately 2.5 mm and the work drops due to unloading and strain localisation. Note that the drop in force at approximately 2.5 mm is driven primarily by geometric effects, rather than purely due to intrinsic material properties. Separating these effects is extremely challenging using traditional tensile test methods, further showing the utility of the VFM for even a "simple" test such as a traditional quasi-static uniaxial tensile test. The difference between the red and blue lines in fig. 10a are effectively the material non-linearity that is not captured by the linear material model – any non-linearity in the red line is due to geometric rather than material effects.

Whilst the units of fig. 10a are in work vs crosshead displacement, for a 1D tensile test the external work-displacement curve is identical to a scaled engineering stress:strain plot. The internal work refers to the work done by the internal stresses and strains, and should match the external work done.

Figure 10b shows an example of the internal and external work done for a tensile test on Aluminium. The bilinear material model clearly fits well here too, however this is unsurprising given the bilinear nature of the force:displacement curve. The parameters extracted for both Polycarbonate and Aluminium are shown in tables 4 and 5. Note the strong rate dependence shown by the fitted parameters for PC, and the weak rate

dependence shown by the Aluminium.

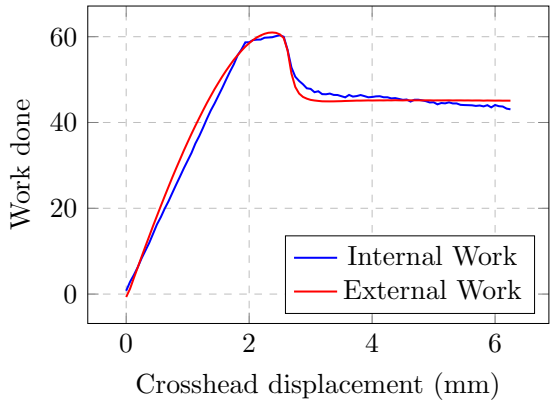
The aluminium provides a validation on a material for which the parameters are straightforward to measure in a tensile test, whilst the PC demonstrates the applicability of the technique to more complex behaviours.

Rate (mmpm)	E_y and cov	ν and cov	S_y	H	Res
10	1822, 0.0086	0.4064, 0.0001	64	35	3.57
1	1810, 0.0059	0.393, 0.0001	56.12	5.85	2.545

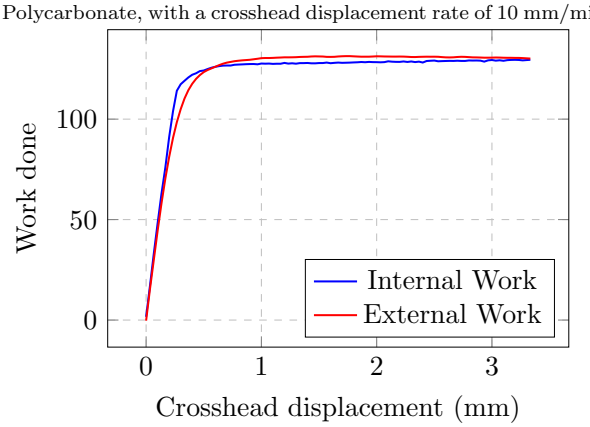
Table 4: Parameters extracted from the VFM analysis of tensile tests on PC

Rate (mmpm)	E_y and cov	ν	S_y	H	Res
1	69700, 0.0059	0.363	114.6	161.9	13.67
10	69700	0.36	121.6	193.3	34.47

Table 5: Parameters extracted by the VFM on tensile tests of Al



(a) Polycarbonate, with a crosshead displacement rate of 10 mm/min



(b) Aluminium, with a crosshead displacement rate of 1 mm/min

Figure 10: External work (due to boundary tractions and displacements) vs internal work (due to material stresses and strains) for a tensile test of Al and PC respectively

3.2. Short beam bend test

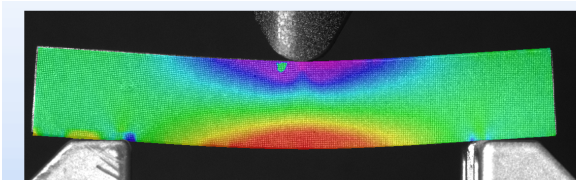
This test was designed as an intermediate between the tensile and the T test; however, only one was performed as the T test was found to better in terms of maximising the range of stress states achieved, as well as minimising the presence of high strain gradients (and hence DIC artefacts). Unlike a traditional beam bend test, the aspect ratio of the beam is low, maximising the amount of shear. This is usually avoided in a traditional bend test, but is an asset for the VFM as it provides additional information for the parameter selection process.

Figure 11 shows the reconstructed stresses for the short beam bend test part way through the test. As can be seen in these images, this test fulfilled the purpose of obtaining a wide range of stress states using only a single test, however there are some critical limitations:

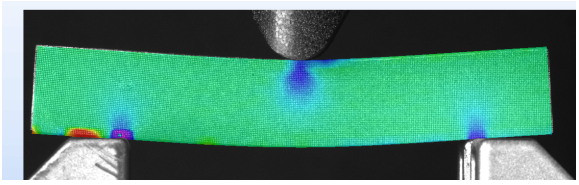
1. Due to the point contact between the specimen and the supports, as well as between the specimen and the indenter, there are high strain gradients in these areas. The DIC measurement process is likely to smooth these high gradients as previously discussed, making this test well suited to the VFM but unfortunately poorly suited to measurement with DIC. Given that the VFM analysis will be relying on measurements extracted via DIC, this is an important limitation.

2. Few regions of the specimen experience significant stresses in the yy direction. This is less of an issue for an isotropic material such as this, but would be a limitation if testing anisotropic materials.

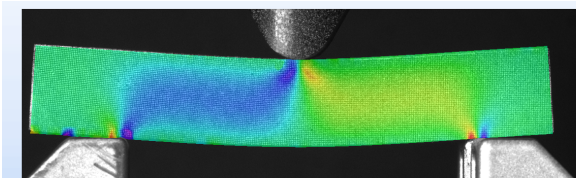
3. When plasticity does occur, it occurs over only a narrow region of the specimen. This is not a critical flaw, particularly if sensitivity based piecewise virtual fields are used, but



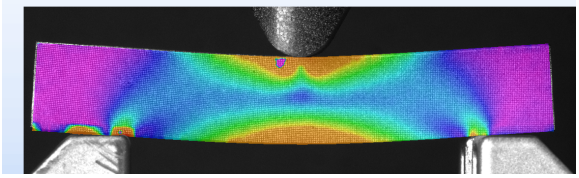
(a) XX stresses



(b) YY stresses



(c) XY stresses



(d) Von Misces stresses

Figure 11: Reconstructed primary and von Mises stresses for the short beam test. Images shown for illustrative purposes, hence lack of detailed colourbars.

it would be better to not have this issue if possible.

Based on the aforementioned flaws, it was decided to move on to the T test, shown in the next subsection. However, the modified bend test benefits from being easy to set up using simple rectangular specimens and standard apparatus. If characterising a simple material for exploratory work, this test is worth conducting before commissioning the apparatus capable of conducting the T test.

3.3. T tests

T tests were conducted at a range of temperatures and strain rates on PC and Al specimens, fitting an elastoplastic model to each test.

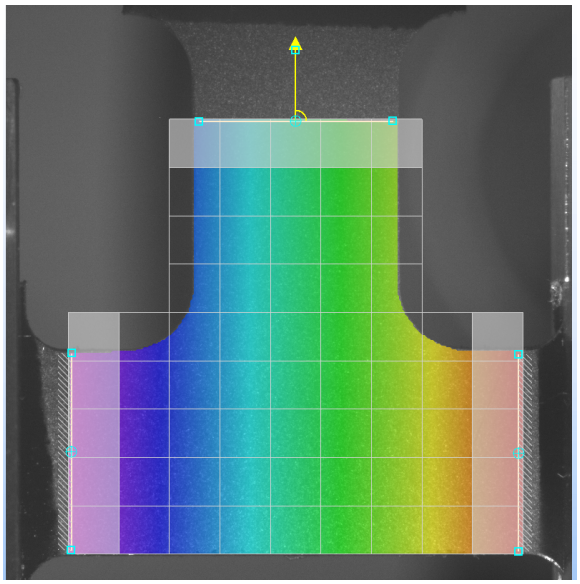


Figure 12: Setup of the T test, with piecewise virtual fields shown

Figure 12 shows an example of the VFM setup for a T test. Note that only the edges of the grips tabs shown in fig. 2 are visible, and that the VFM analysis does not include the very edge sections. The squares show the analysed regions, with each square representing a discretised piecewise virtual field. It is important to note that each virtual field region is in no way equivalent to an element in FEA. Whilst the VFM is in many ways analogous to inverse FEA methods, this is not one of the areas where that analogy holds. It is entirely possible to obtain excellent VFM results using only a single virtual field, however it has been found that the use of piecewise fields can improve sensitivity, particularly if only a small portion of the overall specimen is undergoing the behaviour of interest. For instance, if one is attempting to solve for plasticity parameters and only a small portion of the specimen is undergoing plasticity, the use of optimised piecewise virtual fields can enhance the sensitivity of the analysis.

The various experimental parameters (such as boundary conditions, force, and specimen thickness) are input, as well as the material model to solve and an initial guess for material parameters. The two lateral boundaries are set to be a displacement boundary condition, and the upper boundary is set as a force boundary condition

using the synchronised force measurements taken from the Instron. Additionally, various VFM specific parameters can be chosen, such as the type of virtual field and limitations on the allowable range of solutions for material parameters.

Tables 6 and 7 show the material parameters obtained from the T test data at room temperature.

Rate (mmpm)	E_y (MPa) and cov	ν and cov	S_y (MPa)	H (MPa)	Res
10	2084, 0.0054	0.411, 0.0001	72.75	25.6	2.755
1	2013, 0.0026	0.3862, 0.0001	68.14	28.65	1.184
0.1	1982, 0.0088	0.377, 0.0001	59.63	32	0.5361

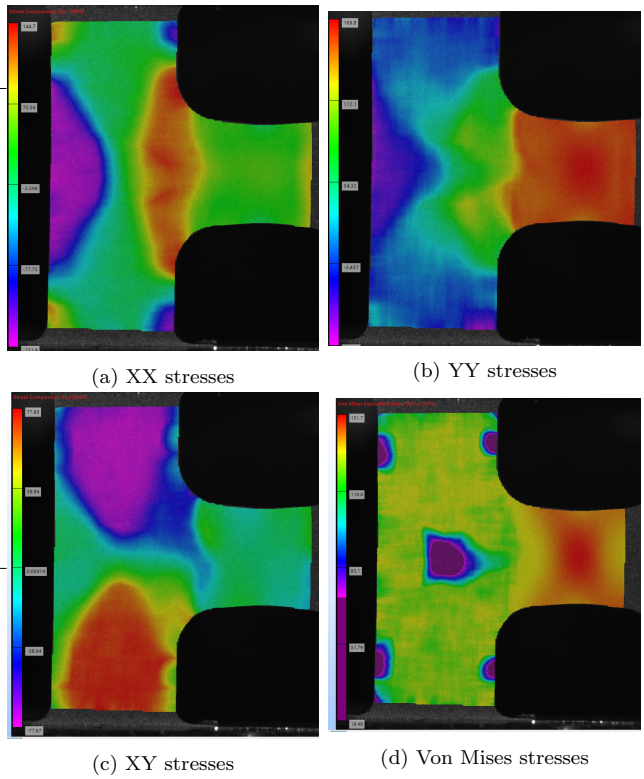
Table 6: Parameters extracted by the VFM from T tests of PC

Rate (mmpm)	E_y (MPa) and cov	ν and cov	S_y (MPa)	H (MPa)	Res
5	68700, 0.0059	0.353, 0.0001	135.6	81.9	6.02

Table 7: Parameters extracted by the VFM from T tests of Al

3.3.1. Stress states achieved

Reconstructed stresses in the specimen for both the Al and the PC T specimens are shown in (fig. 13) and (fig. 14)respectively. The stresses in the PC are shown just prior to the onset of yield, whilst the stresses in the Al are shown later in the test, just prior to fracture of the specimen. When viewing fig. 13d, note the X shaped portion of maximum stress on the upper portion of the T shape. This appears to be a double shear band, which formed just prior to initial yield and then again just prior to fracture. In both instances, the location of the yield initiation and the crack initiation appeared to be at the centre of the X shape.



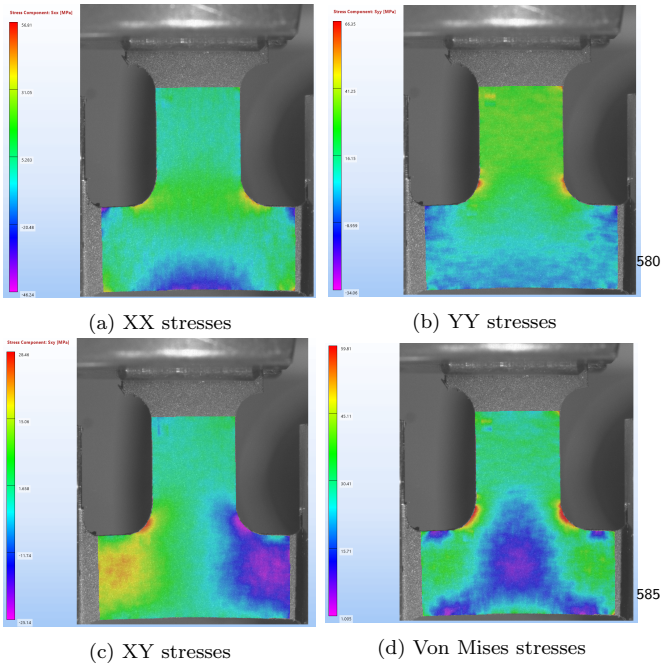
(a) XX stresses (b) YY stresses

(c) XY stresses (d) Von Mises stresses

Figure 13: Reconstructed stresses in the Al T section just prior to fracture

Figures 14a and 14c to 14d shows the reconstructed stress distribution in the PC T section just prior to yield. Note that the rounded corners of the T section undergo a small amount of yielding long before the rest of the specimen ex-

periences plastic deformation; this is due to the effect of stress concentrations. Whilst this did not adversely affect this set of tests, this may cause issues if testing less ductile materials. Note that the compressive stresses at the bottom of the specimen are a substantial percentage of the yield stress, allowing for good characterisation of (elastic) compressive properties as well as tensile properties if needed.

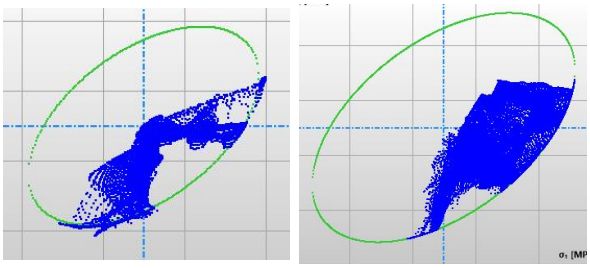


(a) XX stresses (b) YY stresses

(c) XY stresses (d) Von Mises stresses

Figure 14: Reconstructed stresses in the PC T section just prior to the onset of significant plasticity

Unlike the tensile tests or even the beam tests, the T tests achieved a wide variety of stress states. This is shown graphically in figs. 13 and 14 but is also shown below in fig. 15, with xx and yy stresses for each datapoint plotted against each other at a single time.



(a) Beam stresses (b) T section stresses

Figure 15: Range of stress states obtained in the beam and the T test on PC, shortly before the onset of significant plasticity. The green oval represents the von mises yield criterion

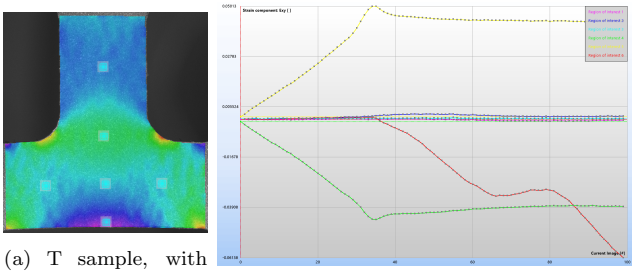
As shown in fig. 15a, the beam test obtains a better distribution of stress states than a tensile test would, but does not cover as much of the stress space as it could. In contrast, fig. 15b shows that the stress state obtained by the T test covers far more of the stress space. Whilst the stresses in the Y axis are primarily tensile, a range of both tensile and compressive stress states are obtained in the X axis.

3.3.2. Change in strain with time

Due to the geometry of the specimen, a range of strain rates is obtained as the specimen progressively deforms under loading. Whilst this range is not large, it is significantly more than would normally be obtained using traditional methods such as tensile tests[4]. For example, when conducting a T test on polycarbonate at a constant crosshead speed, multiple decades of strain rate

[4]However as shown earlier in this paper, even tensile tests with nominally constant strain rates often have a range of local strain rates after the onset of plasticity.

are achieved in the specimen. This can be an advantage if one is using a time-dependant material model, as a range of strain rates can be obtained from a single test.



(a) T sample, with locations of pts for stress extraction

(b) Shear stress vs time for pts shown in fig. 16a

Figure 16: Shear stress evolution vs time for various points on the sample

Figure 16 shows the evolution of the shear stress vs time for 6 points on a T specimen, where pt 6 is at the top, and points 4 and 5 are to the sides. Note that the shear stresses the central points are zero initially, as one would expect. The shear stresses in points 4 and 5 rise linearly as the specimen is loaded elastically, but then peak and drop as the top section begins to yield. At this point the shear stresses in pt 6 start to rise, due to plastic deformation. Whilst these are a limited subsection of the available points that the VFM analyses, already one can see a variety of deformation profiles, including various strain rates as well as relaxation behaviour. This range of behaviour is an asset for the VFM, and will aid in the time dependant characterisation of the material, should a time dependant material model be used.

3.4. Tensile vs T results

Both the tensile tests and the T tests obtained similar moduli, Poisson's ratios, and yield stresses, however there was some disagreement, particularly when it came to the hardening index. Given that the T section effectively had a shorter gauge length than the tensile specimens, it was not expected that the results would match up exactly for a given displacement rate, however the results from the T tests are almost uniformly stiffer than those from the tensile tests. It is expected that the results from the T test are more reliable than the tensile test results, as:

1. The VFM makes the assumption of plane stress, and the T sections were far closer to a 2d sample than the tensile samples. The narrowest portion of the T specimen had a cross-sectional aspect ratio of 15:3, whereas the cross-sectional aspect ratio of the tensile specimens was 5:3 Whilst the tensile samples were cut to the ASTM standard, they were thick in comparison to their width. The importance of this could be tested using artificially deformed images based on FEA simulations, as was done in [9]
2. The residual, a measure of goodness of fit, was far lower (i.e. better) for the T tests

than for the tensile tests. This was unexpected: as the material tested has some time dependence, and the T tests exhibit a wider array of strain rates, it was expected that the tensile tests would fit better, with a lower residual.

4. Conclusions

This methodology is a significant improvement over traditional tensile tests, obtaining better quality, more varied data. The use of the VFM allows for even complex material behaviour to be modelled using a simple material model. Using a simple bilinear elasto-plastic material model, experiments which exhibited complex force:displacement histories were accurately modelled and characterised. The use of the T geometry allows for an experiment that covers a far greater range of stress states and strain-rates than a traditional tensile test, taking advantage of the full-field measurement methods available to the modern researcher. Unlike traditional tensile tests, the T geometry allows for a single experiment to obtain a full range of plane-stress states including compression and biaxial tension. Even when conducting traditional tensile tests using standard specimen geometries, the use of the VFM for analysis can greatly improve the quality of the parameter extraction, as shown by the analysis of the tensile tests on the PC. The VFM's ability to fully exploit the full-field measurement capabilities of DIC allowed for the separation of the total specimen response into material non-linearities and geometric non-linearities such as necking. In this way significantly more information can be extracted from a tensile test than would otherwise be possible, and the apparently complex behaviour can be accurately predicted using only a simple material model once the effect of geometric non-linearities has been taken into account.

Acknowledgements

This research forms part of the research programme of DPI, project 827t19, *Impact Modelling of Polymers: High-rate Experiments for Solid-state Simulations*, and the materials were kindly supported by Saudi Basic Industries Corporation (SABIC). The authors thank the Rhodes Trust for their generous support. The authors thank the technicians of the Solid Mechanics Group workshop, in particular Andy Bateman for his help with the manufacture of specimens and fixtures for this project.

For the purpose of Open Access, the authors have applied a CC BY public copyright license to any Author Accepted Manuscript (AAM) version arising from this submission.

Data Availability

All data supporting this study are openly available from the Oxford University Research Archive at [insert DOI here]. **Note: Data upload is waiting for the DOI to be generated.**

References

[1] F. Pierron, M. Grédiac, The Virtual Fields Method, Springer New York, New York, NY, 2012. URL: http://link.springer.com/10.1007/978-1-4614-1824-5. doi:10.1007/978-1-4614-1824-5.

[2] R. Moulart, F. Pierron, S. R. Hallett, M. R. Wisnom, Full-Field Strain Measurement and Identification of Composites Moduli at High Strain Rate with the Virtual Fields Method, Experimental Mechanics 51 (2011) 509–536.

[3] X. Gu, F. Pierron, Towards the design of a new standard for composite stiffness identification, Composites Part A: Applied Science and Manufacturing 91 (2016) 448–460.

[4] S. H. Yoon, C. R. Siviour, Application of the Virtual Fields Method to Rubbers Under Medium Strain Rate Deformation Using Both Acceleration and Traction Force Data, Journal of Dynamic Behavior of Materials 3 (2017) 12–22.

[5] A. K. Ghosh, Tensile instability and necking in materials with strain hardening and strain-rate hardening, Acta Metallurgica 25 (1977) 1413–1424.

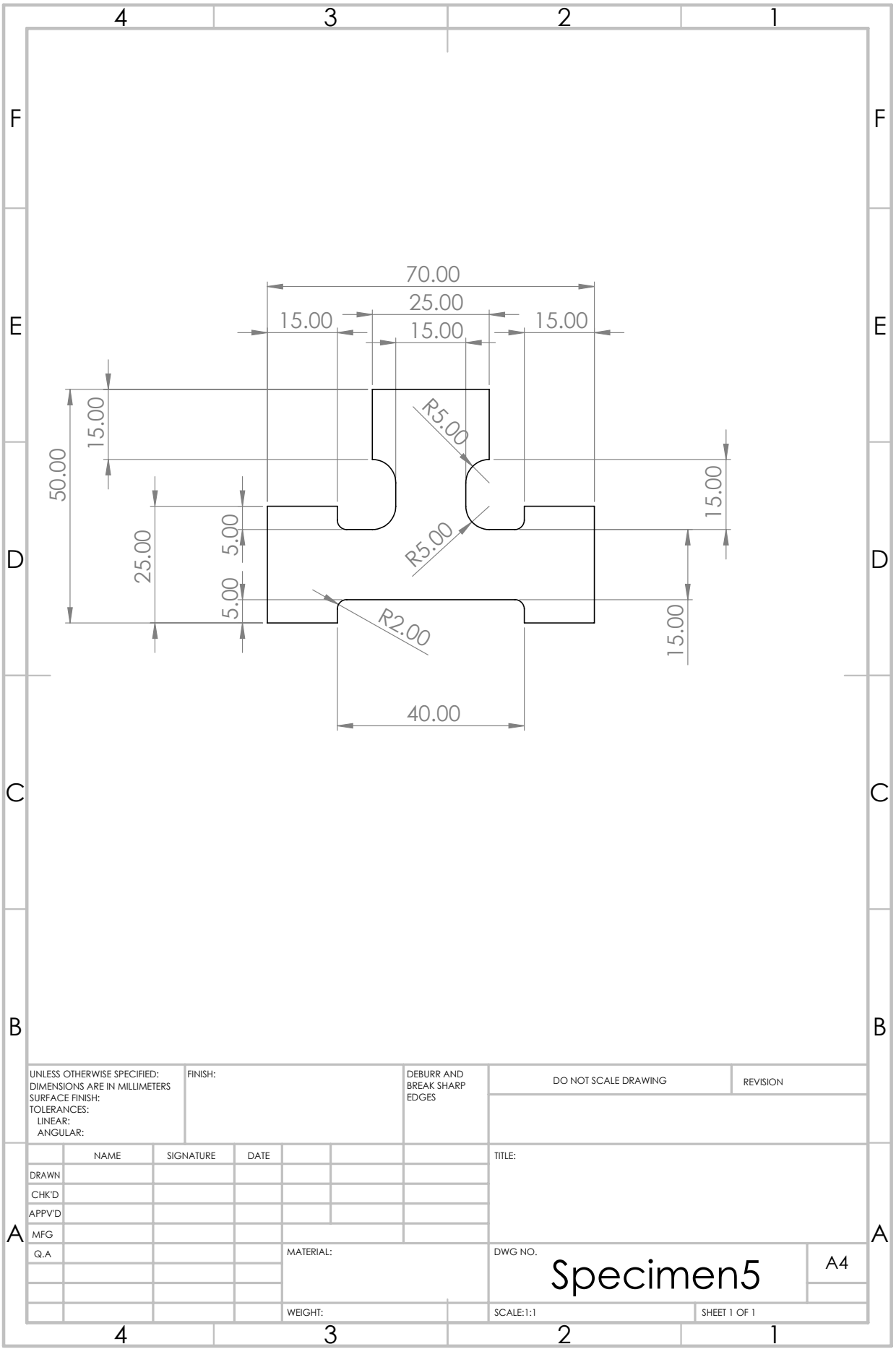
[6] G. Valeri, B. Koohbor, A. Kidane, M. A. Sutton, Determining the tensile response of materials at high temperature using DIC and the Virtual Fields Method, Optics and Lasers in Engineering 91 (2017) 53–61.

[7] P. Song, A. Trivedi, C. R. Siviour, Tensile testing of polymers: Integration of digital image correlation, infrared thermography and finite element modelling, Journal of the Mechanics and Physics of Solids 171 (2023) 105161.

[8] P. Song, A. R. Trived, C. R. Siviour, Mechanical response of two different molecular weight polycarbonates at varying rates and temperatures, EPJ Web of Conferences 250 (2021). Copyright - © 2021. This work is licensed under https://creativecommons.org/licenses/by/4.0/ (the "License"). Notwithstanding the ProQuest Terms and conditions, you may use this content in accordance with the terms of the License; Last updated - 2022-05-23.

[9] A. Graham, C. Siviour, Characterising the frequency-response of ultra-soft polymers with the virtual fields method, Strain 57 (2021) e12386.

Appendix A. T specimen design


4
3
2
1
F
E
D
C
B
A
70.00
25.00
15.00
15.00
15.00
15.00
50.00
25.00
5.00
5.00
R5.00
R5.00
R2.00
15.00
15.00
40.00
UNLESS OTHERWISE SPECIFIED:
DIMENSIONS ARE IN MILLIMETERS
SURFACE FINISH:
TOLERANCES:
LINEAR:
ANGULAR:
FINISH:
DEBURR AND BREAK SHARP EDGES
DO NOT SCALE DRAWING
REVISION
NAME
SIGNATURE
DATE
DRAWN
CHK'D
APPV'D
MFG
Q.A
TITLE:
MATERIAL:
DWG NO.
Specimen5
A4
WEIGHT:
SCALE:1:1
SHEET 1 OF 1

Appendix B. T Clamp

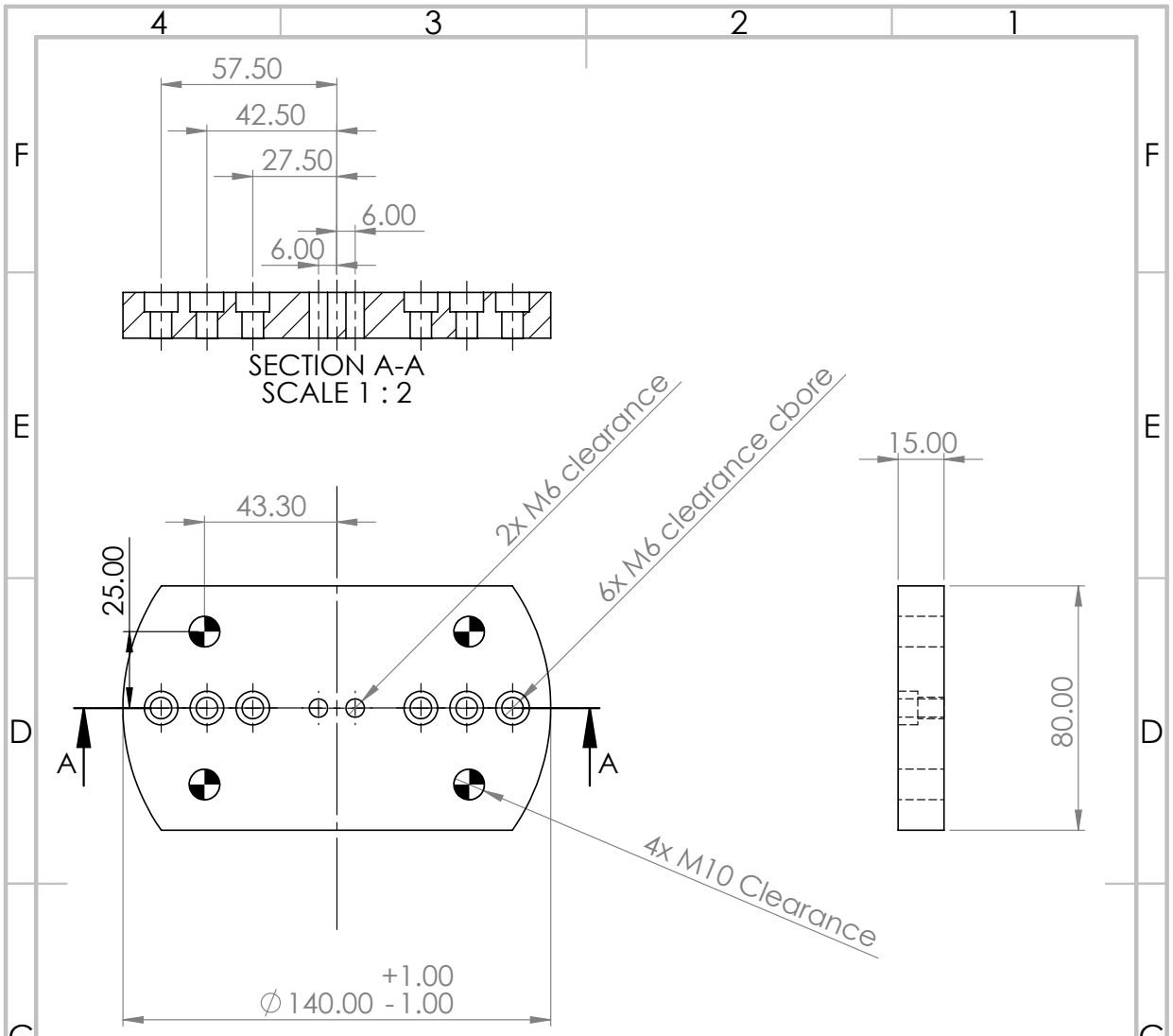


Plate thickness unimportant, to be between 15 and 20mm
All tolerances +- 0.1mm unless otherwise stated
All sharp edges 1mm chamfer
Quantity: 1
Material: Mild steel

DFR01810
Aaron Graham
07784051985

UNLESS OTHERWISE SPECIFIED: DIMENSIONS ARE IN MILLIMETERS SURFACE FINISH: TOLERANCES: LINEAR: ANGULAR:	FINISH:	DEBURR AND BREAK SHARP EDGES	DO NOT SCALE DRAWING / REVISION

	NAME	SIGNATURE	DATE
DRAWN	A Graham		
CHK'D			
APPV'D			
MFG			
Q.A			

TITLE: Base plate

MATERIAL: Mild Steel

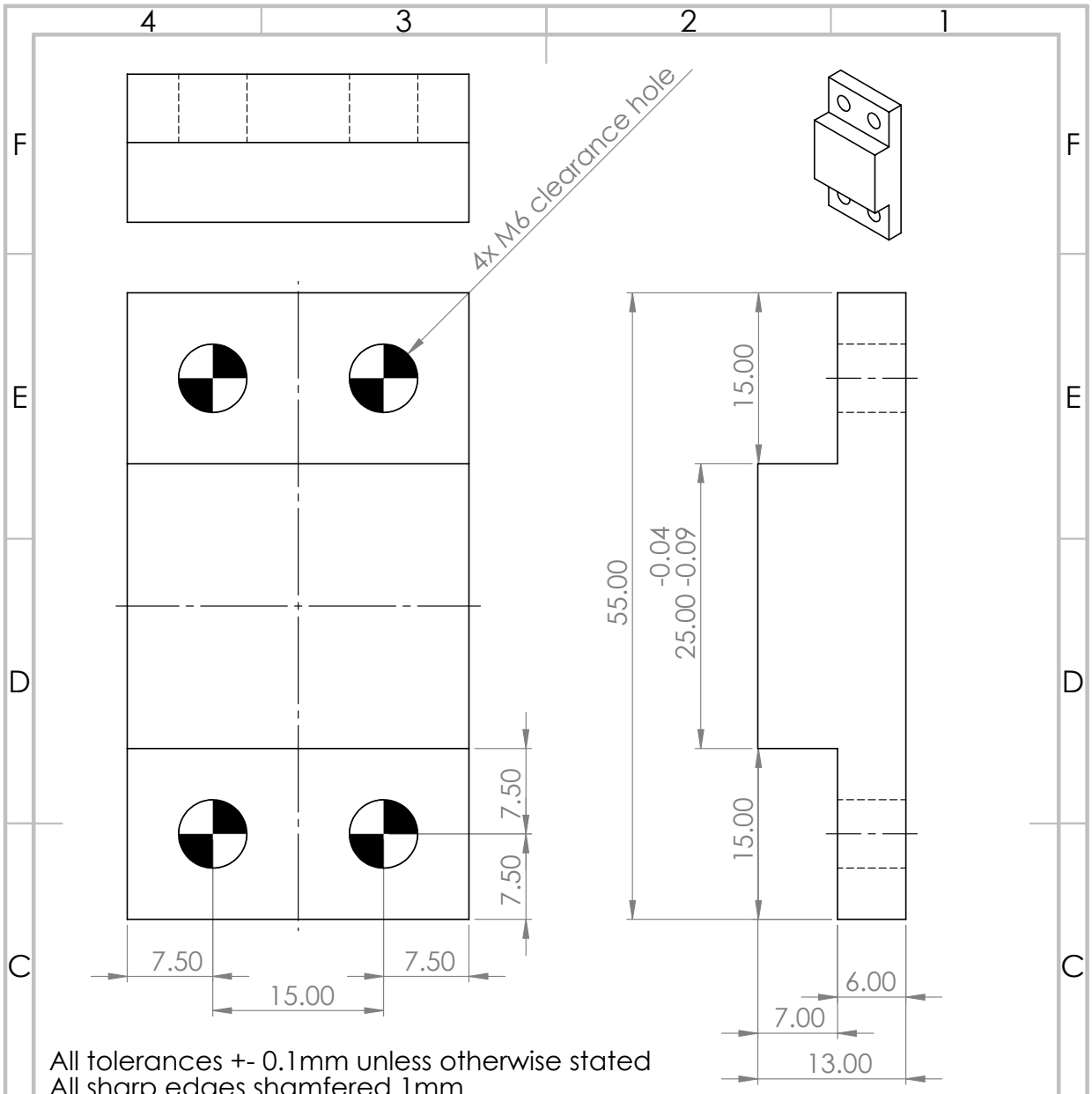
DWG NO. Base plate

A4

WEIGHT:

SCALE:1:5

SHEET 1 OF 1



All tolerances +- 0.1mm unless otherwise stated
All sharp edges shamfered 1mm
Part symmetrical about x and y axis
Quantity: 2
Material: Mild steel

Aaron Graham
DRF01800
07784051985

UNLESS OTHERWISE SPECIFIED: DIMENSIONS ARE IN MILLIMETERS SURFACE FINISH: TOLERANCES: LINEAR: ANGULAR:	FINISH:	DEBURR AND BREAK SHARP EDGES	DO NOT SCALE DRAWING / REVISION

	NAME	SIGNATURE	DATE
DRAWN	A Graham		
CHK'D			
APPV'D			
MFG			
Q.A			

TITLE: Clamp tab

MATERIAL: Mild Steel

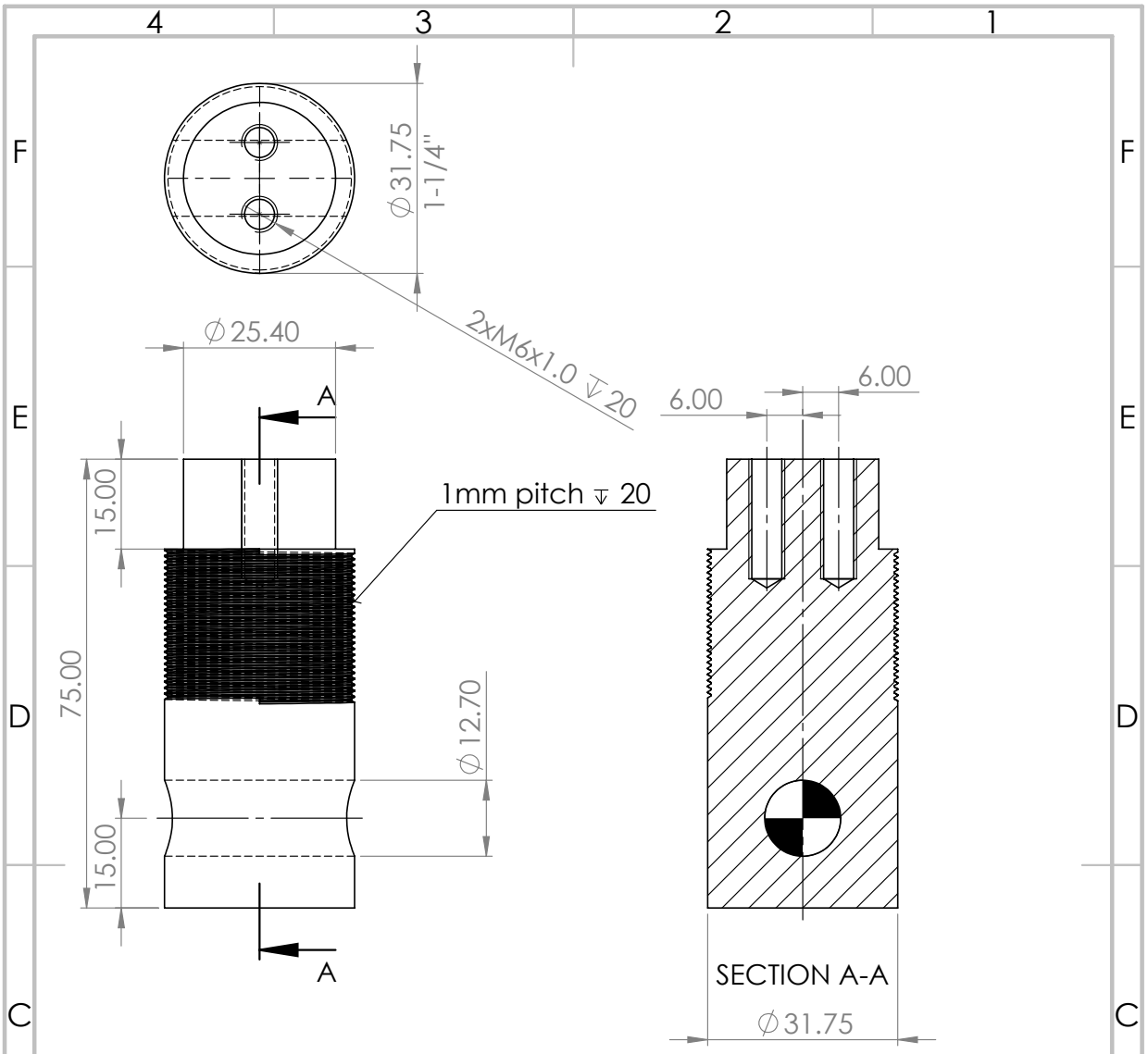
DWG NO. clamp tab

A4

WEIGHT:

SCALE:2:1

SHEET 1 OF 1



All tolerances +- 0.1mm unless otherwise stated

All sharp edges 1mm chamfer

Quantity : 1
Material: Mild steel

DRF01810
Aaron Graham
07784051985

UNLESS OTHERWISE SPECIFIED: DIMENSIONS ARE IN MILLIMETERS SURFACE FINISH: TOLERANCES: LINEAR: ANGULAR:	FINISH:	DEBURR AND BREAK SHARP EDGES	DO NOT SCALE DRAWING / REVISION

	NAME	SIGNATURE	DATE
DRAWN			
CHK'D			
APPV'D			
MFG			
Q.A			

TITLE: Instron base

MATERIAL: Mild steel

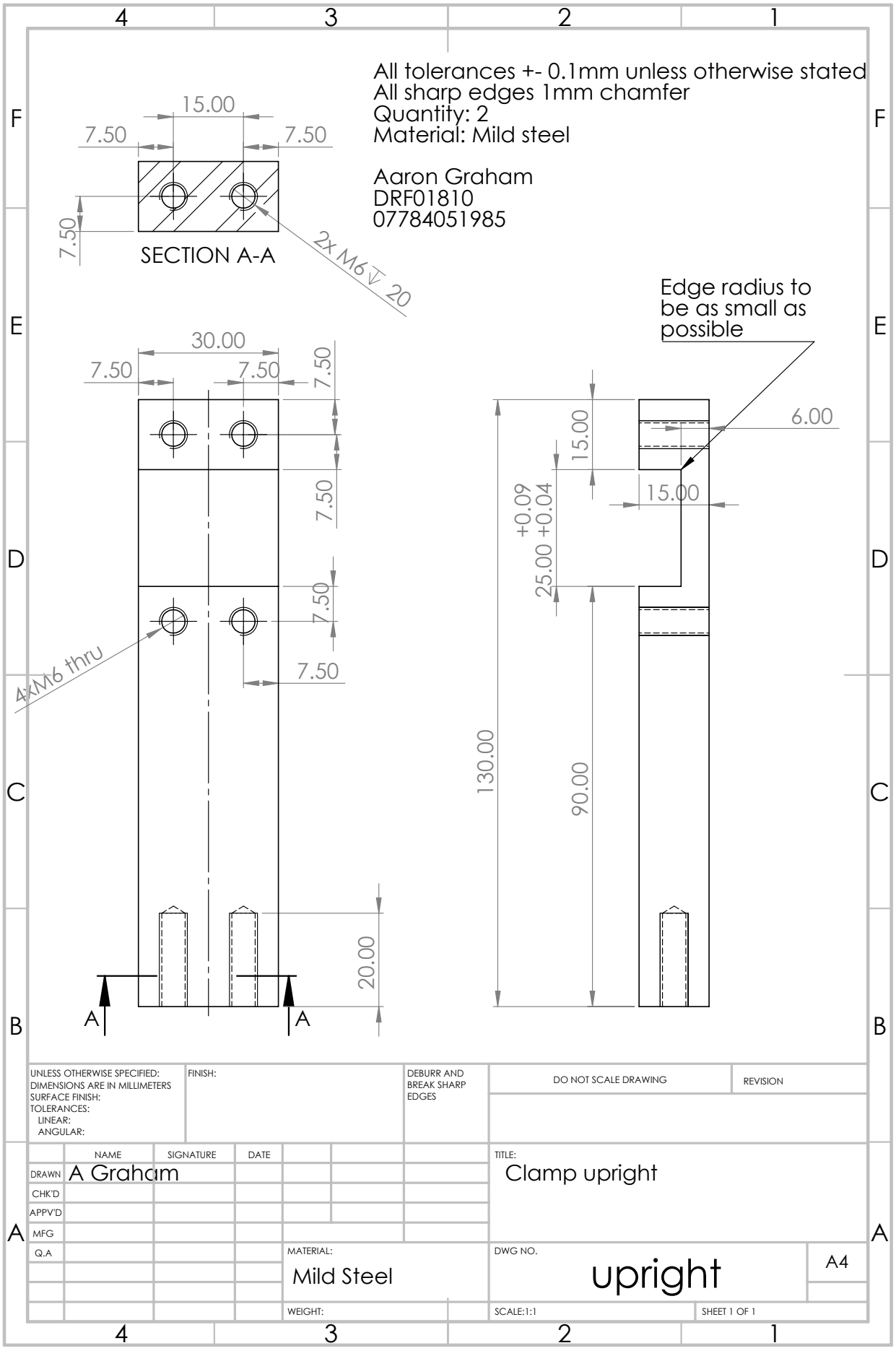
DWG NO. Instron Base

A4

WEIGHT:

SCALE:1:1

SHEET 1 OF 1


All tolerances +- 0.1mm unless otherwise stated
All sharp edges 1mm chamfer
Quantity: 2
Material: Mild steel
Aaron Graham
DRF01810
07784051985
15.00
7.50
7.50
7.50
SECTION A-A
2x M6▽ 20
Edge radius to be as small as possible
30.00
7.50
7.50
7.50
7.50
7.50
7.50
4xM6 thru
20.00
A
A
6.00
15.00
15.00
+0.09 +0.04
25.00
130.00
90.00
UNLESS OTHERWISE SPECIFIED:
DIMENSIONS ARE IN MILLIMETERS
SURFACE FINISH:
TOLERANCES:
LINEAR:
ANGULAR:
FINISH:
DEBURR AND BREAK SHARP EDGES
DO NOT SCALE DRAWING
REVISION
NAME
SIGNATURE
DATE
DRAWN
A Graham
CHK'D
APPV'D
MFG
Q.A
TITLE:
Clamp upright
MATERIAL:
Mild Steel
DWG NO.
upright
A4
WEIGHT:
SCALE:1:1
SHEET 1 OF 1

Statement of Authorship for joint/multi-authored papers for PGR thesis

To appear at the end of each thesis chapter submitted as an article/paper

The statement shall describe the candidate's and co-authors' independent research contributions in the thesis publications. For each publication there should exist a complete statement that is to be filled out and signed by the candidate and supervisor **(only required where there isn't already a statement of contribution within the paper itself).**

Title of Paper	Application of the T-test and the Virtual Fields Method to the Constitutive Response of Materials
Publication Status	□Published □ Accepted for Publication ■Submitted for Publication □Unpublished and unsubmitted work written in a manuscript style
Publication Details	

Student Confirmation

Student Name:	Aaron Graham		
Contribution to the Paper	Performed Experimental and analysis design, conducted experiments and analysis on samples, interpreted data, wrote manuscript Standard Tensile tests were conducted by a colleague, Peihao Song, with the data analysed and used in this paper alongside the T specimens		
Signature		Date	05-03-2024

Supervisor Confirmation

By signing the Statement of Authorship, you are certifying that the candidate made a substantial contribution to the publication, and that the description described above is accurate.

Supervisor name and title: Professor Clive Siviour		
Supervisor comments The statement above is correct.		
Signature 	Date	06/03/2024

This completed form should be included in the thesis, at the end of the relevant chapter.

8 Conclusions

This chapter consists of an overall conclusion and summary of the Thesis. More detailed conclusions and findings of each chapter are given at the end of each respective chapter. These conclusions are presented here in a more condensed form.

The novel apparatus, experimental and analytical techniques developed in this thesis overcome many of the difficulties associated with high rate tests on soft materials, mitigating or otherwise avoiding the consequences inherent to low wave-speeds, small forces, and extreme sensitivity to boundary conditions.

8.1 Summaries

8.1.1 Development of apparatus and methodology

The requisite apparatus and analysis method was successfully developed, and validated using an ultra-soft PDMS material. High rates of cyclic strain were accurately and repeatably obtained, with the primary limitation being the camera technology rather than the apparatus itself – as the strain rate increases, the displacement amplitude decreases, requiring increasing camera sensitivity even as resolution drops with frame-rate. For a more detailed explanation of this with some plots, see the appendix of chapter 4.

The limitation to strainrate in soft material testing is usually due to the slow wave-speed and the need to allow force to equilibrate[1], but this limitation was

[1] See start of chapter 4 for more detail on this

entirely overcome via the use of the VFM and high rate DIC – the acceleration terms became a beneficial source of signal rather than of error. As each experiment resulted in full-field characterisation, there was no need to assume homogeneity of specimens, unlike in traditional engineering testing. This had two advantages: naturally heterogeneous materials could be accurately tested, and any inhomogeneity in a nominally homogeneous sample was detected, validating assumptions made about the sample.

Sensitivity to boundary conditions was successfully mitigated via the use of the VFM, improving the accuracy and repeatability of each experiment. The apparatus and analytical techniques developed in this thesis are capable of and allow for the characterisation of ultra-soft materials under conditions that would be difficult of impossible using traditional engineering test methodologies.

8.1.2 Sylgard

In spite of Sylgard 184 being a standard engineering polymer, there is a large spread of reported properties quoted in the literature. This is likely to be due to a combination of difficulty in accurately testing soft materials, and insufficient curing of specimens. This section showed that the cure times specified by the manufacturer are insufficient for full curing to occur, likely leading to some of the spread in the literature.

After accurately characterising the frequency dependant moduli of Sylgard 184 for a range of crosslinker percentages and temperatures, it was shown that traditional TTS methods could not be accurately used to extend this data to higher rates. This is important, as the results of TTS shifting are often unfalsifiable. A modified TTS method was developed, and validated against high rate testing of the same materials. This high rate testing both validated the modified TTS methodology, as well as provided data that would otherwise be difficult or impossible to obtain.

8.1.3 Bio-materials

A combination of low frequency rheometry and high rate shear testing was conducted on both porcine brain tissue and agarose gel of varying concentrations. The low rate results on both materials matched those present in the literature. The high rate results for both materials fitted what one would expect from the low rate results. The brain tissue was significantly stiffer at lower temperatures than at body-temperatures, a result that matches those in the literature.

The agarose gels were slightly stiffer than expected at high rates, but this is likely due to the high rate tests having a slightly higher strain amplitude than the low rate rheometry. Agarose gel is sensitive to strain amplitude, and so this result is expected.

A deliberately inhomogeneous agarose sample was prepared and tested, and the full-field modulus results clearly showed the expected inhomogeneity. Some inhomogeneity was also detected in the tests on brain tissue, which was expected, as the samples contained some grey matter – white matter is slightly stiffer than grey matter, and the results matched

8.1.4 VFM on Engineering materials

The previous chapters focused on obtaining material characterisation data that would be difficult or impossible to obtain using traditional engineering test methodology. These data are valuable, but do not fully exploit the capability of the VFM to extract multiple material parameters per test. In this chapter, experiments are conducted at quasi-static rates on relatively stiff materials (polycarbonate and aluminium), with geometry chosen such that the specimen experienced a deliberately heterogeneous strain state.

The focus for this chapter was on exploiting the VFM to extract multiple material parameters from a single test, as well as separating the geometric and material contributions to overall specimen response. Each single experiment obtained data for the full range of plane-stress states including compression and biaxial tension. The total response was decomposed into geometric and material contributions, allowing for accurate and efficient fitting of material parameters unaffected by

phenomena such as necking. Once geometric non-linearities have been taken into account, apparently complex behaviour could be accurately predicted using only a simple material model.

8.2 Future work

This thesis has achieved its research goals, developing an apparatus and test methodology capable of testing soft biological tissue at high strain rates whilst obviating the barriers presented by sensitivity to boundary conditions, low wave-speed, and extreme bulk:shear modulus ratio.

There are several clear areas of promising future work extending the work done for this thesis. Whilst they are beyond the scope of this thesis, the following are recommended as future work following on from this thesis:

Extension to stiffer materials Whilst this apparatus was designed for the testing of soft materials, it shows promise for extension to stiffer materials. This would require the use of higher power smart-shakers and strengthening of the apparatus, as well as the fixing of the top of the specimen – all things which are entirely feasible. Additionally, if the material were substantially stiffer, the specimen geometry could be modified to be a hollow tube, reducing stiffness and increasing accuracy of the analytical assumptions. This would likely prove particularly valuable for validation of high rate behaviour of materials such as polycarbonate, particularly at higher temperatures

Further changes to boundary conditions Whilst this thesis only tested the effects of temperature on the mechanical response of brain tissue, brain tissue is sensitive to a wide range of changes in boundary conditions. In particular, it has been shown to reversibly stiffen when a voltage is applied. The application of a voltage across the specimen could easily be implemented, and would lead to valuable results.

Dynamic T-test Combining the analysis done in chapters 4 to 6 with the methodology of chapter 7 would allow for the full-field dynamic characterisation of materials such as polycarbonate whilst keeping the same advantages of the T test geometry. Replacing the tensile grip with the fatigue testing grip such that the loading is quasi-static linear displacement with frequency components superimposed would allow for one to characterise the frequency dependant behaviour of a material over a range of frequencies and plane-stress states.

Whilst the experimental setup would be challenging, it would allow for a single test to obtain a wide range of dynamic material properties, whilst separating out the effects of geometric non-linearities that often confound results.

Deviatoric testing The work in this thesis primarily focused on pure dilatational loading of brain tissue, as that is the loading mode of primary importance. The behaviour of brain tissue under deviatoric loading is still important however, if significantly challenging to test accurately. Appendix A shows a set of designs and simulations for a proposed test methodology that would be capable of characterising brain tissue under dilatational loading at high rates.

References

[1] P Hartmann et al. "[Normal weight of the brain in adults in relation to age, sex, body height and weight]." In: *Der Pathologe* 15 (3 June 1994), pp. 165–70. URL: http://www.ncbi.nlm.nih.gov/pubmed/8072950.

[2] Karol. Miller. *Biomechanics of the brain*. Springer, 2011, p. 225.

[3] Silvia Budday et al. "Mechanical properties of gray and white matter brain tissue by indentation". In: *Journal of the Mechanical Behavior of Biomedical Materials* 46 (June 2015), pp. 318–330. URL: https://www.sciencedirect.com/science/article/pii/S1751616115000673.

[4] Silvia Budday et al. "Fifty Shades of Brain: A Review on the Mechanical Testing and Modeling of Brain Tissue". In: *Archives of Computational Methods in Engineering* (July 2019), pp. 1–44. URL: http://link.springer.com/10.1007/s11831-019-09352-w.

[5] S. Chatelin et al. "Towards child versus adult brain mechanical properties". In: *Journal of the Mechanical Behavior of Biomedical Materials* 6 (Feb. 2012), pp. 166–173. URL: https://www.sciencedirect.com/science/article/pii/S1751616111002475.

[6] G. Franceschini et al. "Brain tissue deforms similarly to filled elastomers and follows consolidation theory". In: *Journal of the Mechanics and Physics of Solids* 54 (12 Dec. 2006), pp. 2592–2620. URL: https://www.sciencedirect.com/science/article/pii/S0022509606000883.

[7] Kathrin Holtzmann et al. "Brain tissue stiffness is a sensitive marker for acidosis". In: *Journal of Neuroscience Methods* 271 (Sept. 2016), pp. 50–54. URL: https://www.sciencedirect.com/science/article/pii/S0165027016301558.

[8] David F. Moore et al. "Computational biology — Modeling of primary blast effects on the central nervous system". In: *NeuroImage* 47 (Aug. 2009), T10–T20. URL: https://www.sciencedirect.com/science/article/pii/S1053811909001438.

[9] Antoine Jérusalem and Ming Dao. "Continuum modeling of a neuronal cell under blast loading". In: *Acta Biomaterialia* 8 (9 Sept. 2012), pp. 3360–3371. URL: https://www.sciencedirect.com/science/article/pii/S174270611200195X.

[10] Wynn Legon et al. "Transcranial focused ultrasound neuromodulation of the human primary motor cortex". In: *Scientific Reports* 8 (1 Dec. 2018), p. 10007. URL: http://www.nature.com/articles/s41598-018-28320-1.

[11] Mark H Wilson. "Traumatic brain injury: an underappreciated public health issue". In: *The Lancet Public Health* 1 (2 Dec. 2016), e44. URL: https://www.sciencedirect.com/science/article/pii/S2468266716300226.

[12] Marek Majdan et al. "Epidemiology of traumatic brain injuries in Europe: a cross-sectional analysis". In: *The Lancet Public Health* 1 (2 Dec. 2016), e76–e83. URL: https://www.sciencedirect.com/science/article/pii/S2468266716300172.

[13] Ragini Verma et al. "Neuroimaging Findings in US Government Personnel With Possible Exposure to Directional Phenomena in Havana, Cuba". In: *JAMA* 322 (4 July 2019), pp. 336–347. URL: https://jamanetwork.com/journals/jama/fullarticle/2738552?guestAccessKey=47486c47-c01c-47fa-8b6e-41fc69f29cf4&utm_source=For_The_Media&utm_medium=referral&utm_campaign=ftm_links&utm_content=tfl&utm_term=072319.

[14] S. Budday et al. "Mechanical characterization of human brain tissue". In: *Acta Biomaterialia* 48 (Jan. 2017), pp. 319–340. URL: https://www.sciencedirect.com/science/article/pii/S1742706116305633.

[15] L. Angela Mihai et al. "A comparison of hyperelastic constitutive models applicable to brain and fat tissues". In: *Journal of The Royal Society Interface* 12 (110 Sept. 2015), p. 20150486. URL: https://royalsocietypublishing.org/doi/10.1098/rsif.2015.0486.

[16] Dongli Li et al. "3D multicellular model of shock wave-cell interaction". In: *Acta Biomaterialia* 77 (Sept. 2018), pp. 282–291. URL: https://www.sciencedirect.com/science/article/pii/S1742706118302447.

[17] Valentina Balbi et al. "Poynting effect of brain matter in torsion". In: *Soft Matter* 15 (25 2019), pp. 5147–5153.

[18] L E Bilston, Z Liu, and N Phan-Thien. "Large strain behaviour of brain tissue in shear: some experimental data and differential constitutive model." In: *Biorheology* 38 (4 2001), pp. 335–45. URL: http://www.ncbi.nlm.nih.gov/pubmed/11673648.

[19] D W A. Brands. "The Large Shear Strain Dynamic Behavior of In-Vitro Porcine Brain Tissue and a Silicone Gel Model Material". In: vol. 1. SAE International, Nov. 2018.

[20] Simon Chatelin, André Constantinesco, and Rémy Willinger. "Fifty years of brain tissue mechanical testing: from in vitro to in vivo investigations." In: *Biorheology* 47 (5-6 2010), pp. 255–76. URL: http://www.ncbi.nlm.nih.gov/pubmed/21403381.

[21] Shaokoon Cheng and Lynne E. Bilston. "Unconfined compression of white matter". In: *Journal of Biomechanics* 40 (1 Jan. 2007), pp. 117–124. URL: https://www.sciencedirect.com/science/article/pii/S002192900500521X.

[22] K.K. Darvish and J.R. Crandall. "Nonlinear viscoelastic effects in oscillatory shear deformation of brain tissue". In: *Medical Engineering Physics* 23 (9 Nov. 2001), pp. 633–645. URL: https://www.sciencedirect.com/science/article/pii/S1350453301001011.

[23] Rijk de Rooij and Ellen Kuhl. "Constitutive Modeling of Brain Tissue: Current Perspectives". In: *Applied Mechanics Reviews* 68 (1 Jan. 2016), p. 010801. URL: http://appliedmechanicsreviews.asmedigitalcollection.asme.org/article.aspx?doi=10.1115/1.4032436.

[24] Wolfgang Ehlers and Bernd Markert. "A Linear Viscoelastic Biphasic Model for Soft Tissues Based on the Theory of Porous Media". In: *Journal of Biomechanical Engineering* 123 (5 2001), p. 418. URL: http://biomechanical.asmedigitalcollection.asme.org/article.aspx?articleid=1476122.

[25] Antonio Elia Forte. "Brain Tissue Biomechanics : New Tissue Phantoms , Mechanical Characterisation and Modelling Strategies for Enhanced Surgical". In: (November 2015).

[26] Amit Gefen and Susan S Margulies. "Are in vivo and in situ brain tissues mechanically similar?" In: *Journal of Biomechanics* 37 (9 Sept. 2004), pp. 1339–1352. URL: https://www.sciencedirect.com/science/article/pii/S0021929004000090.

[27] Alain Goriely et al. "Mechanics of the brain: perspectives, challenges, and opportunities". In: *Biomechanics and Modeling in Mechanobiology* 14 (5 Oct. 2015), pp. 931–965. URL: http://dx.doi.org/10.1007/s10237-015-0662-4http://link.springer.com/10.1007/s10237-015-0662-4.

[28] M Hrapko et al. "The mechanical behaviour of brain tissue: large strain response and constitutive modelling." In: *Biorheology* 43 (5 2006), pp. 623–36. URL: http://www.ncbi.nlm.nih.gov/pubmed/17047281.

[29] T. Kaster, I. Sack, and A. Samani. "Measurement of the hyperelastic properties of ex vivo brain tissue slices". In: *Journal of Biomechanics* 44 (6 Apr. 2011), pp. 1158–1163. URL: https://www.sciencedirect.com/science/article/pii/S0021929011000492.

[30] L. Angela Mihai et al. "A family of hyperelastic models for human brain tissue". In: *Journal of the Mechanics and Physics of Solids* 106 (Sept. 2017), pp. 60–79. URL: https://www.sciencedirect.com/science/article/pii/S0022509617302703.

[31] Karol Miller and Kiyoyuki Chinzei. "Mechanical properties of brain tissue in tension". In: *Journal of Biomechanics* 35 (4 Apr. 2002), pp. 483–490. URL: https://www.sciencedirect.com/science/article/pii/S0021929001002342https://www.sciencedirect.com/science/article/pii/S0021929001002342#FIG3.

[32] Michael T. Prange and Susan S. Margulies. "Regional, Directional, and Age-Dependent Properties of the Brain Undergoing Large Deformation". In: *Journal of Biomechanical Engineering* 124 (2 2002), p. 244. URL: http://biomechanical.asmedigitalcollection.asme.org/article.aspx?articleid=1407804.

[33] K. P. Wilkie, C. S. Drapaca, and S. Sivaloganathan. "Aging impact on brain biomechanics with applications to hydrocephalus". In: *Mathematical Medicine and Biology* 29 (2 June 2012), pp. 145–161. URL: https://academic.oup.com/imammb/article-lookup/doi/10.1093/imammb/dqr001.

[34] Arvin Arani et al. "In vivo, high-frequency three-dimensional cardiac MR elastography: Feasibility in normal volunteers". In: *Magnetic Resonance in Medicine* 77 (1 Jan. 2017), pp. 351–360. URL: http://www.ncbi.nlm.nih.gov/pubmed/26778442http://www.pubmedcentral.nih.gov/articlerender.fcgi?artid=PMC4947569http://doi.wiley.com/10.1002/mrm.26101.

[35] Lynne E. Bilston, Zizhen Liu, and Nhan Phan-Thien. "Linear Viscoelastic Properties of Bovine Brain Tissue in Shear". In: *Biorheology* 34 (6 Dec. 1997), pp. 377–385. URL: http://www.medra.org/servlet/aliasResolver?alias=iospress&doi=10.3233/BIR-1997-34603.

[36] Jonathan Bishop et al. "Magnetic resonance imaging of shear wave propagation in excised tissue". In: *Journal of Magnetic Resonance Imaging* 8 (6 Nov. 1998), pp. 1257–1265. URL: http://doi.wiley.com/10.1002/jmri.1880080613.

[37] Andreas Fehlner et al. "Cerebral multifrequency MR elastography by remote excitation of intracranial shear waves". In: *NMR in Biomedicine* 28 (11 Nov. 2015), pp. 1426–1432. URL: http://doi.wiley.com/10.1002/nbm.3388.

[38] Andreas Fehlner et al. "Higher-resolution MR elastography reveals early mechanical signatures of neuroinflammation in patients with clinically isolated syndrome". In: *Journal of Magnetic Resonance Imaging* 44 (1 July 2016), pp. 51–58. URL: http://doi.wiley.com/10.1002/jmri.25129.

[39] Andreas Fehlner et al. "Increasing the spatial resolution and sensitivity of magnetic resonance elastography by correcting for subject motion and susceptibility-induced image distortions". In: *Journal of Magnetic Resonance Imaging* 46 (1 July 2017), pp. 134–141. URL: http://doi.wiley.com/10.1002/jmri.25516.

[40] John D. Finan et al. "Regional mechanical properties of human brain tissue for computational models of traumatic brain injury". In: *Acta Biomaterialia* 55 (June 2017), pp. 333–339. URL: https://www.sciencedirect.com/science/article/pii/S1742706117302076.

[41] Jing Guo et al. "Towards an Elastographic Atlas of Brain Anatomy". In: *PLoS ONE* 8 (8 Aug. 2013). Ed. by Assad Anshuman Oberai, e71807. URL: https://dx.plos.org/10.1371/journal.pone.0071807.

[42] Xunan Huang et al. "Magnetic resonance elastography of the brain: A study of feasibility and reproducibility using an ergonomic pillow-like passive driver". In: *Magnetic Resonance Imaging* 59 (June 2019), pp. 68–76. URL: https://linkinghub.elsevier.com/retrieve/pii/S0730725X18305460.

[43] Curtis L. Johnson and Eva H. Telzer. *Magnetic resonance elastography for examining developmental changes in the mechanical properties of the brain.* Oct. 2018. URL: https://www.sciencedirect.com/science/article/pii/S1878929317300373?via%3Dihubhttps://linkinghub.elsevier.com/retrieve/pii/S1878929317300373.

[44] Scott A. Kruse et al. "Magnetic resonance elastography of the brain". In: *NeuroImage* 39 (1 Jan. 2008), pp. 231–237. URL: https://www.sciencedirect.com/science/article/pii/S1053811907007161.

[45] Yan-Lin Liu et al. "In vivo and ex vivo elastic properties of brain tissues measured with ultrasound elastography". In: *Journal of the Mechanical Behavior of Biomedical Materials* 83 (July 2018), pp. 120–125. URL: https://www.sciencedirect.com/science/article/pii/S1751616118305198.

[46] Clayton T. McKee et al. “Indentation Versus Tensile Measurements of Young’s Modulus for Soft Biological Tissues”. In: *Tissue Engineering Part B: Reviews* 17 (3 June 2011), pp. 155–164. URL: https://www.liebertpub.com/doi/10.1089/ten.teb.2010.0520.

[47] Stéphane Nicolle, Mourad Lounis, and Rémy Willinger. “Shear Properties of Brain Tissue over a Frequency Range Relevant for Automotive Impact Situations: New Experimental Results.” In: *Stapp car crash journal* 48 (Nov. 2004), pp. 239–58. URL: http://www.ncbi.nlm.nih.gov/pubmed/17230269.

[48] Long Qian et al. “Indentation response in porcine brain under electric fields”. In: *Soft Matter* 15 (4 Jan. 2019), pp. 623–632. URL: http://xlink.rsc.org/?DOI=C8SM01272E.

[49] Abbas Samani et al. “Measuring the elastic modulus of ex vivo small tissue samples”. In: *Physics in Medicine and Biology* 48 (14 July 2003), pp. 2183–2198. URL: http://stacks.iop.org/0031-9155/48/i=14/a=310?key=crossref.5b37962ee83fc7e56b01a4b1bde585cc.

[50] Ingolf Sack et al. “Non-invasive measurement of brain viscoelasticity using magnetic resonance elastography”. In: *NMR in Biomedicine* 21 (3 Apr. 2008), pp. 265–271. URL: http://doi.wiley.com/10.1002/nbm.1189.

[51] Alexander V. Shulyakov et al. “Age-dependence of intracranial viscoelastic properties in living rats”. In: *Journal of the Mechanical Behavior of Biomedical Materials* 4 (3 Apr. 2011), pp. 484–497. URL: https://www.sciencedirect.com/science/article/pii/S1751616110001876.

[52] Jade Yeung et al. “Paediatric brain tissue properties measured with magnetic resonance elastography”. In: *Biomechanics and Modeling in Mechanobiology* (May 2019). URL: http://link.springer.com/10.1007/s10237-019-01157-x.

[53] E Weichart. “Ueber die elastische Nachwirkung”. Königsberg University, Germany, Jan. 1889. URL: http://doi.wiley.com/10.1002/andp.18782400607.

[54] S. Budday et al. “Viscoelastic parameter identification of human brain tissue”. In: *Journal of the Mechanical Behavior of Biomedical Materials* 74 (Oct. 2017), pp. 463–476. URL: https://www.sciencedirect.com/science/article/pii/S1751616117303004.

[55] Kaveh Laksari, Mehdi Shafieian, and Kurosh Darvish. “Constitutive model for brain tissue under finite compression”. In: *Journal of Biomechanics* 45 (4 Feb. 2012), pp. 642–646. URL: https://www.sciencedirect.com/science/article/pii/S002192901200022X.

[56] Karol Miller and Kiyoyuki Chinzei. “Constitutive modelling of brain tissue: Experiment and theory”. In: *Journal of Biomechanics* 30 (11-12 Nov. 1997), pp. 1115–1121. URL: https://www.sciencedirect.com/science/article/pii/S0021929097000924.

[57] Badar Rashid, Michel Destrade, and Michael D. Gilchrist. “Mechanical characterization of brain tissue in simple shear at dynamic strain rates”. In: *Journal of the Mechanical Behavior of Biomedical Materials* 28 (Dec. 2013), pp. 71–85. URL: https://www.sciencedirect.com/science/article/pii/S175161611300249X.

[58] Badar Rashid, Michel Destrade, and Michael D Gilchrist. "Mechanical characterization of brain tissue in tension at dynamic strain rates". In: *Journal of the Mechanical Behavior of Biomedical Materials* 33 (May 2014), pp. 43–54. URL: https://www.sciencedirect.com/science/article/pii/S175161611200224X.

[59] R. W. Ogden. "Large Deformation Isotropic Elasticity - On the Correlation of Theory and Experiment for Incompressible Rubberlike Solids". In: *Proceedings of the Royal Society A: Mathematical, Physical and Engineering Sciences* 326 (1567 Feb. 1972), pp. 565–584. URL: http://rspa.royalsocietypublishing.org/cgi/doi/10.1098/rspa.1972.0026.

[60] A. N. Gent. "A New Constitutive Relation for Rubber". In: *Rubber Chemistry and Technology* 69 (1 Mar. 1996), pp. 59–61. URL: http://rubberchemtechnol.org/doi/abs/10.5254/1.3538357.

[61] Hilmi Demiray. "A note on the elasticity of soft biological tissues". In: *Journal of Biomechanics* 5 (3 May 1972), pp. 309–311. URL: https://www.sciencedirect.com/science/article/pii/0021929072900474.

[62] Gerhard A. Holzapfel, Thomas C. Gasser, and Ray W. Ogden. "A New Constitutive Framework for Arterial Wall Mechanics and a Comparative Study of Material Models". In: *Journal of Elasticity* 61 (1/3 2000), pp. 1–48. URL: http://link.springer.com/10.1023/A:1010835316564.

[63] J.D. Humphrey. "Review Paper: Continuum biomechanics of soft biological tissues". In: *Proceedings of the Royal Society of London. Series A: Mathematical, Physical and Engineering Sciences* 459 (2029 Jan. 2003), pp. 3–46. URL: https://royalsocietypublishing.org/doi/10.1098/rspa.2002.1060.

[64] R. W. Ogden, G. Saccomandi, and I. Sgura. "Fitting hyperelastic models to experimental data". In: *Computational Mechanics* 34 (6 Nov. 2004), pp. 484–502. URL: http://link.springer.com/10.1007/s00466-004-0593-y.

[65] Stefanie Reese and Sanjay Govindjee. "A theory of finite viscoelasticity and numerical aspects". In: *International Journal of Solids and Structures* 35 (26-27 Sept. 1998), pp. 3455–3482. URL: https://www.sciencedirect.com/science/article/pii/S0020768397002175.

[66] Thibault P. Prevost et al. "Biomechanics of brain tissue". In: *Acta Biomaterialia* 7 (1 Jan. 2011), pp. 83–95. URL: https://www.sciencedirect.com/science/article/pii/S1742706110003016.

[67] Amit Gefen et al. "Age-Dependent Changes in Material Properties of the Brain and Braincase of the Rat". In: *Journal of Neurotrauma* 20 (11 2003), pp. 1163–1177.

[68] V. Libertiaux, F. Pascon, and S. Cescotto. "Experimental verification of brain tissue incompressibility using digital image correlation". In: *Journal of the Mechanical Behavior of Biomedical Materials* 4 (7 Oct. 2011), pp. 1177–1185. URL: https://www.sciencedirect.com/science/article/pii/S1751616111000737.

[69] Dongli Li et al. “Response of Single Cells to Shock Waves and Numerically Optimized Waveforms for Cancer Therapy.” In: *Biophysical journal* 114 (6 Mar. 2018), pp. 1433–1439. URL: http://www.ncbi.nlm.nih.gov/pubmed/29590600http://www.pubmedcentral.nih.gov/articlerender.fcgi?artid=PMC5883951.

[70] D. E. Ingber. “Tensegrity I. Cell structure and hierarchical systems biology”. In: *Journal of Cell Science* 116 (7 2003), pp. 1157–1173.

[71] Antoine Jerusalem et al. “Electrophysiological-mechanical coupling in the neuronal membrane and its role in ultrasound neuromodulation and general anaesthesia”. In: *Acta Biomaterialia* (July 2019). URL: https://www.sciencedirect.com/science/article/pii/S1742706119305306.

[72] Haoyu Chen, Daniel Garcia-Gonzalez, and Antoine Jérusalem. “Computational model of the mechanoelectrophysiological coupling in axons with application to neuromodulation”. In: *Physical Review E* 99 (3 Mar. 2019), p. 032406. URL: https://link.aps.org/doi/10.1103/PhysRevE.99.032406.

[73] Jonathan Vappou et al. “Assessment of in vivo and post-mortem mechanical behavior of brain tissue using magnetic resonance elastography”. In: *Journal of Biomechanics* 41 (14 Oct. 2008), pp. 2954–2959. URL: https://www.sciencedirect.com/science/article/pii/S0021929008003965.

[74] J. Weickenmeier et al. “Brain stiffens post mortem”. In: *Journal of the Mechanical Behavior of Biomedical Materials* 84 (May Aug. 2018), pp. 88–98. URL: https://doi.org/10.1016/j.jmbbm.2018.04.009https://linkinghub.elsevier.com/retrieve/pii/S1751616118304818.

[75] Charlotte A. Guertler et al. “Mechanical properties of porcine brain tissue in vivo and ex vivo estimated by MR elastography”. In: *Journal of Biomechanics* 69 (Mar. 2018), pp. 10–18. URL: https://www.sciencedirect.com/science/article/pii/S0021929018300344.

[76] A Garo et al. “Towards a reliable characterisation of the mechanical behaviour of brain tissue: The effects of post-mortem time and sample preparation.” In: *Biorheology* 44 (1 2007), pp. 51–8. URL: http://www.ncbi.nlm.nih.gov/pubmed/17502689.

[77] Wei Zhang et al. “Effect of in vitro storage duration on measured mechanical properties of brain tissue”. In: *Scientific Reports* 8 (1 Dec. 2018), p. 1247. URL: http://www.nature.com/articles/s41598-018-19687-2.

[78] Madhuvanthi A. Kandadai, Jason L. Raymond, and George J. Shaw. “Comparison of electrical conductivities of various brain phantom gels: Developing a ‘brain gel model’”. In: *Materials Science and Engineering: C* 32 (8 Dec. 2012), pp. 2664–2667. URL: https://www.sciencedirect.com/science/article/pii/S0928493112003426.

[79] S.M. Park et al. “Gelled versus nongelled phantom material for measurement of MRI-induced temperature increases with bioimplants”. In: *IEEE Transactions on Magnetics* 39 (5 Sept. 2003), pp. 3367–3371. URL: http://ieeexplore.ieee.org/document/1233400/.

[80] Jonathan B. Leonard, Kenneth R. Foster, and T. Whit Athley. "Thermal Properties of Tissue Equivalent Phantom Materials". In: *IEEE Transactions on Biomedical Engineering* BME-31 (7 July 1984), pp. 533–536. URL: http://ieeexplore.ieee.org/document/4121886/.

[81] Antonio E. Forte et al. "A composite hydrogel for brain tissue phantoms". In: *Materials Design* 112 (Dec. 2016), pp. 227–238. URL: https://www.sciencedirect.com/science/article/pii/S0264127516312370.

[82] Miriam Lozoya. "Development of a Tissue-Mimicking Brain Phantom for Neurosurgical Pre-Operative Planning and Training". Clemson university, 2016. URL: https://tigerprints.clemson.edu/all_theses/2550.

[83] Guy Lamouche et al. "Review of tissue simulating phantoms with controllable optical, mechanical and structural properties for use in optical coherence tomography." In: *Biomedical optics express* 3 (6 June 2012), pp. 1381–98. URL: http://www.ncbi.nlm.nih.gov/pubmed/22741083http://www.pubmedcentral.nih.gov/articlerender.fcgi?artid=PMC3370977.

[84] Penny L. Hubbard et al. "Biomimetic phantom for the validation of diffusion magnetic resonance imaging". In: *Magnetic Resonance in Medicine* 73 (1 Jan. 2015), pp. 299–305. URL: http://doi.wiley.com/10.1002/mrm.25107.

[85] Rachelle N. Palchesko et al. "Development of Polydimethylsiloxane Substrates with Tunable Elastic Modulus to Study Cell Mechanobiology in Muscle and Nerve". In: *PLoS ONE* 7 (12 2012).

[86] Céline Kayal et al. "Mechanical Response of Neural Cells to Physiologically Relevant Stiffness Gradients". In: *Advanced Healthcare Materials* 9 (8 2020).

[87] V. Placet and P. Delobelle. "Mechanical properties of bulk polydimethylsiloxane for microfluidics over a large range of frequencies and aging times". In: *Journal of Micromechanics and Microengineering* 25 (3 2015).

[88] F. Schneider et al. "Mechanical properties of silicones for MEMS". In: *Journal of Micromechanics and Microengineering* 18 (6 2008).

[89] Florian Schneider et al. "Process and material properties of polydimethylsiloxane (PDMS) for Optical MEMS". In: *Sensors and Actuators, A: Physical* 151 (2 2009), pp. 95–99.

[90] Jessamine Ng Lee et al. "Compatibility of mammalian cells on surfaces of poly(dimethylsiloxane)". In: *Langmuir* 20 (26 2004), pp. 11684–11691.

[91] Matthew C. Murphy et al. "Measuring the Characteristic Topography of Brain Stiffness with Magnetic Resonance Elastography". In: *PLoS ONE* 8 (12 Dec. 2013). Ed. by Gareth Robert Barnes, e81668. URL: https://dx.plos.org/10.1371/journal.pone.0081668.

[92] Ligin M. Solamen et al. "Phantom evaluations of low frequency MR elastography". In: *Physics in Medicine and Biology* 64 (6 2019).

[93] Yogesh K Mariappan, Kevin J Glaser, and Richard L Ehman. "Magnetic resonance elastography: a review." In: *Clinical anatomy (New York, N.Y.)* 23 (5 July 2010), pp. 497–511. URL: http://www.ncbi.nlm.nih.gov/pubmed/20544947http://www.pubmedcentral.nih.gov/articlerender.fcgi?artid=PMC3066083.

[94] Farhana Pervin and Weinong W. Chen. "Dynamic mechanical response of bovine gray matter and white matter brain tissues under compression". In: *Journal of Biomechanics* 42 (6 Apr. 2009), pp. 731–735. URL: https://www.sciencedirect.com/science/article/pii/S0021929009000220.

[95] L. Wittevrongel et al. "A Self Adaptive Global Digital Image Correlation Algorithm". In: *Experimental Mechanics* 55 (2 Feb. 2015), pp. 361–378. URL: http://link.springer.com/10.1007/s11340-014-9946-3.

[96] Michael Sutton, Jean-Jose Orteu, and Hubert Schreier. *Image Correlation for Shape, Motion and Deformation Measurements*. Springer International Publishing, 2009, pp. 2–6.

[97] Vincent J Parks. "The range of speckle metrology: Estimates of the largest and smallest displacements measurable with speckle methods are drawn from the literature and laboratory studies". In: *Experimental mechanics* 20 (1980), pp. 181–191.

[98] TC Chu, WF Ranson, and Michael A Sutton. "Applications of digital-image-correlation techniques to experimental mechanics". In: *Experimental mechanics* 25 (1985), pp. 232–244.

[99] Richard Curry. "Response of plates subjected to air-blast and buried explosions". University of Cape Town, 2017.

[100] Jin Yang. *Improved Digital Image Correlation Algorithm*. 2017. URL: http://www.its.caltech.edu/~yangjin/research_DIC.html.

[101] B. Pan. "Recent Progress in Digital Image Correlation". In: *Experimental Mechanics* 51 (7 2011), pp. 1223–1235.

[102] F. Hild and S. Roux. "Comparison of Local and Global Approaches to Digital Image Correlation". In: *Experimental Mechanics* 52 (9 2012), pp. 1503–1519.

[103] Bo Wang and Bing Pan. "Subset-based local vs. finite element-based global digital image correlation: A comparison study". In: *Theoretical and Applied Mechanics Letters* 6 (5 2016), pp. 200–208. URL: http://dx.doi.org/10.1016/j.taml.2016.08.003.

[104] Theodore A. Scambos et al. "Application of image cross-correlation to the measurement of glacier velocity using satellite image data". In: *Remote Sensing of Environment* 42 (3 1992), pp. 177–186.

[105] R. Rosenau, M. Scheinert, and R. Dietrich. "A processing system to monitor Greenland outlet glacier velocity variations at decadal and seasonal time scales utilizing the Landsat imagery". In: *Remote Sensing of Environment* 169 (2015), pp. 1–19. URL: http://dx.doi.org/10.1016/j.rse.2015.07.012.

[106] Marcin Tekieli et al. "Application of Digital Image Correlation to composite reinforcements testing". In: *Composite Structures* 160 (2017), pp. 670–688.

[107] H. Haddadi and S. Belhabib. "Use of rigid-body motion for the investigation and estimation of the measurement errors related to digital image correlation technique". In: *Optics and Lasers in Engineering* 46 (2 2008), pp. 185–196.

[108] Stéphane Avril et al. "Overview of Identification Methods of Mechanical Parameters Based on Full-field Measurements". In: *Experimental Mechanics* 48 (4 Aug. 2008), pp. 381–402. URL: http://link.springer.com/10.1007/s11340-008-9148-y.

[109] Fabrice Pierron and Michel Grédiac. *The Virtual Fields Method*. Springer New York, 2012. URL: http://link.springer.com/10.1007/978-1-4614-1824-5.

[110] Sung ho Yoon, Ioannis Giannakopoulos, and Clive R. Siviour. "Application of the Virtual Fields Method to the uniaxial behavior of rubbers at medium strain rates". In: *International Journal of Solids and Structures* 69-70 (Sept. 2015), pp. 553–568. URL: https://www.sciencedirect.com/science/article/pii/S0020768315001882.

[111] N. Promma et al. "Application of the virtual fields method to mechanical characterization of elastomeric materials". In: *International Journal of Solids and Structures* 46 (2009), pp. 698–715.

[112] T. Guelon et al. "A new characterisation method for rubber". In: *Polymer Testing* 28 (2009), pp. 715–723.

[113] F. Pierron. "Identification of Poisson's ratios of standard and auxetic low-density polymeric foams from full-field measurements". In: *The Journal of Strain Analysis for Engineering Design* 45 (2010), pp. 233–253.

[114] Y. Mei et al. "General Finite-Element Framework of the Virtual Fields Method in Nonlinear Elasticity". In: *Journal of Elasticity* 145 (2021), pp. 265–294.

[115] Jing Guo et al. "Fractal network dimension and viscoelastic powerlaw behavior: II. An experimental study of structure-mimicking phantoms by magnetic resonance elastography". In: *Physics in Medicine and Biology* 57 (12 June 2012), pp. 4041–4053. URL: http://stacks.iop.org/0031-9155/57/i=12/a=4041?key=crossref.ab81f2cef6e70a778ec295db385557a2.

[116] Smooth-On. lnc. *Ecolfex Series technical bulletin*. 2018. URL: https://www.smooth-on.com/tb/files/ECOFLEX_SERIES_TB.pdf.

[117] Smooth-On. lnc. *Ecoflex ™ GEL*. 2018. URL: https://www.smooth-on.com/tb/files/ECOFLEX_GEL_TB.pdf.

[118] Smooth-On. lnc. *Silicone Thinner ®*, p. 22510.

[119] Smooth-On. lnc. *Shore hardness scales*. 2008, p. 2008.

[120] Malcolm L. Williams, Robert F. Landel, and John D. Ferry. "The Temperature Dependence of Relaxation Mechanisms in Amorphous Polymers and Other Glass-forming Liquids". In: *Journal of the American Chemical Society* 77 (14 1955), pp. 3701–3707.

[121] L.A. Steiner and P.J.D. Andrews. "Monitoring the injured brain: ICP and CBF". In: *British Journal of Anaesthesia* 97 (1 July 2006), pp. 26–38. URL: https://www.sciencedirect.com/science/article/pii/S0007091217351802?via%3Dihub.

[122] Goran Žagar et al. "Fracture toughness measurement in fused quartz using triangular chevron-notched micro-cantilevers". In: *Scripta Materialia* 112 (Feb. 2016), pp. 132–135. URL: https://www.sciencedirect.com/science/article/pii/S1359646215004303.

[123] Jon Salem. *Fused Silica and Other Transparent Window Materials*. National Aeronautics and Space Administration, 2016, pp. 1–27. URL: https://ntrs.nasa.gov/archive/nasa/casi.ntrs.nasa.gov/20160010278.pdf.

Appendices

A

Design and simulation of proposal for future test methodology

A.1 Design of apparatus

As seen in chapter 2, current test methodologies suffer from both measurement difficulties[1] and poor control of boundary conditions when measuring brain tissue. Whilst the bulk of this thesis has considered measurements of deviatoric response, we now turn our attention to volumetric behaviour. This chapter considers the design of a novel experimental apparatus which aims to control loading conditions in order to better emulate *in vivo* conditions whilst still allowing for a wide range of loading frequencies and magnitudes in dilatational loading. Simulations and design are conducted, showing that it is feasible, however experiments to this end were not performed, the principal reason being the difficulty of obtaining high speed images of suitable resolution for the VFM analysis.

[1] Due to the extreme softness of brain tissue

A.1.1 Specimen containment

The aim is to conduct experiments on *ex vivo* sections of brain outside of the skull, but contained in a fluid medium to emulate the presence of CSF.

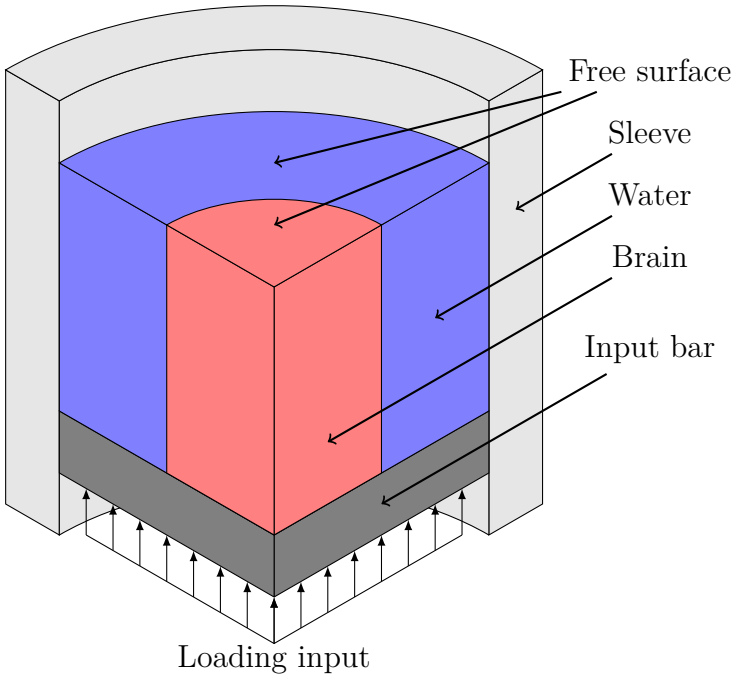


Figure A.1: Quarter cross-section view of proposed loading setup. Loading is applied to the brain sample via the input bar. The brain sample is immersed in cerebrospinal fluid (CSF) simulant, better emulating *in vivo* drainage and loading conditions. The sleeve is transparent, allowing one to image the brain sample directly and make use of DIC for full-field displacement measurements. The free surface guarantees a stress-free boundary, allowing for easy calculation of stresses via integration of the acceleration field.

The specimen constraint shown in fig. A.1 has several advantages over that used in figs. 2.6b and 2.10:

1. The presence of the CSF simulant reduces de-watering, and allows for re-watering on removal of the load - much like the *in vivo* brain.

2. The compressive bulk modulus of brain tissue is the same as water, allowing for 1D compressive loading of the tissue for short time-scales

3. Slightly increasing the hydrostatic pressure in the chamber allows for one to probe the effect of pressure on the brain's behaviour, unlike in open-air

systems[2].

4. The water and sleeve allow for full-field DIC measurements of the surface of the brain sample, which in turn allows for non-contact measurement of the axial stresses via integration of the acceleration field

Note that the free surface at the top of the sample means that this setup is unsuitable for quasi-static loading, as acceleration fields are used to calculate the stresses in the sample. Note too that the duration of the uniaxial compressive loading will be limited by the width of the water layer - as the 1D strain wave travels up the cylinder, a release wave will travel inwards from the walls of the sleeve. Once the release wave arrives at the surface of the brain tissue, the specimen will no longer be in a conditions of 1D strain.

This apparatus is designed for both dilatational and deviatoric characterisation of brain tissue using the same containment device. The same input bar is used for both deviatoric and dilatational loading - the bar is simply loaded via either a torsional shaker or a longitudinal impact respectively.

A.1.1.1 Sleeve material

There are two primary requirements of the sleeve, one mechanical and one optical.

- Optical:
  - The sleeve must be transparent, in order to allow the use of DIC imaging
  - If possible, the sleeve should have a refractive index matching water, in order to reduce the effect of refraction at the sleeve:water boundary (the greater the difference the greater the lens effect). This lens effect can be accounted for (and indeed could plausibly be taken advantage of in order to obtain greater optical zoom) but the lower the lens effect the simpler the optical metrology and analysis
- Mechanical:

[2]The inter-cranial pressure of the skull is 1-2kPA in a healthy adult [121], with significant pathological effects occurring at 5.5-6.6 kPa

Material	E_y (Pa)	K (Pa)	Refractive index
Water	-	2.2×10^9	1.33
60% glucose			1.44
Brain	$10 - 100$	2.2×10^9	-
PMMA	3.2×10^9	5.3×10^9	1.49
Polycarbonate	2.6×10^9	3.3×10^9	1.6
PET	2.7×10^9	3.5×10^9	1.57
'Standard' glass	5.0×10^{10}	3.5×10^{10}	1.52
Fused quartz	7.1×10^{10}	3.7×10^{10}	1.46
ALON [a]	3.34×10^{11}	2.14×10^{11}	1.79
Air			1.00

Table A.1: Approximate stiffness and refractive index of various transparent materials

[a]Aluminium oxynitride is a transparent ceramic with mechanical properties similar to aluminium oxide

- The sleeve must have sufficient strength to withstand the high pressures generated during loading of the brain tissue. This is important from both a practical perspective and from a Health and Safety perspective - the brain tissue should be contained at all times during experimentation.
- The sleeve should be as rigid as possible, in order to provide lateral constraint to the water and keep the loading in a 1D strain state

Table A.1 shows the stiffness and refractive index of various transparent materials, as well as water, brain, and air. This shows that fused quartz and PMMA have the best refractive index [3], however ALON is two orders of magnitude stiffer than the polymer options. Unfortunately ALON is an incredibly expensive material to obtain and shape, making it impractical. This leaves fused quartz as the best option for a containment sleeve, particularly as fused quartz tubes are already widely available and in use in the chemical industry. Fused quartz has a fracture toughness of approximately 0.67 MPa·m$^{0.5}$ [122] and a failure strength of approximately 80 MPa [123]; this is sufficient for the loading regime envisioned, and will safely keep the sample contained.

[3]Particularly once some glucose is added to the water, raising the refreactive index slightly

A.1.2 Dilatational characterisation

Applying a compressive stress wave in the sample via the input bar will result in an initially 1D strain state. Given that brain tissue and water have effectively the same bulk modulus and density, this wave will travel through both the fluid medium and the brain sample at the same speed. Unless the sleeve is perfectly rigid, however, a release wave will travel inwards from the walls, limiting the duration of the 1D strain state to approximately $\frac{t}{c}$ where c is the speed of sound in the fluid, and t is the thickness of the fluid region. For water, this means that the 1D strain state will last for approximately 1 ms per 1.5 mm of fluid thickness.

Due to the high dilatational wave-speed ($\approx$ 1500 m/s) and small sample size, each test will last only a few ms - this will require very high speed imaging in order to capture sufficient frames per test.

A.1.2.1 Loading method

As a result of the free surface and fluid medium, the device can only be used when vertical - this makes it challenging to load with a traditional SHPB apparatus, unless the entire SHPB apparatus is mounted vertically. Instead it is proposed that the specimen is loaded as a drop bar apparatus - the entire containment apparatus including the input bar will simply be dropped a short distance onto a rigid surface (such as a steel plate). This will generate a stress wave which travels up the bar and into the specimen.

The load magnitude will be limited by the drop distance, however this experiment does not require particularly high stresses when compared to typical SHPB tests. If greater load magnitudes are required, a vertically oriented pneumatic impact bar can be used. During the design phase the fluid medium was approximated as inviscid. Later simulations show that this approximation is valid over the range of viscosity exhibited by water.

A.1.2.2 Stress measurement

As in the high rate shear tests, the stress will be measured either through direct integration of acceleration terms, or through the full dynamic VFM. This is covered in detail in chapters 2 and 4, but for convenience the simple 1d case is repeated here.

Consider a 1D rod with a known acceleration field and initial density, with a free end at $X = 0$. Satisfying the 1D conservation of momentum equation results in:

$$\frac{\partial \sigma}{\partial X} + b = \rho \ddot{x} \tag{A.1}$$

Integrating eq. (A.1) from the stress free end at $X = 0$ and neglecting body forces results in:

$$\sigma(X) = \int_0^X \rho(X)\ddot{x}(X)dX \tag{A.2}$$

This integral will give an expression for the compressive stress throughout the specimen, and is what is used for the rest of this chapter. Should this method be used experimentally, then a more sophisticated use of the VFM such as that shown in chapter 4 would be used.

A.2 Simulation of experimental setup

The proposed experimental setup was simulated using quarter symmetry in Abaqus. Representative material properties from the literature were used for the brain tissue, fluid medium, input bar, and containment sleeve. Given the small displacements expected, a Lagrangian element formulation was used for all materials (including water). C3D8R elements were used for all parts, with a maximum size of 50 µm for elements modelling brain or water - the sleeve and input bar elements were double this length, and kept below 100 µm. This ensured that each wave was captured by at least 10 elements - if the wavelength approaches 3 elements, the artificial viscosity in the solver rapidly dissipates the wave. Abaqus's Explicit Dynamic solver was used for all simulations.

The input bar and containment sleeve were both modelled with linear-elastic constitutive models, whilst the brain sample and fluid medium were modelled using the Mie-Grüneisen equation of state (EOS) combined with Newtonian viscosity and linear elastic shear behaviour. The linearised Mie-Grüneisen EOS models the pressure as:

$$P = \frac{\rho_0 c_0^2 \eta}{(1 - s\eta)^2} \left(1 - \frac{\Gamma_0 \eta}{2}\right) + \Gamma_0 \rho_0 E_m \tag{A.3}$$

where η is the volumetric strain $(1 - \frac{\rho_0}{\rho})$, and Γ_0 is the Grüneisen ratio. c_0 and s define the relationship between the shock velocity U_s and the particle velocity U_p: $U_s = c_0 + sU_p$. Note that $\rho_0 c_0^2$ is equivalent to the small strain elastic bulk modulus, and that there is a limiting case for the volumetric strain of $\eta_{lim} = \frac{1}{s}$. Table A.2 shows the parameter values used to model brain tissue; water was modelled the same way, but with a Newtonian viscosity of 6.91×10^{-4} Pa.s instead of a shear stiffness.

Parameter	ρ_0 (kg/m^3)	G (Pa)	c_0 (m/s)	s	Γ_0
Value	1000	1000	1500	1.85	1.65

Table A.2: Material parameters for simulating brain under compression

A.2.1 Effect of sleeve material on stress wave

A step load of 1 MPa was simulated for 3 sleeve materials: PMMA, Quartz, and a perfectly rigid material.

Figures A.2 and A.3 show the stress in the 22 (axial) direction at the surface of the specimen at 5μs when loaded with a step load of 1MPA pressure via the input bar (see fig. A.1 for geometry). Figure A.2 shows the axial stress at the surface of the specimen (at the brain:water interface) during testing - this is the surface that is visible for high speed photography and DIC, and the surface for which the deformation will be measured. This figure clearly shows that increasing the rigidity of the containment sleeve improves the match between the input pulse (a 1MPA step pulse) and the loading of the specimen. What this figure does not describe however, is the uniformity of that loading - as measurements are taken only at the

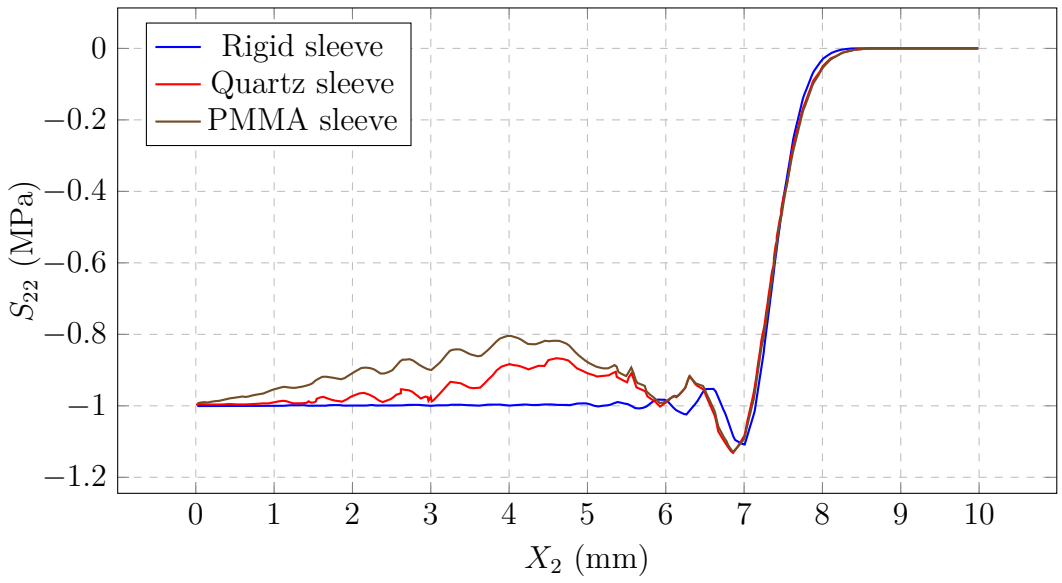


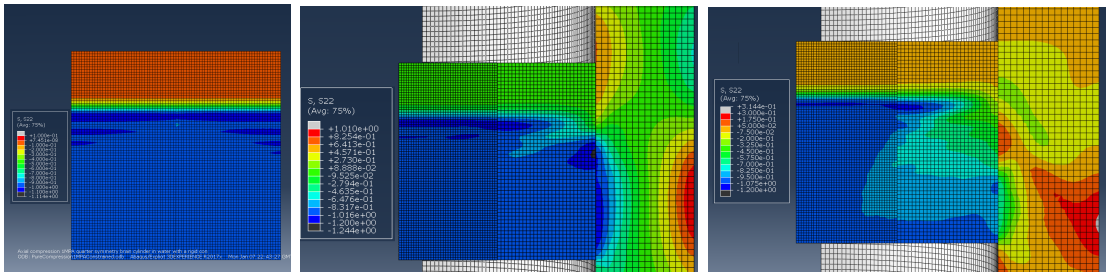
Figure A.2: Axial stress distribution along the surface of the sample at 5μs. Loading is a step load of 1 MPa pressure. Three containment material types are modelled: perfectly rigid (blue), quartz (red), and PMMA (brown).

surface of the sample, it is important that the stress state throughout the sample is uniform at a given axial co-ordinate (i.e. does not vary with radial co-ordinate).

Figure A.3 shows the stress distribution throughout the sample (and surrounding fluid and containment sleeve) - fig. A.3a models only the sample and surrounding fluid with a rigid boundary condition, whilst figs. A.3b and A.3c model quartz and PMMA sleeves as well. This shows that the rigid sleeve results in a perfectly uniaxial distribution of S_22, with no radial variation in either the brain or the fluid. The simulation with the quartz sleeve shows the effect of the radial release wave affecting the stress distribution in the fluid, but not significantly affecting the stress distribution in the sample - allowing for the sample to be modelled as undergoing 1D strain. Figure A.3c shows that the release wave has significantly affected the stress distribution in the sample, invalidating the 1D assumption and disallowing PMMA as a sleeve material.

A.2.2 Effect of friction on stress wave

Assuming 1D strain and integrating the acceleration field according to eq. (A.2) will result in a small error if the shear stresses due to the fluid medium's viscosity



(a) Rigid sleeve **(b)** Quartz sleeve **(c)** PMMA sleeve

Figure A.3: Distribution of S22 at 5μs for various containers, using a clean loading pulse of 1 MPa. Figure a models only a brain specimen and a water specimen, whilst figures b and c show brain, water, and the sleeve material. Note that the magnitudes of the stress waves are not of great importance, but rather the distribution within the brain tissue. A nominally perfect rigid sleeve results in a perfectly 1d stress profile, a quartz sleeve is worse, but most of the inhomogeneity in the stress wave occurs in the water portion, rather than the sample. For a PMMA sleeve, even the sample portion undergoes messy loading

are not considered. Figure A.4 shows the stress profile using a PMMA input rod and a PMMA sleeve. The stress is calculated via integration of the acceleration field and via integration of both the acceleration field and the surface shear stress due to Newtonian viscosity. As the figure shows, the effects of viscosity have a negligible contribution to the stress state in the material. By far the largest source of error in this figure is the effect of the release wave (due to use of a PMMA sleeve) - this causes the mismatch between the calculated and actual stress around 5mm in. Note that this matches up with the location of the release wave in fig. A.3c in spite of the difference in loading regime (PMMA striker vs step pulse).

A.2.3 Parameter extraction from simulated experiment

Simulated experiments have now shown that eq. (A.2) can be used for the proposed experimental setup, however the acceleration data input to generate fig. A.4 were extracted directly from the FE simulation. In reality, displacement data will first be extracted from DIC, derived with respect to time, and then integrated spatially - leading to errors at each step. There will be two primary sources of error:

- Spatial error: The camera used will have finite spatial resolution, and some noise in the measurements

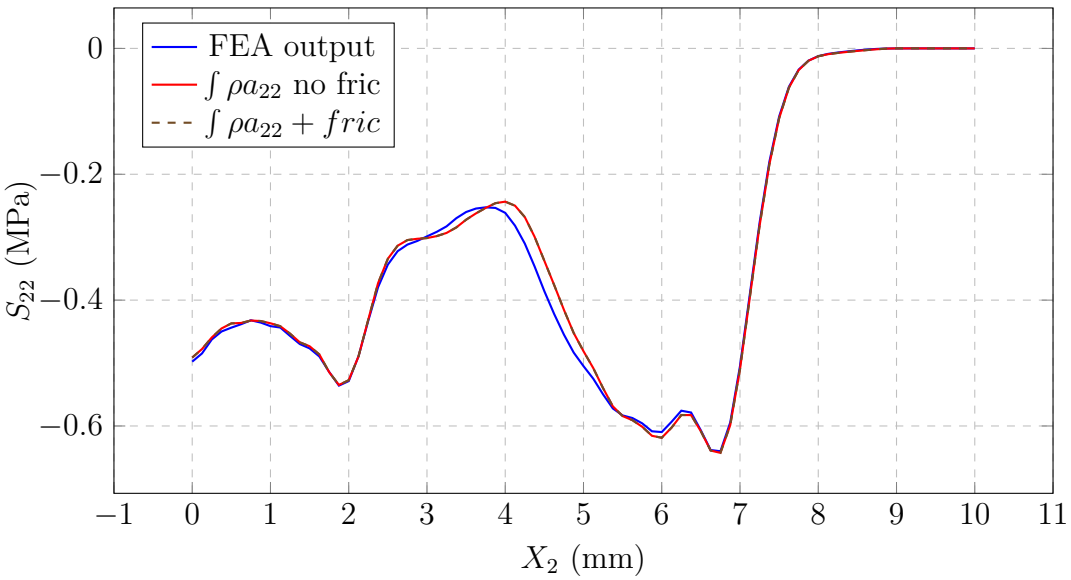


Figure A.4: Stress at the surface of the specimen compared to stress calculated by integrating the acceleration field and stress taking friction effects into account. Note that the shear stresses due to Newtonian viscosity in the fluid medium are negligible - lines 2 and 3 overlap almost exactly. Loading is 1 MPa applied through a PMMA input bar - the impedance mismatch at the PMMA-sample interface causes ineffective force transmission, hence the particularly non-constant stress profile

- Temporal resolution: the camera will have finite temporal resolution based on the frame-rate at which the images are taken

The spatial error will cause noise in the displacement data, which will be amplified when calculating strain (due to taking the numerical derivative of noisy data). This spatial error will be reduced when calculating the stress field however, as the numerical integral of a noisy signal reduces the effects of noise[4].

The reduced temporal resolution will limit the measurable frequencies - this will have a particularly noticeable effect if the loading pulse contains high frequency components (such as are present in a square wave), as these components will not be measured, leading to artificial smoothing of the acceleration field.

Figure A.5 shows the stress at the surface of the specimen calculated via integration of the acceleration field, as well as the "actual" stress extracted directly from FEA. For comparison, the strain multiplied by the (known) bulk modulus is also shown. Note that even at a frame rate of 1 000 000 fps, the acceleration field

[4]Provided that the noise is symmetrical and not biased

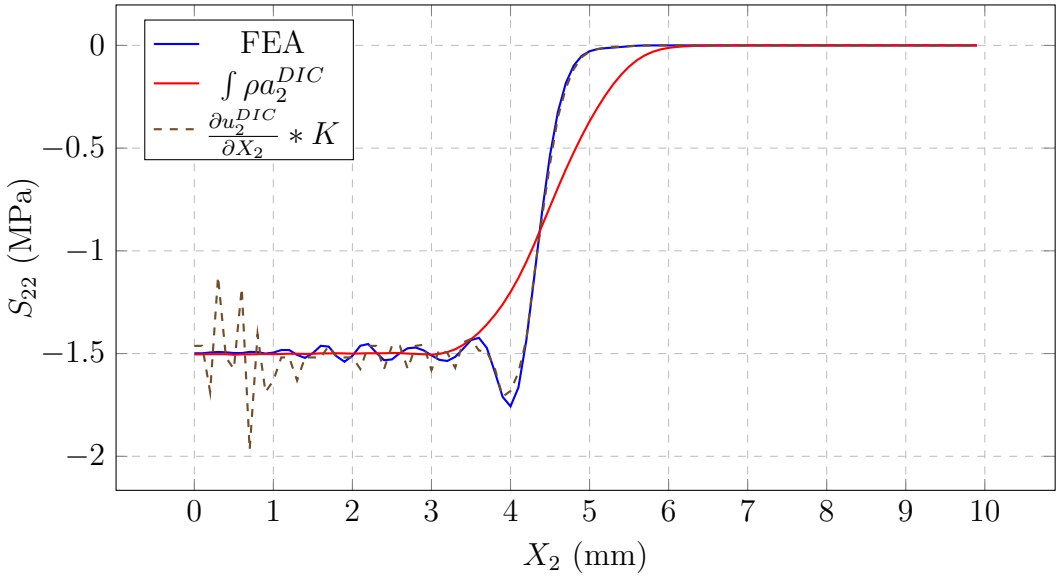


Figure A.5: Stress at the surface of the specimen according to FEA output, integrating the acceleration field of the DIC output, and multiplying the DIC strain field by the bulk modulus of the specimen.

is still smoothed out - removing both noise and actual high frequency components. The strain data is the opposite, as it is derived rather than integrated - any noise in the displacement field is exaggerated. Overall however, (away from the wave-front), the output approximately matches the input to the simulation.

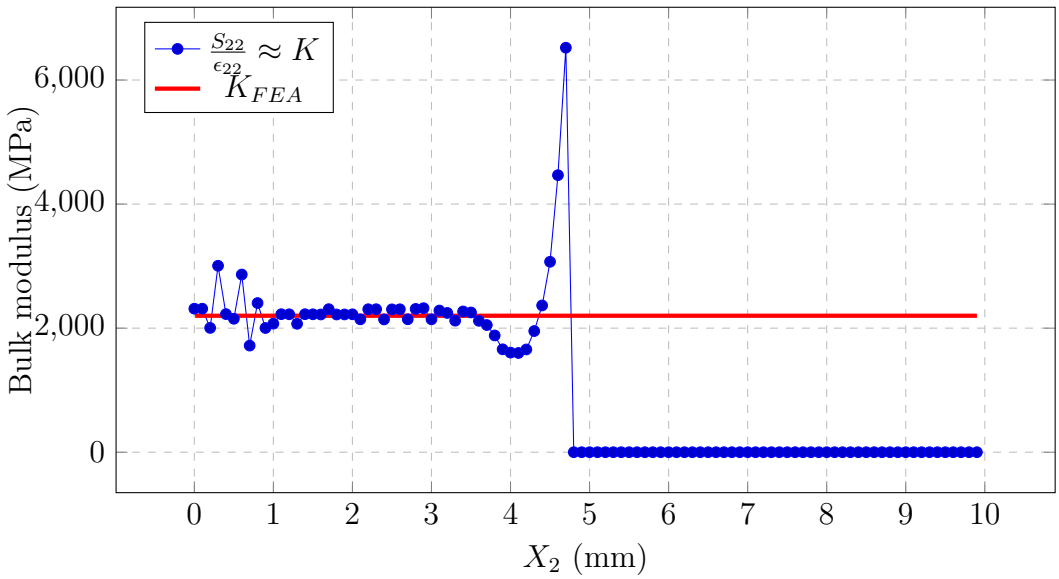


Figure A.6: Bulk modulus obtained by comparing the stress in fig. A.5 to the measured strain. Where the measured strain was less than 10% of the maximum strain, this region was ignored in order to avoid dividing by very small strain values.

Figure A.6 shows the bulk modulus calculated by comparing the calculated stress to the measured strain - this method gives reasonable results away from the wave-front, but gives clearly spurious result at the wave-front due to the aforementioned stress field smoothing caused by frame-rate limitations.

A.2.4 Conclusion

The above simulation show that the proposed methodology is clearly feasible, and should be conducted. As can be seen in fig. A.5, making use of the camera currently available to the author would result in a blurring of the wavefront of at least 3 mm purely due to limitations to framerate, not to mention additional blurring due to the low resolutions available at these framerates.

Whilst the high speed cameras currently available to the author do not have sufficient framerate and resolution to accurately conduct the proposed experiments, cameras with said resolution and frame-rate do exist. Additionally, given the current and historic trajectory of camera resolution and framerate, it is highly likely that camera performance will continue to improve. As such, the author strongly recommends that this apparatus be built, and this set of proposed experiments be conducted.